



Faculteit Wetenschappen
Departement Fysica

Characterization of scanning gate technique and transport in nanostructured graphene

Karakterisatie van de scanning gate-techniek en van transport in nanogestructureerd grafeen

Proefschrift voorgelegd tot het behalen
van de graad van doctor in de wetenschappen
aan de Universiteit Antwerpen te verdedigen door

Marko Petrović

Promotor
Prof. Dr. François Peeters

Antwerpen 2017

Members of the jury

Chairman

Prof. Dr. Joke Hadermann, University of Antwerp, Belgium

Supervisor

Prof. Dr. François Peeters, University of Antwerp, Belgium

Members

Prof. Dr. Dirk Lamoen, University of Antwerp, Belgium

Prof. Dr. Wim Magnus, University of Antwerp, Belgium

Prof. Dr. Thomas Ihn, ETH Zurich, Switzerland

Prof. Dr. Benoît Hackens, UC Louvain-la-Neuve, Belgium

Prof. Dr. Etienne Goovaerts, University of Antwerp, Belgium

Contact information

Marko Petrović

Groenenborgerlaan 171 U208

2020 Antwerpen

Belgium

mpetrovic.ks@gmail.com

Dedicated to my mother Milanka

Acknowledgements

First and foremost, I would like to thank my supervisor Prof. Dr. François Peeters for guiding me towards the completion of this dissertation. His understanding, constructive feedback and attention to detail helped me to see the shortcomings of my own ideas, and to constantly correct myself. I would also like to express my gratitude to Prof. Dr. Andrey Chaves for sharing his wave packet code with me, and for providing insightful comments and advice. Special thanks goes to my friend and colleague Dr. Slaviša Milovanović, for devoting his time and effort to perform some of the semi-classical calculations shown in this thesis.

My sincere gratitude goes to my friends and colleagues, current and past members of the CMT. Thank you for your help, and for all the interesting and funny discussions. You've made my stay at the CMT a very pleasant experience.

At the end, I am very grateful to my family for their love and support. Thank you to my late mother Milanka and my father Dušan, my sisters Marija and Marina, and to little Pavle, who always makes me laugh.

This work was supported by the Methusalem Funding of the Flemish Government.

Contents

1	Introduction	1
1.1	Short history of quantum transport	1
1.2	2D electron gas	4
1.3	Graphene	6
1.4	Aharonov-Bohm effect	10
1.5	Scanning gate microscopy	12
1.6	Motivation and organisation of the thesis	14
2	Theoretical background	17
2.1	Landauer-Büttiker formalism	17
2.1.1	Landauer formula	17
2.1.2	Büttiker multi-terminal formula	21
2.2	S-matrix and Green's functions	22
2.3	KWANT	26
3	SGM of Aharonov-Bohm Rings	29
3.1	Scanning gate microscopy of 2DEG rings	29
3.2	Theoretical model	32
3.3	Single band transport	36
3.3.1	Radial fringes	37
3.3.2	Concentric fringes	41
3.3.3	Magnetic field dependence	44
3.4	Multiband transport	45
3.5	SGM of AB rings: Conclusions	50

4	Fano resonances	53
4.1	Introduction	53
4.2	System and Methods	55
4.3	Dispersion relation	57
4.4	Transmission of individual modes	59
4.5	Mirror symmetry and intervalley scattering	61
4.6	Fano resonances	65
4.7	LDOS and the electrical current	69
4.8	Fano resonances in GNR: Conclusion	74
5	Vacancy disorder	77
5.1	Introduction	77
5.2	System and Methods	80
5.3	Results	85
5.3.1	Effects of different disorder types	85
5.3.2	Changing vacancy concentration	91
5.3.3	Changing the magnetic field	92
5.3.4	Decomposition of R_B and the current density	98
5.3.5	NNN interaction	101
5.4	Conclusions	103
6	Electron guiding in graphene	105
6.1	Introduction	105
6.2	System and Methods	107
6.3	Results	108
6.3.1	Dispersion relations	108
6.3.2	Incoming and outgoing modes	111
6.3.3	Current guiding	114
6.3.4	Bend and Hall resistances	117
6.4	Conclusions	120
7	SGM in graphene	123
7.1	Introduction	123
7.2	Focusing system and SGM potential	125
7.3	Scaling the tight-binding Hamiltonian	129
7.4	Magnetic focusing	131
7.5	Scanning gate microscopy	135
7.6	Resistance maps of a six-terminal device	139
7.7	Summary	143

8	Summary and outlook	145
9	Samenvatting	149
Appendices		
Appendix A	Force field in classical SGM simulation	155
Appendix B	Expression for the modified vector potential	157
References		161
CV		

Abbreviations

2DEG Two-dimensional Electron Gas.

AB Aharonov-Bohm Effect.

AFM Atomic Force Microscopy.

BN Boron nitride.

DOS Density of states.

FQHE Fractional Quantum Hall Effect.

FWHM Full width at half maximum.

GNR Graphene nanoribbon.

HWHM Half width at half maximum.

IQHE Integer Quantum Hall Effect.

KWANT A software package for quantum transport.

LB Landauer-Büttiker.

LDOS Local density of states.

LL Landau level.

MOSFET Metal-oxide-semiconductor field-effect transistor.

NEGF Non Equilibrium Green's Functions.

NNN Next-nearest neighbour.

QPC Quantum Point Contact.

QR Quantum ring.

SGM Scanning Gate Microscopy.

STM Scanning Tunneling Microscopy.

CHAPTER 1

Introduction

1.1 Short history of quantum transport

The field of *quantum transport* can be placed within a broader discipline called *nanoscience*.¹ We can view nanoscience as a combination of several historically well established science branches, such as physics, chemistry, and materials science (as well as engineering) with each branch being applied to solve specific problems in the field. The major goal of nanoscience is to control and manipulate matter on very small scales. With that aim, typical research in nanoscience serves a double purpose. On the one hand, it explores the fundamental physical phenomena operating at the nanoscale, and on the other hand, it searches for possible utilization of these phenomena. Nanoscience also deals with constructing nanoscaled devices, or *nanostuctures*. The word “nano” comes from Greek, and it means “dwarf”, therefore the literal translation of the word “nanostucture” is a “dwarf-structure”.² Quantum transport stemmed from the field of *mesoscopic physics* in the early 1980s.^{1,3} The word “meso” also comes from the Greek language, meaning “intermediate” or “middle”, and for mesoscopic physics this has a double meaning. The first interpretation is related to the size of studied systems, because they are in between the atomic (microscopic) scales and the (macroscopic) scales of everyday objects. The word “meso” then signifies the scales in between the “micro” and the “macro”. The second meaning is related to

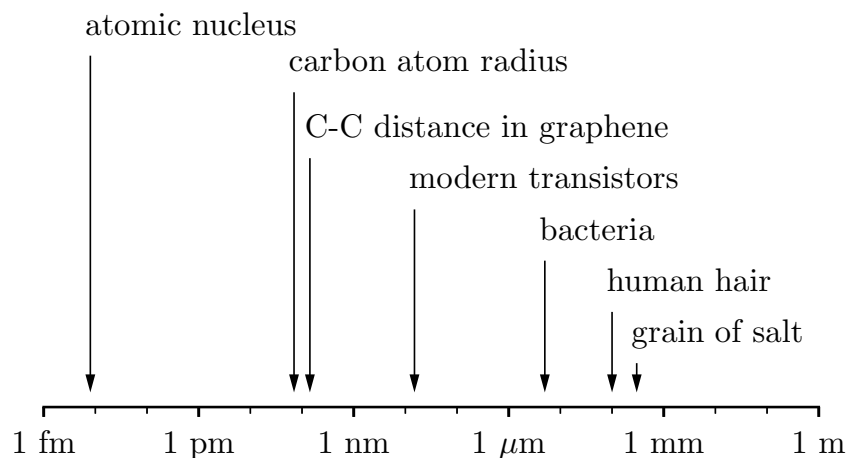


Figure 1.1: Logarithmic length scales: scales relevant for mesoscopic physics are those in the nanometer range, which is a typical size for a mesoscopic device.

the main physical laws operating at these two scales. In contrast to atoms, which are governed by quantum mechanics, the macro world obeys classical laws. Therefore the “meso” scales are those in between quantum and classical scales. Since there is no clear demarcation between the quantum and classical scales (the quantum features disappear gradually as we increase the scale of the studied system), the term mesoscopic is now mainly used to connect the two separate transport regimes, the quantum and the classical one.¹ In Fig. 1.1 we present the wider length range, centered around scales relevant for mesoscopic physics and transport.

When it comes to transport in mesoscopic devices it is also important to separate few important lengths and their relations to transport. Beside the size of the device (L), important lengths are the electron wavelength and the electron mean free path. The mean free path is the distance that an electron travels before its momentum is significantly changed due to impurity scattering.⁴ If the device size is larger than the mean free path (the momentum relaxation length as it is sometimes called), then electron transport is considered to be *diffusive*. On the other hand, if an electron travels across the device without significant change in its momentum, then we are in the *ballistic* regime. Another transport regime occurs in samples exposed to high magnetic fields, where the emergence of edge channels suppresses electron

scattering. In this thesis we investigate only ballistic transport regime, and transport in high magnetic fields. It is also important to stress that this thesis deals only with systems in which electrons are free to move in two spatial dimensions, while their motion is confined in the third dimension as is the case in two-dimensional electron gas 2DEG.

Ref. [2], which focuses on electrical transport in semiconductor nanostructures, traces the origin of transport studies back to the Drude model, and later to the discovery of the first transistor in the 1940s. With Moore's law, and the consequent miniaturization, the necessity for quantum mechanical description of transport phenomena became apparent in the following decades. There are several experimental milestones which paved the way to modern research, to name a few:

- The discovery of integer quantum Hall effect (IQHE) in 2DEG.⁵
- The discovery of fractional quantum Hall effect (FQHE) in 2DEG.⁶
- The measurement of conductance quantization in quantum point contacts (QPC).^{7,8}
- The realization of quantum dots (QD)[†].
- The Coulomb-blockade effect in quantum dots.
- The Aharonov-Bohm effect (AB).
- The discovery of graphene and other 2D materials.
- The measurements of QHE in graphene.

Although some of these discoveries are more than twenty years old, they are still very important topics of present day research.

The exploration of nanoscales would not be possible without significant improvements in measuring techniques. The construction of scanning tunneling microscope¹⁰ (STM) in 1981–82, and the first successful STM experiments¹¹ opened the whole field of nanoscience. Using similar principles the atomic force microscope was constructed in 1985. Most of the previous experimentally observed phenomena required extreme operating conditions such as high magnetic fields, low temperatures (few Kelvins), high vacuum,

[†]According to Ref. [2], the term *quantum dot* appeared first in the year 1986 in Ref. [9], but the first experiments on confined electrons were performed several decades earlier.

or special care in patterning the devices. Therefore new techniques for effective cooling, etching, and sample preparation were developed in order to perform these previous measurements. On the other hand, some effects were predicted before the experiment was performed (e.g. Aharonov-Bohm effect).

The experimental discoveries and improvements in measuring techniques were complemented with theoretical breakthroughs. Each of the previous experimental discoveries was accompanied with theoretical explanation of the underlying physics behind the observed effect. The theoretical approach we take in this thesis is the so-called *S-matrix* approach, pioneered by Landauer.¹² We devote the whole next chapter to the explanation of this approach, but now we would like to point out that the main idea behind it is that the transport characteristics of a device are directly related with the charge carrier transmissions.

In the rest of this chapter we give a short introduction to each of previously mentioned main topics in quantum transport that is of interest to this thesis. We start with electron confinement in two dimensions in conventional semiconductor nanostructures. Next, we give a short introduction to graphene, and describe the basis of Aharonov-Bohm effect. In the last subsection we explain a typical scanning gate experiment.

1.2 2D electron gas

One of the major steps in the development of all modern electronic devices was the realization of a two-dimensional electron gas. A typical example is a MOSFET device in which the carriers are confined in a two-dimensional (inversion) layer. In modern experiments, nanodevices are usually made from semiconductor heterostructures. The important concept here is *doping*. Impurities can be added to semiconducting materials to modify their chemical potential. The material can be p-doped or n-doped depending on whether the embedded impurities add or extract electrons from it. Heterostructures are formed when two different materials are deposited on top of each other. Usually the two materials have matching lattice constants, therefore the connection is smooth and there is no strain induced. After they are brought in contact, the electrons from the n-doped layer would eventually go to the p-doped layer and localize on the interface of the two materials, forming a two-dimensional layer. A typical band diagram close to the interface is presented in Fig. 1.2. The electrons in n-doped GaAlAs enter p-doped GaAs leaving behind positively charged donors. The conduction and valence bands

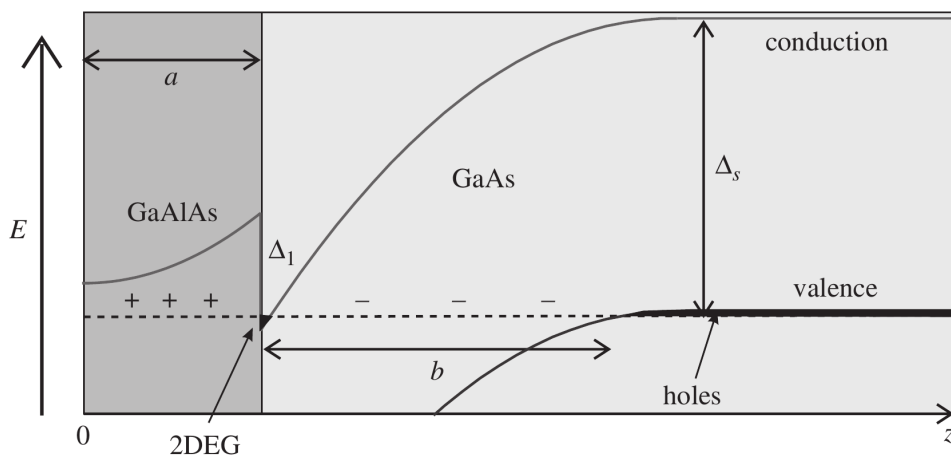


Figure 1.2: Band edges in GaAlAs-GaAs heterostructure along the growth direction (full curves). The Fermi energy is given by the horizontal dashed line. Image taken from Ref. [1].

in GaAs bend and there is a very narrow region on the interface where electrons are confined only in one direction.

Due to the very narrow size of this localization region, electrons inside it exhibit quantization in the normal, growth direction (z). Since confinement occurs only in the z direction, and electrons are free in the x and y direction, the electron wave function can be divided in two parts $\Psi(x, y, z) = \psi(x, y)\Phi_n(z)$. The wave function in the plane is given by plane waves, and there are different subbands due to the quantization along the z direction. Usually (because of the narrow spatial confinement along the z direction) the energy separation between the different localized states is large, so only the lowest localized state is occupied. Because this part of the wave function is the same in the whole plane, and it can't change, the wave function along z is sometimes not considered in transport studies.

After the 2DEG is created between the two layers, it can be further processed into nanostructured devices, such as Hall bars, small rings, quantum point contacts etc. This is usually performed through several techniques such as photolithography, electron beam lithography or AFM lithography.² The first two are similar, and involve depositing a layer of photoresist on top of the sample, which is then exposed to UV light or to electrons with high energies. A mask with a specific pattern of the device is used to define the

exposed regions. After the exposure, the photoresist in the exposed region is easily removed. Next step in the process depends on the purpose. To structurally delimit the 2DEG, the sample needs to be etched, and the 2DEG is removed beneath those areas not covered with the photoresist. In the final step the remaining resist is also removed. If the purpose is to create metallic contacts, the procedure is different. After the development of a photoresist, a thin layer of metal is deposited on top of the device. The so-called lift-off technique is used to remove the metal in areas of the photoresist. The third technique of creating patterns in 2DEG involves a biased tip of the atomic force microscope (AFM). If a proper potential is applied on top of the tip, the tip will oxidize the top surface of the sample. The created oxide layer will deplete the 2DEG beneath it. This technique allows to separate the 2DEG in different regions, and impose additional confinement on the electrons.

1.3 Graphene

Semiconductor heterostructures were widely used materials capable of sustaining two-dimensional electron gases. However, with the discovery of graphene, a new opportunity to study 2D electrons emerged. Graphene is a 2D material consisting of a single layer of carbon atoms. Beside a single layer, graphene can be produced and stacked in two, three or even several layers. For a very large number of layers the material is known as graphite. Before the discovery of its two dimensional form, graphene was known through its non planar allotropes, such as carbon nanotubes and fullerenes. Carbon atoms in graphene are arranged in a honeycomb crystal lattice shown in Fig. 1.3. The lattice consists of two groups of carbon atoms arranged in two interpenetrating triangular lattices, usually marked with *A* and *B*. A single carbon atom in graphene posses six electrons orbiting its nucleus, therefore its electron configuration is $(1s)^2(2s)^2(2p)^2$. This is the case when carbon is in its ground state. However, when excited, one electron from the $2s$ orbital can populate one $2p$ orbital, and the other two $2p$ electrons can mix with $2s$ to form a sp^2 hybridized state. The hybridization causes carbon atoms to bond in structures with characteristic angle of 120° . After the hybridization, one $2p$ electron is left unhybridized, and perpendicular to the sp^2 hybridization plane ($2p_z$), and these electrons form π bonds.

Long before it was experimentally discovered, graphene was studied theoretically by Wallace in Ref. [13], in order to understand the electronic structure of graphite. The wave function of an electron in a monolayer graphene

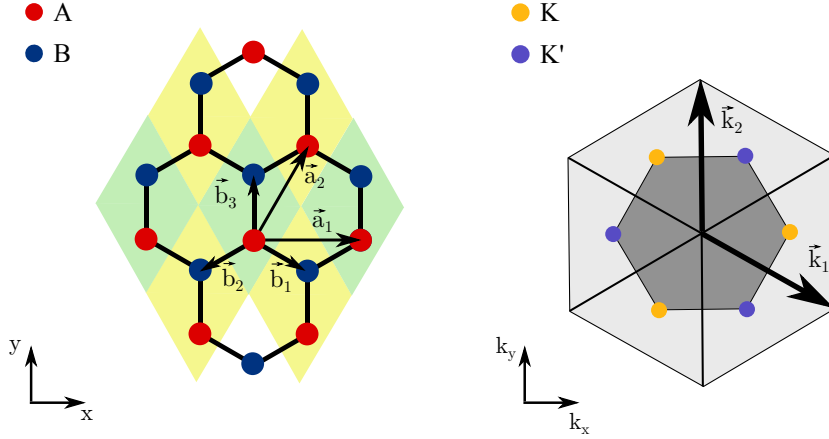


Figure 1.3: (Left side) Graphene honeycomb lattice with two carbon atoms in the unit cell (A and B). Distance between carbon atoms is $a_0 = 1.42 \text{ \AA}$, and the two lattice vectors are $\mathbf{a}_1 = (a, 0)$, and $\mathbf{a}_2 = (a/2, a\sqrt{3}/2)$, where $a = a_0\sqrt{3}$. The three nearest neighbor vectors are $\mathbf{b}_1 = (a_0\sqrt{3}/2, -a_0/2)$, $\mathbf{b}_2 = (-a_0\sqrt{3}/2, -a_0/2)$, and $\mathbf{b}_3 = (0, a_0)$. (Right side) The first Brillouin zone (dark inner hexagon) with six corner points. The two basis vectors in the reciprocal space are $\mathbf{k}_1 = (2\pi/a, -2\pi/a\sqrt{3})$, and $\mathbf{k}_2 = (0, 4\pi/a\sqrt{3})$.

can be written as a sum of contributions coming from the two sublattices

$$\psi_{\mathbf{k}}(\mathbf{r}) = a_{\mathbf{k}}\psi_{\mathbf{k}}^{(A)}(\mathbf{r}) + b_{\mathbf{k}}\psi_{\mathbf{k}}^{(B)}(\mathbf{r}), \quad (1.1)$$

where $\psi_{\mathbf{k}}^{(A,B)}$ are Bloch functions

$$\psi_{\mathbf{k}}^{(j)}(\mathbf{r}) = \sum_{\mathbf{R}_l} e^{i\mathbf{k}\cdot\mathbf{R}_l} \phi^j(\mathbf{r} - \boldsymbol{\delta}_j - \mathbf{R}_l). \quad (1.2)$$

Index j in previous equation signifies a sublattice type (A or B), and \mathbf{R}_l is the position vector of l -th unit cell. Vector $\boldsymbol{\delta}_j$ is a displacement vector from the center of the current cell to a lattice site j , and ϕ^j is the orbital wave function of the carbon atom belonging to sublattice j . The two-component wave function could be used to solve the Schrödinger equation $\hat{H}\psi_{\mathbf{k}} = \epsilon_{\mathbf{k}}\psi_{\mathbf{k}}$, and an approximate solution in the tight-binding model yields the graphene dispersion

$$\epsilon_k^\lambda = t'_{NNN} \left(3 + 2 \sum_{i=1}^3 \cos(\mathbf{k} \cdot \mathbf{a}_i) \right) + t\lambda \sqrt{3 + 2 \sum_{i=1}^3 \cos(\mathbf{k} \cdot \mathbf{a}_i)}, \quad (1.3)$$

1.3. Graphene

where vector \mathbf{a}_3 is defined as $\mathbf{a}_3 = \mathbf{a}_2 - \mathbf{a}_1$. Terms $t = -2.7$ eV and $t'_{NNN} \approx 0.1t$ are nearest- and next-nearest-neighbour hopping terms, defined as

$$t = \int d^2r \phi^{A*}(\mathbf{r}) \Delta V \phi^B(\mathbf{r} + \mathbf{b}_3), \quad (1.4)$$

$$t'_{NNN} = \int d^2r \phi^{A*}(\mathbf{r}) \Delta V \phi^A(\mathbf{r} + \mathbf{a}_1), \quad (1.5)$$

and $\lambda = \pm 1$ signifies two possible solutions (bands). The ΔV term in previous two integrals is the potential energy coming from all other atoms in the sample.

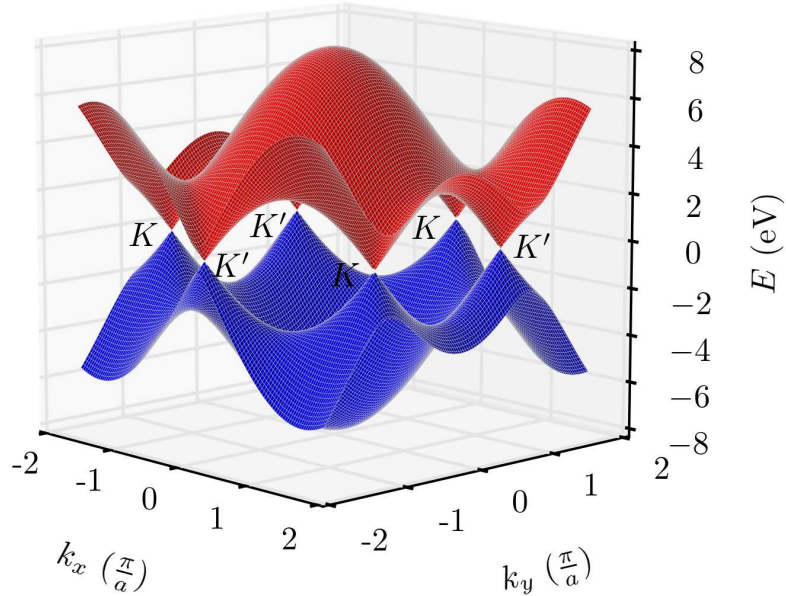


Figure 1.4: Graphene dispersion relation: The two bands (electron band—red surface, and hole band—blue surface) touch at six corners of the first Brillouin zone. Only two corners from these six are unique, and the other four corners can be obtained by appropriate translations by reciprocal lattice vectors. Figure is obtained from Eq. (1.3) by setting $t_{NNN} = 0$.

The two dispersion bands described by Eq. (1.3) are shown in Fig. 1.4. They touch at six corners of the Brillouin zone, known as Dirac points. In the low energy part of the spectrum, the dispersion can be expanded in

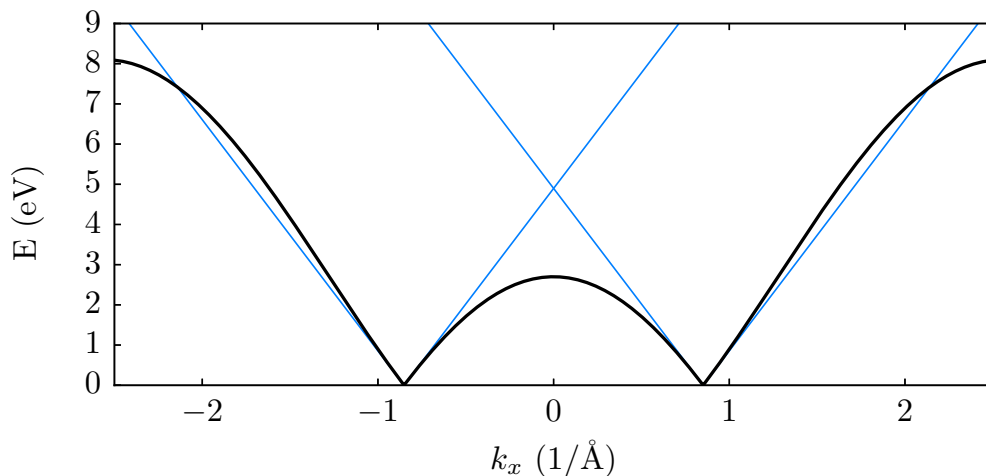


Figure 1.5: Comparison of the dispersion given by Eq. (1.3) for $k_y = 2\pi/a\sqrt{3}$ (black curve), and the linear dispersion given by Eq. (1.8) (blue lines).

the vicinity of the six Dirac points. Starting from a low-energy effective Hamiltonian,¹⁴

$$\hat{H}_{\mathbf{q}}^{\text{eff},\xi} = \xi \frac{3ta}{2} (q_x \sigma_x + \xi q_y \sigma_y), \quad (1.6)$$

where σ_x and σ_y are Pauli matrices

$$\sigma_x = \begin{pmatrix} 0 & 1 \\ 1 & 0 \end{pmatrix} \quad \text{and} \quad \sigma_y = \begin{pmatrix} 0 & -i \\ i & 0 \end{pmatrix}, \quad (1.7)$$

and \mathbf{q} is a small wave vector around one of the six Dirac points. The parameter ξ is used to separate between Hamiltonians of the two valleys ($\xi = 1$ for the K valley, and $\xi = -1$ for the K' valley). The low-energy solution of the Schrödinger equation is then linear in momentum, and does not depend on the valley index ξ

$$\epsilon_{\mathbf{q}}^{\lambda,\xi} = \lambda \hbar v_F |\mathbf{q}|, \quad (1.8)$$

where $v_F = -3|t|a/2\hbar$ is known as the Fermi velocity in graphene. Because of linearity, and the fact that \mathbf{q} can point in any direction, the low energy solutions can be approximately represented as six narrow cones, placed at the six Dirac points. Also, due to the linearity in the low energy part of the spectrum, the collective low-energetic excitations are treated as massless particles, also known as massless Dirac fermions. Zero mass carriers in

graphene behave similar to relativistic particles, and that is why they show some similar relativistic effects, such as for example Klein tunneling.¹⁵

Linear approximation is only valid for low energies as shown in Fig. 1.5, where we compare approximate tight-binding solution with its linear approximation. From the figure it is evident that the linear approximation is only valid for energies below 1 eV.

1.4 Aharonov-Bohm effect

The Aharonov-Bohm effect (AB) is an interference phenomenon in which a charged particle acquires a phase by moving in an electromagnetic potential. The most interesting feature of the AB effect is that gauge potentials, which were for a long time considered as only mathematical constructs, could lead to measurable effects such as electron interference. A simple thought experiment proposed by Yakir Aharonov and David Bohm in their 1959 paper¹⁶ explains how electron wave functions are affected by potentials even when they move in regions where no electrical or magnetic forces act on them. In this subsection we introduce the AB effect by summarizing one of the two thought experiments proposed in Ref. [16]. According to this reference, a general phase picked by a charged particle traveling along a closed space-time path l is equal to

$$\Delta\varphi = \frac{e}{\hbar} \oint_l (\phi dt - \mathbf{A} \cdot d\mathbf{r}/c), \quad (1.9)$$

where ϕ and \mathbf{A} are scalar and vector potentials. A more special case is the time-independent one, considered in Fig. 1.6. An electron beam is split in two paths moving along opposite sides of a narrow solenoid which creates a nonzero flux only in the center of the system, while the vector potential is present in the entire space. The electron wave traveling along these two paths acquires a different phase, and this phase is proportional to the action S along each path. The two wave functions (for two paths) at the interference region can be written as

$$\psi_1 = \psi_1^0 e^{-iS_1/\hbar}, \quad \text{and} \quad \psi_2 = \psi_2^0 e^{-iS_2/\hbar}. \quad (1.10)$$

Here, ψ_1^0 and ψ_2^0 are the wave functions for the case when no flux penetrates the system. The phase difference between the two interfering waves is

$$\Delta\phi = (S_2 - S_1)/\hbar = \frac{e}{c\hbar} \left(\int_{l_1} \mathbf{A} \cdot d\mathbf{r} - \int_{l_2} \mathbf{A} \cdot d\mathbf{r} \right) = \frac{e}{c\hbar} \oint_{l_1-l_2} \mathbf{A} \cdot d\mathbf{r}. \quad (1.11)$$

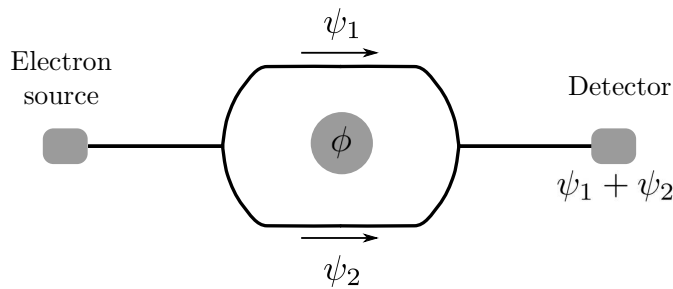


Figure 1.6: Scheme of the device proposed to measure the Aharonov-Bohm effect: A beam of electrons is split into two paths surrounding a nonzero flux thread. Electron wave function can be split into two parts ψ_1 , and ψ_2 corresponding to two paths the electron can take in the system. The two paths are then merged and a detector is placed in the interference region. This experiment is somewhat similar to a two-slit experiment, but instead of measuring interference minima and maxima in real space, they are mapped as a function of a changing magnetic flux.

Taking into account Stokes theorem, the circulation of \mathbf{A} on a closed path l is equal to the magnetic flux enclosed by l

$$\oint_l \mathbf{A} \cdot d\mathbf{r} = \int_S (\nabla \times \mathbf{A}) \cdot \mathbf{n} dS = \int_S \mathbf{B} \cdot \mathbf{n} dS = \phi. \quad (1.12)$$

Here, S is the surface enclosed by l and \mathbf{n} is the surface normal vector. Based on this the phase difference is proportional to the magnetic flux passing through the system. By changing the flux strength, the phase difference between the two interfering electron paths changes from constructive to destructive. Therefore, the total electron transmission probability changes depending on the flux through the system.

The most important message of this thought experiment (which has been realized in several experimental setups) is that no magnetic field acts on electrons as they circle around the system. The other setup presented in Ref. [16], deals with electrons moving in a time varying scalar potential. Aside of the Aharonov-Bohm effect there is its dual known as the Aharonov-Casher effect, where a charge-neutral particle with spin travels around a line of charge and gains an additional phase.

1.5 Scanning gate microscopy

The invention of the optical microscope greatly improved our understanding of the physical phenomena on length scales comparable to the wavelengths of the visible part of the spectrum. With increase in energy of used particles and decrease in wavelength, even smaller features were revealed — such as the crystal structure of solids, and ultimately the composition of atomic nucleus and its constituent particles. With the invention of scanning tunneling microscopy mentioned above,¹⁰ a completely new class of microscopy techniques suitable for nanoscale measurements came into the existence. The basic idea behind all scanning techniques is more or less the same, a probe (similar to that presented in Fig. 1.7) is brought in close proximity of a material surface. Depending on the applied technique, position of the probe is connected with some local property, which allows for the spatial mapping of this local property. In case of scanning tunneling microscopy, a voltage biased metallic probe is brought very close to the sample, and it measures the strength of the tunneling current (therefore the word “tunneling” in STM) into the sample. The current decreases exponentially with the tip height, and this dependence is used to position the tip very close to the sample at constant height. This is achieved by locking the current, in other words by adjusting the tip height so the current is kept constant. Keeping the distance between the tip and the sample constant allows for scanning of the sample surface topography. This method is very precise and is used to image arrangements of individual atoms in a crystal lattice. Another technique is the so-called atomic force microscopy (AFM). In contrast to STM, what is measured in AFM scans is the force acting between a tip and a sample. The force bends the arm holding an AFM and this deflection is measured using a laser pointed to the top of the AFM tip. Instead of a constant tunneling current, the tip is now locked to a constant force. This method can be also applied to image sample topography.

The method we are mostly interested in this thesis is known as *scanning gate microscopy* (SGM). Ever since its early applications in imaging electron transport,^{17,18} SGM was used to study 2DEG buried under insulating surfaces. Connection between the tip and the sample is established through capacitive coupling, and not through direct tip-sample contact. In other words, the tip changes the electron density beneath it, which manifests as an induced electrical potential. In case of graphene, the tip can be placed very close to the conducting layer, or it can be coated with a dielectric¹⁹ and

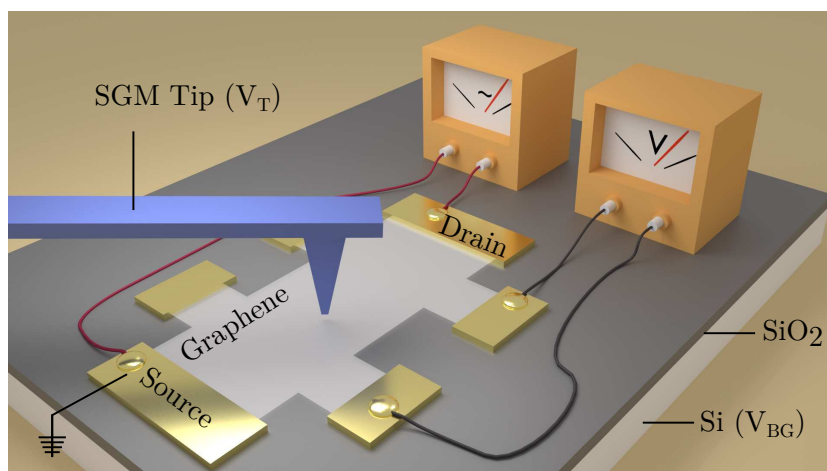


Figure 1.7: A simplified scheme of an SGM experiment of a graphene 6-terminal Hall bar. A biased SGM tip is scanning the graphene sample placed on top of the SiO_2 layer. Current is injected into the source contact and extracted from the drain contact, while the voltage is measured across the device. The graphene electron density (and consequently the Fermi energy) is controlled through the voltage on the back gate (V_{BG}).

placed in direct contact with the sample. In some experimental setups a layer of hexagonal boron-nitride (h-BN) is placed on top of graphene.²⁰ The basic idea behind all SGM measurements is the same. The device conductance (or resistance) is measured simultaneously as the tip is scanned over the sample. The tip-induced potential perturbs the passage of electrons. Since the tip acts as a movable gate, this technique can be used to study localization effects in quantum dots and in narrow constrictions. As we explain later, the interpretation of SGM resistance maps varies depending on the particular device setup and characteristics. In some cases, the interpretation is that the tip is mapping the local flow,¹⁷ while in others it is believed to map the local density of states.^{21,22} In case of experiments on quantum dots and constrictions,^{23,24} the tip can be used to map the distribution of energy levels in a quantum dot. The energy levels manifest in real space as concentric haloes distributed around the localization point. On the other hand, these distributions reveal the equipotential lines of the tip induced potential, and the quantum dot is used as a primitive potentiometer for measuring the tip potential.

In Fig. 7.9 we present a characteristic SGM map showing branched flow

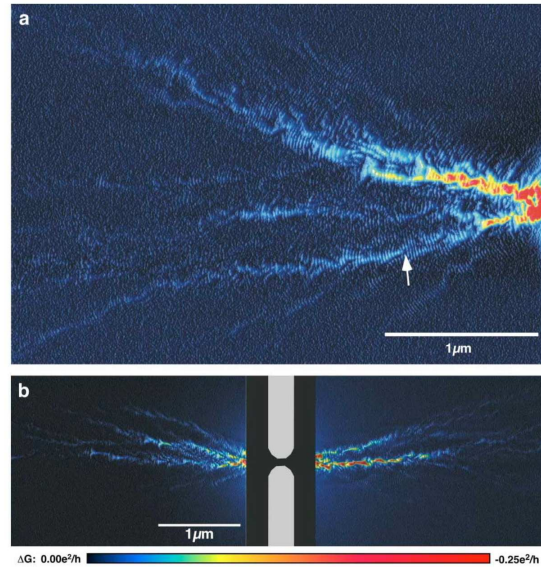


Figure 1.8: SGM conductance map showing branched flow around a quantum point contact in GaAs/AlGaAs 2DEG. Figure taken from Ref. [26].

coming out of a QPC.

Some progress in interpreting SGM maps has been made so far.²⁵ In the case of a weak tip potential, the conductance correction due to a local tip perturbation was calculated up to the second order. The expansion was applied to a specific case of quantum point contact (QPC), but it is also valid in other geometries. The first-order correction term is dominant only at a conductance step, when a new mode opens in the system, and depends mostly only on transmission of this new mode. On the other hand, the second order correction is more dominant at the conductance plateau, and depends on the transmissions of all open modes. Although this interpretation of the SGM maps is valid only in the perturbative regime, some conclusions should still apply in the other regime, when the SGM tip depletes the two-dimensional electron gas.

1.6 Motivation and organisation of the thesis

This thesis deals with electrical transport in micro- and nano-systems made either from conventional 2DEG or from graphene. The main motivation for

this work is to understand the influence of external potential perturbations on electron transport in nano-sized devices. This is particularly related to the SGM experiments. Understanding how the SGM tip interacts with the sample can help not only to interpret the present experiments, but possibly design new ones. The ultimate goal of the SGM technique is to use the measured conductance maps to obtain local properties, e.g. spatial distributions of currents in a scanned sample. Since these local properties are not known in advance, it is our goal to guide the experiments by giving comparisons of simulated local properties with the simulated conductance maps.

Although we provide some insights, a lot more questions remain unanswered and they require further research. For example, if tip dependent conductance is related to some of the local properties, then there must be some sort of transforming function that relates that property with the conductance. In other words, the tip influence can be interpreted as a convolution of the initial function (e.g. current density) with the tip potential. If such transforming function exists, then interpretation of SGM maps would involve the deconvolution of the measured conductances in order to obtain that local property which is related to the conductance. Again, some progress in finding this relation has been made in the case of a weak tip potential.²⁵ It was shown that first-order and second-order correction terms in the conductance depend on the integrals connecting the tip potential with the scattered states in the leads.

The second, but equally significant question is to understand transport in nanostructured graphene under the influence of external electric and magnetic fields. Due to its gapless nature and its massless charge carriers, but also due to the edge and valley effects, graphene behave very differently than classical 2DEG. Even for interpretations of the SGM experiments, it is important to understand the transport physics of graphene (e.g. intervalley scattering, edge states, snake states, Klein tunneling etc.).

This thesis is organised as follows. After a brief introduction to graphene and 2DEG, and the phenomena encountered in nanostructures made from these materials, we proceed by investigating some of the special cases related to some specific geometries. In Chapter 2 we present the theoretical framework used to calculate the transport properties, and then in the next five chapters we discuss the application of this framework for specific cases. Chapter 3 deals with scanning gate microscopy of small Aharonov-Bohm rings, where we apply the wave-packet approach to calculate the device conductances. Our initial idea was to study scanning gate microscopy in

graphene, but in order to gain some familiarity with graphene, we first turn to some simpler cases. In Chapters 4, 5, and 6 we focus on transport in graphene nanoribbons and Hall bars without the SGM tip. Chapter 4 deals with resonance effects in narrow graphene ribbons exposed to two side gates. This chapter emphasizes the differences coming from the different edge types a graphene sample can have. Also, in the ending section we briefly touch on effects due to vacancy disorder. Chapter 5 further investigates the effects of vacancy disorder but in strong magnetic fields. We demonstrate that vacancy disorder affects quantum Hall measurements by inducing new states in the Landau spectrum. In Chapter 6, a remarkable effect of current guiding is studied in a Hall bar geometry. We propose a simple picture which explains the current flow along the guided (snake) states. The guiding leads to an interesting quantization of the bend resistance, and in the absence of backscattering we are able to calculate the quantized resistances analytically. Lastly, we simulate some of the recent scanning gate experiments in graphene in micrometer scaled devices. We differentiate between several different regimes in which a scanning gate tip can operate in graphene, and investigate each of them separately. Due to the large system size, we give a comparison between results obtained in quantum and classical simulations.

CHAPTER 2

Theoretical background

In this chapter we discuss the main theoretical frameworks used to study electrical transport in nanodevices. We start with Landauer formula, connecting the conductance of a nanostructure with the electron transmission. Next, we expand this basic idea to the case of a multiterminal device, and we introduce Büttiker's formula. These formulas can be applied only if the full device transmission matrix is known, and there are several ways to obtain this matrix. One of them is the non-equilibrium Green's functions method (NEGF), which we describe in this chapter, the other is the wave packet propagation method, which we describe in the next chapter. Since most of our numerical results are obtained using KWANT [27], a Python package for quantum transport simulations, we dedicate one part of this chapter to KWANT.

2.1 Landauer-Büttiker formalism

2.1.1 Landauer formula

Most of the concepts that we present in this subsection are based on Refs. [28, 4]. The idea that the conductance of a device is proportional to the probability that the charge carriers travel through it seems very intuitive. It is

2.1. Landauer-Büttiker formalism

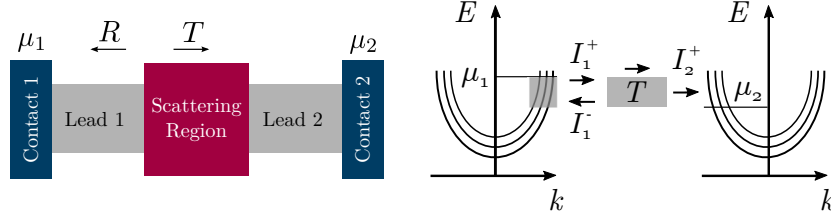


Figure 2.1: Two terminal device (left), and electron band structure in left and right lead of the system (right).

well known that the conductance of a large conductor scales as

$$G = \sigma W/L, \quad (2.1)$$

where σ is the conductivity of the material, L is its length, and W is its width. Based on this formula, the conductivity of a short ballistic conductor would converge to infinity as its length decreases (its resistance would converge to zero). However, this is not what is measured. No matter how short or narrow a conductor is, there is always some resistance R_c which could not be eliminated. This is the so called *contact resistance*. Another feature of the narrow conductors is that their conductance becomes quantized, which is due to the existence of a discrete set of transversal modes. The contact resistance R_c can be connected with the number of transverse modes M through the relation

$$R_c = \frac{h}{2e^2} \frac{1}{M} = \frac{12.9k\Omega}{M}. \quad (2.2)$$

Both of these features, the contact resistance and the transverse quantization, are incorporated in the Landauer formula.

The Landauer formula deals with a two terminal device, as that presented on the left side of Fig. 2.1. The chemical potential for electrons in the left contact is μ_1 , and for electrons in the right contact it is μ_2 . Electrons from both contacts can travel to the opposite side through the main scattering region. The dispersion relations in the leads are presented on the right side of Fig. 2.1. The conductance of the device is determined by the behaviour of electrons with energies between μ_1 and μ_2 . If contacts are reflectionless, meaning that the outgoing electrons do not backscatter, than the right-going electrons in the left lead (lead 1) all originate from the left contact, and they all have electrochemical potential μ_1 . Also, the left-going electrons in the right lead (lead 2) all have electrochemical potential μ_2 , and they all originate from the right contact.

The right-going current in the left lead is then

$$I_1^+ = \frac{2e}{h} M(\mu_1 - \mu_2), \quad (2.3)$$

and the left-going current is simply the current reflected from the scattering region (since there is no left-going current from the right contact for energies above μ_2)

$$I_1^- = \frac{2e}{h} M(1 - T)(\mu_1 - \mu_2). \quad (2.4)$$

Similarly, the right-going current in the right lead (lead 2) is

$$I_2^+ = \frac{2e}{h} MT(\mu_1 - \mu_2). \quad (2.5)$$

The conductance is then

$$G = \frac{I_2^+}{(\mu_1 - \mu_2)/|e|} = \frac{I_1^+ - I_1^-}{(\mu_1 - \mu_2)/|e|} = \frac{2e^2}{h} MT. \quad (2.6)$$

Previous expression is only valid when the temperature is equal to zero, and there are M transverse modes in the system with approximately equal transmission probabilities (T) in the considered energy range. For example, if transmissions are not equal, then the conductance is given by

$$G = \frac{2e^2}{h} \sum_{i=1}^M T_i, \quad (2.7)$$

where T_i is the transmission probability of the i -th mode. In case of nonzero temperature, the energy distributions of electrons in the contacts are no longer given by a Heaviside step function. Instead of all states below the contact chemical potential being occupied, the occupation is now spread in energy and given by the Fermi-Dirac distribution

$$f(E, \mu) = \frac{1}{\exp[(E - \mu)/k_B T] + 1}. \quad (2.8)$$

Assuming that transmissions change with energy, and that each mode has a different transmission T_i , a more general current formula can be written as

$$I = \frac{2e}{h} \sum_{i=1}^M \int T_i(E) [f_1(E) - f_2(E)] dE. \quad (2.9)$$

2.1. Landauer-Büttiker formalism

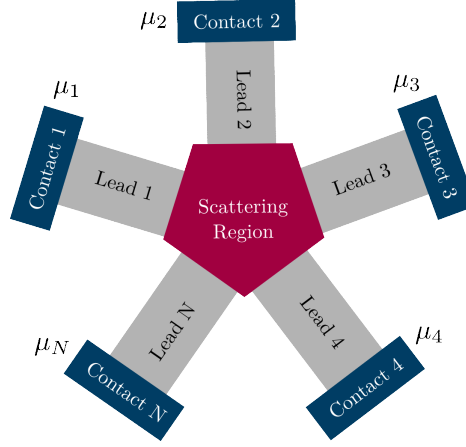


Figure 2.2: A multi-terminal device with N contacts and N leads. The electrochemical potential on the i -th contact is μ_i .

It is obvious that for equal chemical potentials on the two contacts, the system is in equilibrium ($f_1(E) = f_2(E)$), and there is no net current flowing. For small bias $\mu_1 - \mu_2$, the current can be expanded around the equilibrium point as

$$\delta I = \frac{2e}{h} \sum_{i=1}^M \int T_i(E) \delta [f_1(E) - f_2(E)] dE. \quad (2.10)$$

Here, the expansion around δT_i is not necessary, since $f_1(E) - f_2(E) = 0$ at equilibrium. The term $\delta [f_1(E) - f_2(E)]$ can be rewritten as

$$\delta [f_1(E) - f_2(E)] = \left(-\frac{\partial f(E)}{\partial E} \right) (\mu_1 - \mu_2) \quad (2.11)$$

giving a linear response current

$$\delta I = \frac{2e}{h} \sum_{i=1}^M \int T_i(E) \left(-\frac{\partial f}{\partial E} \right) (\mu_1 - \mu_2) dE, \quad (2.12)$$

from which we can obtain the conductance.

$$G = \frac{\delta I}{(\mu_1 - \mu_2) |e|} = \frac{2e^2}{h} \sum_{i=1}^M \int T_i(E) \left(-\frac{\partial f}{\partial E} \right) dE. \quad (2.13)$$

2.1.2 Büttiker multi-terminal formula

The Landauer conductance formula was generalized by Büttiker to include multi-terminal devices. For a N -terminal device, such as that presented in Fig. 2.2, there are several combinations in which the current and voltage probes can be connected to the device. Therefore in order to properly describe any measurements, it is necessary to specify where the measuring probes are attached. For example, $G_{ij,km}$ is the conductance measured when the current probe is attached on contacts i and j , and voltage is measured between contacts k and m . Since any terminal can be either voltage or current probe, the basic idea is to treat all terminals on equal footing.

For the zero temperature case, the current in the p -th lead can be written as

$$I_p = \frac{2e}{h} \sum_q [\bar{T}_{q \leftarrow p} \mu_p - \bar{T}_{p \leftarrow q} \mu_q], \quad (2.14)$$

where $\bar{T}_{q \leftarrow p}$ is a sum of transmissions over all transverse modes that originate from the p -th lead and scatter to some mode in the q -th lead

$$\bar{T}_{q \leftarrow p} = \sum_{m \in q} \sum_{n \in p} T_{m \leftarrow n}. \quad (2.15)$$

Based on Eq. 2.14, the current in lead p consists of two parts: the first part represents the outgoing current, originating from contact p , while the second part represents the incoming current, originating from all other contacts and being drained to contact p .

Previous current formula can be rewritten using the relations $V_i = \mu_i/e$, and $(2e^2/h)T_{pq} = G_{pq}$:

$$I_p = \sum_q [G_{qp} V_p - G_{pq} V_q]. \quad (2.16)$$

If we set potentials on all gates equal, then the current in lead p is equal to zero

$$I_p = \sum_q [G_{qp} - G_{pq}] V_p = 0, \quad (2.17)$$

from which it follows $\sum_q G_{qp} = \sum_q G_{pq}$. Since V_p is constant in Eq. (2.16), then $\sum_q G_{qp} V_p = \sum_q G_{pq} V_p$ and therefore the previous sum can be rewritten as

$$I_p = \sum_q G_{pq} [V_p - V_q]. \quad (2.18)$$

Grouping expressions for all N leads, the general current-voltage relation can be written in matrix form.

$$\begin{pmatrix} I_1 \\ I_2 \\ \vdots \\ I_N \end{pmatrix} = \begin{pmatrix} \sum_i G_{1i} & -G_{12} & \cdots & -G_{1N} \\ -G_{21} & \sum_i G_{2i} & \cdots & -G_{2N} \\ \cdots & \cdots & \cdots & \cdots \\ -G_{N1} & \cdots & \cdots & \sum_i G_{Ni} \end{pmatrix} \begin{pmatrix} V_1 \\ V_2 \\ \vdots \\ V_N \end{pmatrix}. \quad (2.19)$$

The sums in previous matrix do not include the diagonal terms (G_{ii}). These sums can be rewritten as $\sum_{i \neq P} G_{iP} = G_0(M - T_{PP})$, where M is the total number of modes in a lead, and T_{PP} is a reflection coefficient. The resistances can be obtained by inverting the conductance matrix

$$\begin{pmatrix} V_1 \\ V_2 \\ \vdots \\ V_N \end{pmatrix} = \begin{pmatrix} R_{11} & R_{12} & \cdots & R_{1N} \\ R_{21} & R_{22} & \cdots & R_{2N} \\ \cdots & \cdots & \cdots & \cdots \\ R_{N1} & R_{N2} & \cdots & R_{NN} \end{pmatrix} \begin{pmatrix} I_1 \\ I_2 \\ \vdots \\ I_N \end{pmatrix}. \quad (2.20)$$

For nonzero temperatures, the expression for the current is

$$I_p = \frac{2e}{h} \sum_q \bar{T}_{pq}(E) [f_p(E) - f_q(E)], \quad (2.21)$$

where the transmission functions are defined as in Eq. (2.15)

Similarly to the two-terminal case, the conductance for small bias can be calculated as

$$G_{pg} = \frac{2e^2}{h} \int \bar{T}_{pq}(E) \left(-\frac{\partial f_0}{\partial E} \right) dE \quad (2.22)$$

2.2 S-matrix and Green's functions

One way to obtain transmissions in a device is through the application of Green's functions. In order to explain Green's functions, first we need to explain the scattering matrix. The scattering matrix (or S matrix) relates modes which enter the device, with the ones which exit from it. For each incoming mode a_j , there is an amplitude s_{ij} that this mode will scatter into an outgoing state b_i . The transmission from a_j to b_i is then $T_{ij} = |s_{ij}|^2$. In matrix representation, the S matrix can be written as

$$\begin{pmatrix} b_1 \\ b_2 \\ \vdots \\ b_N \end{pmatrix} = \begin{pmatrix} s_{11} & s_{12} & \cdots & s_{1N} \\ s_{21} & s_{22} & \cdots & s_{2N} \\ \cdots & \cdots & \cdots & \cdots \\ s_{N1} & s_{N2} & \cdots & s_{NN} \end{pmatrix} \begin{pmatrix} a_1 \\ a_2 \\ \vdots \\ a_N \end{pmatrix} \quad (2.23)$$

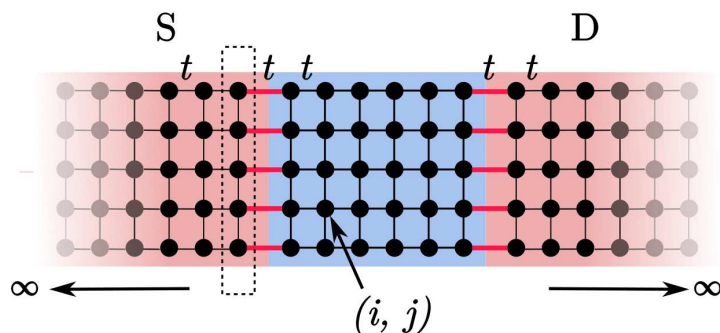


Figure 2.3: Discretized two-terminal device consisting of two semi-infinite leads (colored red), both connected to a main scattering region (colored blue). Each site in the main region can be labeled using two indices (i, j) , and the distance between neighbouring sites is a . Hopping between sites is constant, and equals t . The dashed rectangle marks the lead unit cell.

Knowing the S matrix of a system allows one to calculate transmissions for all modes, and from there (using Landauer-Büttiker formulas) obtain the conductances. Scattering matrix is usually obtained from the system Green's function. Therefore the general scheme for obtaining the conductances is the following

$$\hat{H} \rightarrow G^{R(A)}(x, x') \rightarrow S \rightarrow \bar{T}(E) \rightarrow G.$$

Namely we start from the system Hamiltonian \hat{H} (usually in a discretized form) and after solving the inverse problem, we obtain the system Green's function $G^{R(A)}(x, x')$. This Green's function is then used to obtain the S -matrix and transmissions $\bar{T}(E)$, and consequently the conductance G .

As shown in Eq. (2.24), the first step in calculating the conductance is in obtaining the Green's function from the Hamiltonian of the system. Green's functions are usually used as a tool to solve equations of the general form

$$DR = S, \quad (2.24)$$

where R is the response function to some excitation S , and D is a differential operator. In order to find the solution of this system R , it is necessary to find the operator G such that

$$GS = R. \quad (2.25)$$

From here, it follows

$$G = D^{-1} \quad \text{or} \quad GD = 1. \quad (2.26)$$

In the context of quantum mechanics, the equation we are interested in is

$$\left[E - \hat{H}\right] \Psi = S, \quad (2.27)$$

where we would like to know what is the response function of the system Ψ , caused by an excitation coming from the leads S . In other words, what is the probability distribution inside the system, for an electron originating from the leads. The inverse of the differentiation operator is

$$G = \left[E - \hat{H}\right]^{-1} \quad (2.28)$$

and it is the Green's function of our system. There are always two solutions to Eq. (2.28), corresponding to two boundary conditions. One is called advanced, and the other is called retarded Green's function, and they are usually labeled as G^A , and G^R . By adding or subtracting a small imaginary number $i\eta$, the two boundary conditions (of an incoming or outgoing waves) can be imposed on the system. This is very useful in numeric calculations, since in general the inverting procedures are usually iterative in nature, and during iterations both solutions (retarded or advanced) could be obtained. By adding an infinitesimal $\pm i\eta$ the iteration process is then driven to converge towards one specific solution.

The Hamiltonian in previous equations can be represented in real space as

$$\hat{H}\Psi(x, y) = \left[-\frac{\hbar^2}{2m} \left(\frac{\partial^2}{\partial x^2} + \frac{\partial^2}{\partial y^2}\right) + U(x, y)\right] \Psi(x, y), \quad (2.29)$$

and it can be discretized. Imagine that a two-terminal conductor, e.g. the one presented in Fig. 2.3, is divided in an array of lattice points, each separated from its neighbours by a distance a . Then all points (x, y) can be labeled by indices (i, j) , and previous equation can be rewritten in a discrete form

$$\left[\hat{H}\Psi\right]_{ij} = -\frac{\hbar^2}{2m} \frac{1}{a^2} \left[\Psi_{(i-1)j} + \Psi_{(i+1)j} + \Psi_{i(j-1)} + \Psi_{i(j+1)} - 4\Psi_{ij}\right] + U_{ij}\Psi_{ij}.$$

Here, the second order derivatives are replaced with their finite difference counterparts. For every point (i, j) , there are four terms $-\frac{\hbar^2}{2ma^2} = t$, connecting that point with its neighbours, and one term $(U_{ij} - 4t)$ for the on-site energy.

Inverting this Hamiltonian might seem like a straightforward problem, however this is not the case. Since the two leads are semi-infinite, the system

contains an infinite number of sites, and thus the dimension of the Hamiltonian is infinite. One way to approach this problem is to separate parts that deal with the main scattering region (which is finite), and the infinite leads. Similarly as in Ref. [4], we will present this separation for a system with only one lead attached, and then extend it to the case of a multi-lead device.

For an open system with a single semi-infinite lead, the discretized Hamiltonian matrix can be divided in two parts

$$\hat{H} = \begin{bmatrix} H_l & \tau \\ \tau^* & H_S \end{bmatrix}, \quad (2.30)$$

where H_l is the infinite Hamiltonian of the lead, H_S is the Hamiltonian of the scattering region, and τ is the hopping matrix that connects the lead with main region (hoppings marked with red in Fig. 2.3). Green's function in this case will also be divided into several parts.

$$\begin{bmatrix} G_l & G_{lS} \\ G_{Sl} & G_S \end{bmatrix} = \begin{bmatrix} (E + i\eta)I_l - H_l & \tau \\ \tau^* & (EI_S - H_S) \end{bmatrix}^{-1} \quad (2.31)$$

which could also be written as

$$\begin{bmatrix} (E + i\eta)I_l - H_l & \tau \\ \tau^* & (EI_S - H_S) \end{bmatrix} \begin{bmatrix} G_l & G_{lS} \\ G_{Sl} & G_S \end{bmatrix} = I. \quad (2.32)$$

From this system of equations we obtain

$$[(E + i\eta)I_l - H_l] G_{lS} + \tau G_S = 0, \quad (2.33)$$

$$\tau^* G_{lS} + [EI_S - H_S] G_S = I. \quad (2.34)$$

From here, Eq. (2.33) gives

$$G_{lS} = -[(E + i\eta)I_l - H_l]^{-1} \tau G_S, \quad (2.35)$$

$$G_{lS} = -g_l^R \tau G_S, \quad (2.36)$$

where g_l^R is the Green's function in the lead. Replacing this in Eq. (2.34), we obtain

$$G_S = [EI_S - H_S - \tau^* g_l^R \tau]^{-1} \quad (2.37)$$

In other words, the Green's function of the scattering region can be obtained if the Green's function of the lead is known. Term $\tau^* g_l^R$ is sometimes marked as Σ^R , and called the lead self-energy. It is a finite term, since the matrix

that connects the system with the lead (τ) reduces the leads Green's function only to those sites which are actually connected to the scattering region.

For a multi-lead system, the self-energy can be expressed as

$$\Sigma^R = \sum_p \Sigma_p^R, \quad (2.38)$$

where Σ_p^R is the self-energy of the p -th lead, and the Green's function of the scattering region is then,

$$G_S = [EI_s - H_s - \Sigma^R]^{-1} \quad (2.39)$$

Connection between scattering matrix and Green's function is given in Ref. [29]. This is known as the Fisher-Lee relation. The transmission function \bar{T}_{pq} can be expressed as

$$\bar{T}_{pq} = \text{Tr} [\Gamma_p G_S^R \Gamma_q G_S^A], \quad (2.40)$$

where matrices Γ_p and Γ_q can be related to the lead self-energies

$$\Gamma_p = i [\Sigma_p^R - \Sigma_p^A]. \quad (2.41)$$

2.3 KWANT

The Green's function method is only one way to obtain the elements of the scattering matrix. In order to calculate the resistances using Green's functions, two problems need to be solved. The first problem is finding the Green's functions of the leads g_l^R , and the second is finding the Green's function of the main scattering region G_S . For example, the first problem can be solved by dividing the leads into unit cells, and then using some iteration scheme to compute the Green's functions on the surface. One of the ways to solve the second problem is by direct inversion of the Hamiltonian matrix, although this might be computationally demanding in systems with larger number of atoms. Most of the numerical results presented in this thesis were obtained using KWANT. KWANT is a software package developed in the Python language, and its main purpose is to implement methods to obtain the main transport quantities (S -matrix, propagating modes, lead dispersions, wave functions) on a system defined in the tight-binding model. Although it can be used to obtain Green's functions, the default method used by KWANT is the so-called *wave function* method. In this part, we

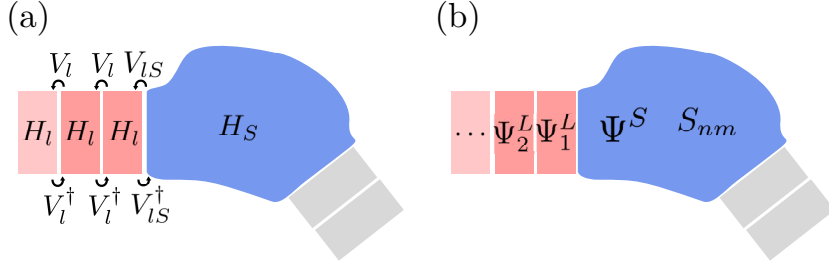


Figure 2.4: (a) Hamiltonian submatrices corresponding to the scattering region (blue) and one lead (red). (b) Wave functions in the lead Ψ^L , and in the main scattering region Ψ^S .

give some main features of this method. This explanation is completely based on Ref. [27], which additionally explains the main usage cases.

The basic problem remains the same as that presented in previous subsection. That is solving the eigenvalue problem of an open system with semi-infinite leads. The case considered in Ref. [27] is that of a system with a single lead, as presented in Fig. 2.4, but the problem can be easily generalized to a multi-lead system. The Hamiltonian matrix in this case is also infinite

$$\hat{H} = \begin{pmatrix} \ddots & V_l & & & \\ V_l^\dagger & H_l & V_l & & \\ & V_l^\dagger & H_l & V_{lS} & \\ & & V_l^\dagger & H_S & \end{pmatrix}, \quad (2.42)$$

where H_S is the Hamiltonian of the main scattering region, and H_l is the Hamiltonian of the lead unit cell. Hopping matrices V_l , and V_{lS} connect two neighbouring unit cells in the lead, and the lead surface with the surface of the system, respectively (see Fig. 2.4). Similarly to the Hamiltonian, the wave function in the system can be divided into parts belonging to the lead ($\Psi^L(i)$, $i = 1, 2, \dots$) and a part belonging to the main scattering region Ψ^S . Since away from the main scattering region the lead is translationally invariant, the wave function can be written as a superposition of the eigenstates of the translation operator. The eigenstate wave functions ϕ_n can be decomposed into two parts

$$\phi_n(j) = (\lambda_n)^j \chi_n, \quad (2.43)$$

where χ_n is the transversal part for the n -th eigenstate, and λ_n^j is a longitu-

dinal part. Previous states are the eigenstates of the system of equations

$$\left(H_l - V_l \lambda_n^{-1} - V_l^\dagger \lambda_n \right) \chi_n = E \chi_n, \quad (2.44)$$

and depending on the value of λ_n , they describe evanescent modes ($|\lambda_n| < 1$), or propagating modes ($\lambda_n = e^{ik_n}$).

Using these precalculated eigenmodes, the wave function in the lead can be written as

$$\Psi_n(i) = \phi_n^{\text{in}}(i) + \sum_m S_{nm} \phi_m^{\text{out}}(i) + \sum_m \tilde{S}_{np} \phi_p^{\text{ev}}(i). \quad (2.45)$$

Inserting this equation back in the previous Hamiltonian, due to the fact that we are using eigenstates of the infinite part of the Hamiltonian reduces the problem to solving the part inside of the main scattering region. This is done by wave function matching, where the coefficients of the S -matrix are obtained in such a way that the wave functions on the lead-system interface match.

CHAPTER 3

Scanning gate microscopy of 2DEG Aharonov-Bohm rings in weak magnetic fields

3.1 Scanning gate microscopy of 2DEG rings

In the introductory chapters, we briefly described the basic principles of scanning gate microscopy (SGM), a measuring technique that uses a charged tip of the atomic force microscope (AFM) to scan two-dimensional nanostructured systems. In this chapter* we study the electron transport inside a small 2DEG ring by applying the wave packet dynamics method. As demonstrated in Ref. [23], a tip-induced local potential perturbs the transport of electrons at low temperatures (see Fig. 3.1(a) which shows experimentally measured tip-induced potential). This is reflected in an overall conductance, which now becomes dependent on the tip position. This technique was successfully used to study electron transport in quantum point contacts (QPC) [17, 21, 30], quantum rings (QR) [31, 32, 33], Hall bars [34], quantum dots [35], and quantum billiards [36].

Experiments on quantum rings (Refs. [31, 32, 33]) showed two types of conductance oscillations: radial fringes—when the tip was located directly

*Results presented in this chapter are based on our publication: M. D. Petrović, F. M. Peeters, A. Chaves, G. A. Farias, *Conductance maps of quantum rings due to a local potential perturbation*, Journal of Physics: Condensed Matter 25, 495301 (2013).

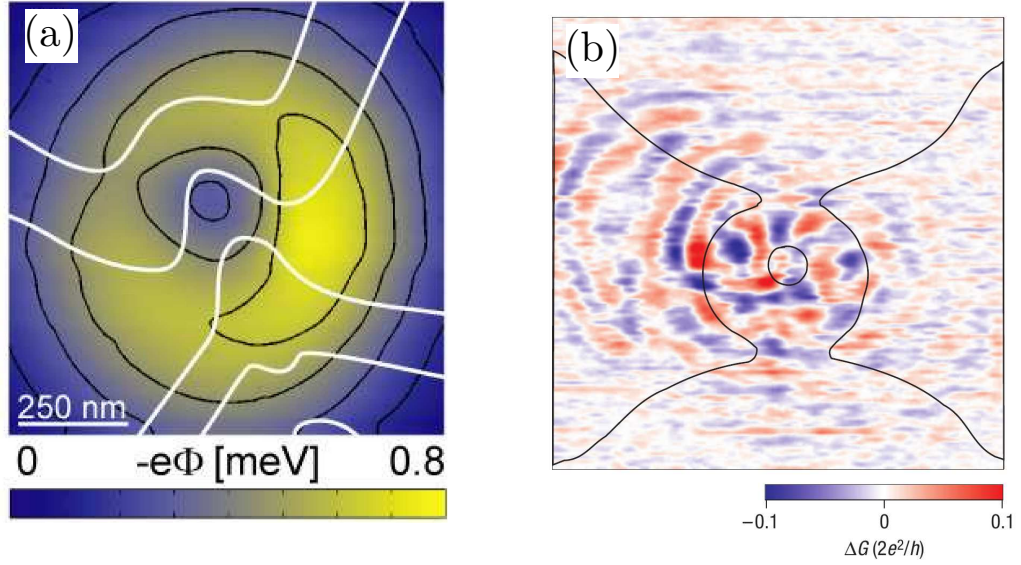


Figure 3.1: (a) Measured tip-potential profile (figure taken from Ref. [23]). The white curves outline the regions where 2DEG is depleted by oxidation to produce a quantum dot. (b) SGM map of a quantum ring (figure taken from Ref. [31]). According to Ref. [31] the inner and outer radius of the ring in (b) are 210 nm and 600 nm, respectively.

above the ring, and concentric fringes—when the tip was moved away from the ring. In Fig. 3.1(b) we present an experimentally measured SGM map taken from Ref. [31]. The map shows previously mentioned two types of conductance oscillations. Only the conductance change is shown (ΔG), there is a high background conductance which is subtracted from the map, and which is not shown. Reference [31] reported background conductance of $G_0 \approx 7.5 2e^2/h$. The interpretation of these experiments was that the radial fringes originate from the tip influence on semi-classical electron trajectories, while the concentric fringes were connected with the change in the electron phase. It was also demonstrated that a perpendicular magnetic field causes the occurrence of Aharonov-Bohm [16] conductance oscillations.

Although there is a considerable amount of data available from SGM measurements, a clear interpretation of these data, and a connection with the local properties, is still missing. Ref. [37] treated SGM experiments from a theoretical point of view, and studied symmetric, abrupt quantum point contact. Connection between the conductance change and the current den-

sity was demonstrated, but only in this specific geometry. Previous studies of quantum rings [21, 32, 22] showed that there is a relation between the local density of states (LDOS) at the Fermi energy and the recorded conductance maps. This was done for a weak perturbing potential which did not significantly change the distribution of energy levels in the system. In a recent theoretical work by B. Szafran [38], these results were confirmed and extended to a strongly interacting tip. With screening included, the tip potential was calculated even when the tip was not directly above the ring. The perturbing potential was shown to be anisotropic, but along the ring arms it could be approximated with a Lorentzian function. Additionally, a recent study [39] investigated the interference effects coming from charge disorder. In the following, we will extend these findings, and explain the origin of oscillating features in the conductance maps. We will show that tip does not influence all modes equally.

In this chapter, extend the previous study of quantum rings done by A. Chaves [40], and use the Landauer formula to obtain the two-terminal conductance. In contrast to recent work done by Chwiej and Szafran [41], which focuses on the electron transport in a multi-mode regime, we concentrate only on single, and two-mode occupancy cases. First, we consider single mode transport, which allows us to tell what are the general effects of the tip acting on a single electron state, and what are the main characteristics of the conductance maps obtained in this regime. When placed away from the ring, the tip creates a dynamical phase difference between the two ring arms, causing a change in the conductance and modifying the AB oscillation period. For two occupied subbands, our results suggest the tip is more selective to higher subbands (the subbands appearing at higher energies). Electrons occupying these higher subbands are more perturbed by the tip, which results in a larger conductance change.

Refs. [21, 32, 22] showed that for a weak tip, the measured conductance maps reflect the electron wave functions. Since we deal with a strong perturbing tip (which acts as a scattering center), our conductance maps do not precisely reflect this connection.

The rest of this chapter is organized as follows. In the next section, we define the ring system and present the wave packet method. Next, we present conductance maps for one and two subband occupancy cases. Our findings are summarized at the end of the chapter.

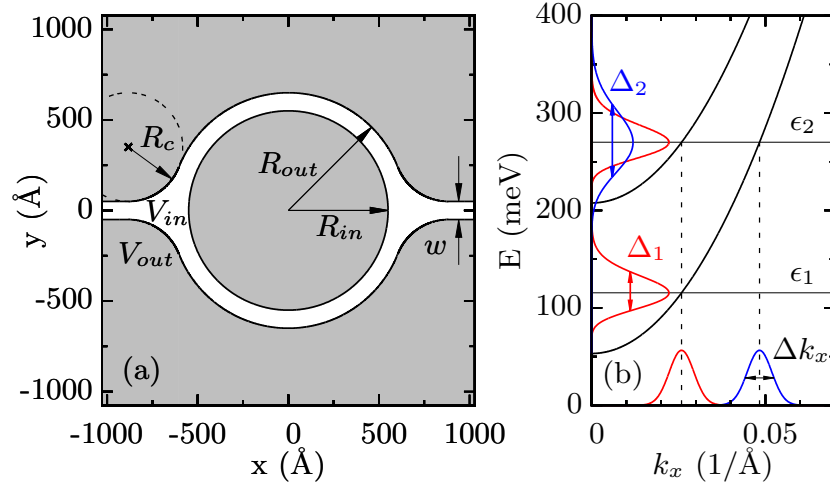


Figure 3.2: (a) Quantum ring system: Radius of the inner circle is $R_{in} = 550 \text{ \AA}$, and of the outer is $R_{out} = 650 \text{ \AA}$. Radius of a circle used to create a smooth lead-ring connection is $R_c = 300 \text{ \AA}$, while the channel width is $w = 100 \text{ \AA}$. Potential outside of the ring is $V_{out} = 600 \text{ meV}$ (gray area), while in the ring is $V_{in} = 0 \text{ meV}$ (white area). (b) Electron dispersion relation for a 100 \AA wide channel. Selected wave packet energies are $\epsilon_1 = 115.4 \text{ meV}$ and $\epsilon_2 = 270 \text{ meV}$, with distribution widths $\Delta_1 = 40 \text{ meV}$ and $\Delta_2 = 75 \text{ meV}$.

3.2 Theoretical model

We consider a quantum ring obtained of e.g. an InGaAs/InAlAs heterostructure with two smoothly connected leads, as shown in Fig. 3.2(a). The dispersion relation for an electron placed inside one of the leads is given by

$$E_n(k_x) = E_n^{(y)} + \frac{\hbar^2(k_x)^2}{2m_e}, \quad (3.1)$$

where $E_n^{(y)}$ is the confinement energy along the y direction (for an electron in the n -th subband), and k_x is the wave vector in the x direction. m_e is the electron effective mass ($m_e = \kappa m_0$), and for InGaAs/InAlAs heterostructures $\kappa = 0.041$.

In the wave packet dynamics approach, the electron wave function is defined for a given geometry in the initial time moment, and then it is propagated using the time evolution operator. In two terminal geometries, the wave packet is usually positioned in one of the leads at the initial time, and

given an initial momentum. By calculating the percentage of the packet that arrives in the output lead, after a sufficient amount of time, the transmission is obtained. The initial wave function for an electron positioned far away from the ring can be written as a product of two independent parts

$$\Psi(x, y) = \psi(x)\phi_n(y). \quad (3.2)$$

Since we define the leads using a finite confinement potential, the energies $E_n^{(y)}$ and functions $\phi_n(y)$ are obtained by numerically solving the 1D Schrödinger equation with the finite difference method. Calculated dispersion relations for the first two subbands are shown with the solid black curves in Fig. 3.2(b). For the wave packet shape in the x direction, we choose a Gaussian function

$$\psi(x) = \frac{1}{\sqrt{\sigma\sqrt{\pi}}} e^{-(x-x_0)^2/(2\sigma^2)} e^{-ik_x x}, \quad (3.3)$$

with the probability density

$$|\psi(x)|^2 = \frac{1}{\sigma\sqrt{\pi}} e^{-(x-x_0)^2/\sigma^2}. \quad (3.4)$$

The wave packet maximum in the initial time moment is positioned at $x_0 = -1100 \text{ \AA}$.

The probability density in the Fourier-inverse space is also a Gaussian

$$|\psi(k)|^2 = \frac{\sigma}{\sqrt{\pi}} e^{-(k-k_x)^2\sigma^2}, \quad (3.5)$$

with width inversely proportional to the packet width in the real space. Full width at half maximum (FWHM) in the x direction is then $\Delta x = 2\sqrt{\ln 2}\sigma$, and in the inverse space $\Delta k_x = 2\sqrt{\ln 2}/\sigma$. For our numerical calculations the parameter σ is set to 200 \AA , hence $\Delta x = 333 \text{ \AA}$ and $\Delta k_x = 0.0083 \text{ \AA}^{-1}$. Since the electron wave vector is given by a probability distribution, and not by a single value, the electron energy is also given by a distribution of possible values. Full width at half maximum of this non-Gaussian distribution is

$$\Delta_n = \frac{\hbar^2}{2m_e} \left[\left(k_x + \frac{\Delta k_x}{2} \right)^2 - \left(k_x - \frac{\Delta k_x}{2} \right)^2 \right] = \frac{\hbar^2}{m_e} k_x \Delta k_x. \quad (3.6)$$

Subband energies for the first two modes are $E_1^{(y)} = 53.2 \text{ meV}$ and $E_2^{(y)} = 207.7 \text{ meV}$. Wave packet energies are set to $\epsilon_1 = 115.4 \text{ meV}$ and $\epsilon_2 = 270 \text{ meV}$, with $\Delta_1 = 40 \text{ meV}$ and $\Delta_2 = 75 \text{ meV}$ (see Fig. 3.2(b)). The

wave packet length determines its spread in energy. Ideally, the wider the packet—the narrower the energy range, but the downside is that propagation time then rises. The chosen value of $\sigma = 200 \text{ \AA}$ is a compromise between the accuracy and the performance.

The wave packet energies are chosen so that the ϵ_2 packet (situated in the second subband) has the same kinetic energy as the ϵ_1 packet (situated in the first subband). This will allow us to study the influence of the confinement energy and the wave packet symmetry on the final conductance maps, since the wave function for the first subband is symmetric, and for the second subband is asymmetric.

We propagate this initial wave function using the time-evolution operator

$$\Psi(x, y, t + \Delta t) = e^{-i\hat{H}\Delta t/\hbar} \Psi(x, y, t), \quad (3.7)$$

expanded as

$$e^{-i\hat{H}\Delta t/\hbar} = e^{-i\hat{V}\Delta t/(2\hbar)} \times e^{-i\hat{T}_x\Delta t/\hbar} \times e^{-i\hat{T}_y\Delta t/\hbar} \times e^{-i\hat{V}\Delta t/(2\hbar)} + O(\Delta t^3). \quad (3.8)$$

Exponents containing the potential operators are ordinary complex numbers, while exponents with \hat{T} operators can be rewritten in the form

$$e^{-i\hat{T}_i\Delta t/\hbar} \approx \left[1 + \frac{i\Delta t}{2\hbar} \hat{T}_i \right]^{-1} \left[1 - \frac{i\Delta t}{2\hbar} \hat{T}_i \right], \quad (3.9)$$

where kinetic energy operators can be represented as

$$\hat{T}_i = \frac{1}{2m_e} \left(-i\hbar \frac{\partial}{\partial x_i} + eA_i \right)^2. \quad (3.10)$$

The vector potential is chosen in the Coulomb gauge $\mathbf{A} = (-y, x, 0)B/2$, while the magnetic flux is calculated for the average ring radius $(R_{in} + R_{out})/2$, and expressed in units of the flux quantum $\phi_0 = h/|e|$. Magnetic field of $B = 0.18 \text{ T}$ corresponds to a flux value of $\phi = \phi_0/2$.

Transmission and reflection coefficients are calculated by integrating the probability current that passes through a certain point x_R (x_L) in the output (input) lead after a sufficiently long period of time τ .

$$T = \int_0^\tau dt \int_{-\infty}^\infty dy j_x(x_R, y), \quad (3.11)$$

$$R = \int_0^\tau dt \int_{-\infty}^\infty dy j_x(x_L, y), \quad (3.12)$$

where the probability current is given by

$$j_x(x, y, t) = -i \frac{\hbar}{2m_e} \left(\Psi^* \frac{\partial}{\partial x} \Psi - \Psi \frac{\partial}{\partial x} \Psi^* \right) + \frac{e}{m_e} A_x \Psi^* \Psi. \quad (3.13)$$

Error of this method depends on the length of the time interval τ . For all results presented in this chapter, the wave packet is propagated until the sum $T + R$ reaches a value of at least 99%. The probability current is integrated at points $x_L = -1680 \text{ \AA}$, and $x_R = 1680 \text{ \AA}$.

As the packet reaches the lead boundaries, it gets scattered backwards. This backscattering prevents the calculation of T and R , since it affects the current density at points where T and R are calculated. This effect can be neglected, if the input and output leads are sufficiently long, so that the backscattering does not occur before most of the packet has already left the ring. Another approach, the one we consider here, is to use an imaginary potential near the boundary. This imaginary potential will decrease the value of the wave function as wave packet moves closer to a boundary, and completely suppress any reflection back into the ring. We model this imaginary potential (following [40], and [42]) as

$$V_{im}^R(\bar{x}) = -i E_{\min} \left[a\bar{x} - b\bar{x}^3 + \frac{4}{(c - \bar{x})^2} - \frac{4}{(c + \bar{x})^2} \right]. \quad (3.14)$$

Where

$$E_{\min} = \frac{\hbar^2 k_{\min}^2}{2m_e} = \frac{\hbar^2}{2m_e} \left[\frac{c}{2(x_2 - x_1)\delta} \right]^2 \quad (3.15)$$

is the minimum energy at which the absorption starts. Imaginary potential is expressed as a function of a dimensionless $\bar{x} = 2k_{\min}(x - x_1)\delta$, with x_1 and x_2 marking the beginning and the end point of the absorption region. Coefficients a and b are $a = 1 - 16/c^3$, and $b = (1 - 17/c^2)/c^3$, where $c = 2.62206$. Parameter δ is set to $\delta = 0.2$, and $x_2 - x_1 = 420 \text{ \AA}$, where x_2 is placed at the boundary of the computational box ($x_2 = 2100 \text{ \AA}$). Minimum energy for previously defined parameters is $E_{\min} \approx 25 \text{ meV}$. Similarly to V_{im}^R placed after x_R , we can construct V_{im}^L placed before x_L by applying $x \rightarrow -x$ in all expressions defining V_{im}^R .

Following Ref. [23], the perturbing SGM potential is taken as a Lorentzian function

$$V(x, y) = V_t \frac{w_t^2}{w_t^2 + (x - x_t)^2 + (y - y_t)^2}, \quad (3.16)$$

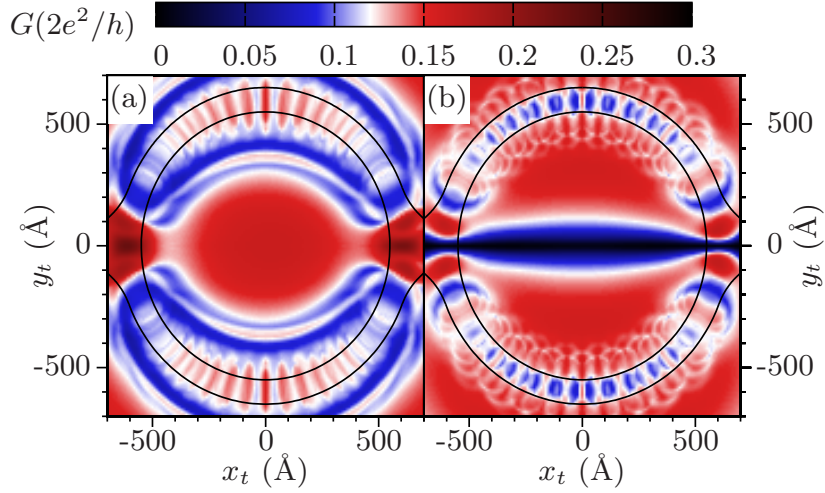


Figure 3.3: Conductance map for the wave packet with energy $\epsilon_1 = 115.4$ meV, situated in the first subband, for (a) $\phi = 0$ and (b) $\phi = \phi_0/2$. Tip potential width is $w_t = 140$ Å, and $V_t = 70$ meV.

with $w_t = 140$ Å and $V_t = 70$ meV, unless stated otherwise. The total conductance is then calculated using the Landauer formula

$$G(x_t, y_t) = \frac{2e^2}{h} \sum_n T_n(x_t, y_t), \quad (3.17)$$

where n runs over the occupied subbands. Coefficients T_n are calculated by putting the wave packet in a given subband n (at the initial time moment), and integrating the probability current as explained by Eq. (3.11).

3.3 Single band transport

Conductance maps obtained with the method described above, for two magnetic flux values (0 and $\phi_0/2$) are presented in Fig. 3.3. The scan is performed only over the area close to the ring, in order to prevent the wave packet scattering from the tip potential at the initial time moment. The wave packet energy is $\epsilon_1 = 115.4$ meV, and it is situated in the first subband. The figure shows similarities between the two cases, but also differences originating from the introduction of the magnetic field and the Aharonov-Bohm phase. We will focus our attention to Fig. 3.3(a), and discuss the magnetic field influence later.

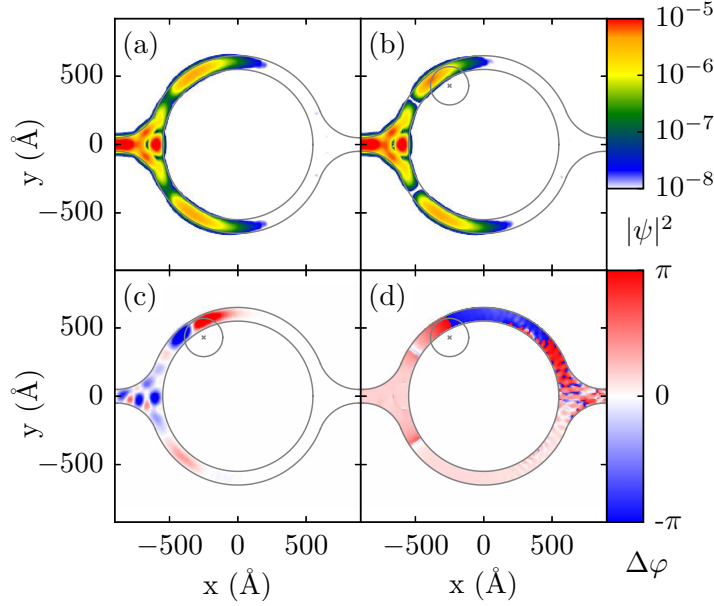


Figure 3.4: Snapshot of the wave packet propagation at $t = 130$ fs. Wave packet energy is $\epsilon_1 = 115.4$ meV and $\phi = 0$. (a) $|\psi|^2$ for a system without the tip. (b) $|\psi|^2$ for AFM tip with $V_t = 70$ meV, and width $w_t = 140$ Å, placed at $x_t = -250$ Å, $y_t = 430$ Å as shown by the cross in the figure (Although the tip is not present in (a), we mark its position from (b) in (a) for better comparison). The radius of a small circle is equal to a Lorentzian half-width at half-maximum (HWHM) and it is $w_t = 140$ Å. (c) Difference between probability distributions from (b) and (a). (d) Difference in the wave function phase between (b) and (a).

In the absence of magnetic field, the system is fully symmetric with respect to mirror reflection over the $y = 0$ axis, and this property is completely preserved in the overall conductance map. There are concentric fringes of oscillating conductance outside of the ring, and radial ones inside the channel. The first are associated with the phase change and the equiphase lines, while the second are caused by an interference of backscattered parts of the wave packet, as it will be explained in the following subsection.

3.3.1 Radial fringes

Tip potential can influence the wave packet in two different ways: by changing its phase and/or amplitude in every point. The amount of phase and amplitude change depends mostly on the strength of the tip potential at

that particular point. Tip positioned far away from the ring will act more uniformly across the whole channel, and it will affect mostly the phase. On the other hand, tip placed right above the channel (depending on its strength) could affect the amplitude and cause backscattering. This is illustrated in Fig. 3.4, where we present the wave packet at $t = 130$ fs for two cases: no tip (a), and tip positioned at $(-250, 430)$ Å (b). In order to separate the influence of the tip on the phase and the amplitude, we plotted the differences in probability density and the wave function phase between these two cases in Figs. 3.4(c) and 3.4(d), respectively.

When tip is positioned at the ring center ($x_t = 0, y_t = 0$), it hardly causes any backscattering. As it approaches one of the ring arms, it starts to deform the part of the wave packet that travels through that arm. This is clearly seen in Fig. 3.4(c), where one part of the wave packet is slowed by the tip. At later times, the packet still manages to go through the potential obstacle. If the tip potential is larger than the particle kinetic energy, and the tip is positioned at the channel center, the packet will not be able to go through the obstacle and it will undergo backscattering. Interference of these backscattered waves will create patterns of oscillating conductance seen in Fig. 3.3(a).

To get the basic understanding of the evolution of amplitude differences as the packet propagates, in Fig. 3.5 we compare time snapshots for two cases: no SGM tip, and SGM tip present. The tip creates a disbalance between the two arms, which can be seen in different interference patterns at the output ring-lead connection (compare 1st and 2nd column in Fig. 3.5 for times greater than 50 fs).

For conductance oscillations inside the ring arms, caused by the backscattering, positions of conductance maxima and minima can be predicted by using the model of a 1D quantum ring (with radius $R_m = (R_{in} + R_{out})/2$), and an infinite potential obstacle placed at one of its arms at distance $l = \alpha R_m$ from the input lead. Electrons can backscatter from the front or the back side of this obstacle, once or several times, or they can avoid it by traveling in the opposite arm. A scheme of the first three electron paths is shown in Fig. 3.6. If we ascribe certain amplitude $t_i e^{-i\beta_i}$ to each of these possible paths, and we approximate the transmission coefficient $T = |\sum_i t_i e^{-i\beta_i}|^2$ by using just the first three paths, one where electron avoids the obstacle ($i = 1$), and the two other where it backscatters only once from the front ($i = 2$) and the back side of the potential ($i = 3$), we get three main transmission contributions in the form $2t_i t_j \cos(\beta_i - \beta_j)$. When there is no magnetic field, the phase

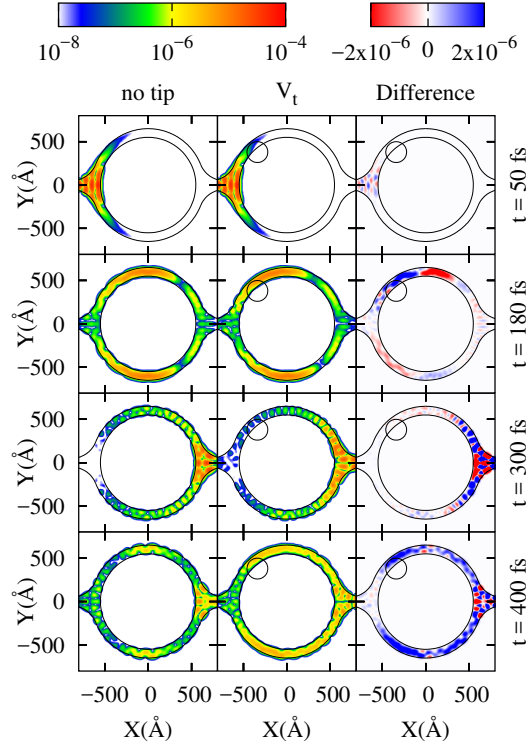


Figure 3.5: Snapshots of the wave packet propagation at different times for no tip present (first column on the left), and with the tip (middle column). The third column shows differences between the first two columns. Tip potential in this case is modeled as a sum of two Lorentzian functions, one with width $w_1 = 120 \text{ \AA}$ and height $V_1 = 140 \text{ meV}$, and the other with width $w_2 = 50 \text{ \AA}$, and height $V_2 = -70 \text{ meV}$. Wave packet energy is 140 meV .

difference $\Delta\beta_{ij} = \beta_i - \beta_j$ depends only on the difference in length between paths i and j . For paths 1 and 2 we mark this difference as $2l$ (see Fig. 3.6). For paths 1–3 we mark it as $2l'$, where $2l' = 2(\pi R_m - l)$, and for 2–3 this difference is $2(l - l')$. Each time this difference in length is equal to a multiple of a wavelength $n\lambda$ we will have a maximum, therefore conductance maxima are spaced across the ring circumference by $\lambda/2$ for the 1–2 and 1–3 interferences, and by $\lambda/4$ for the 2–3 interference. First maximum for the 1–2 interference is located near the input lead-ring junction, while for the 1–3 interference, it is on the output lead-ring junction. First maximum for the interference between paths where electron backscatters only once is located halfway between the input and the output lead. The wavelength in this case is obtained from the average wave vector of our wave packet, and is equal to

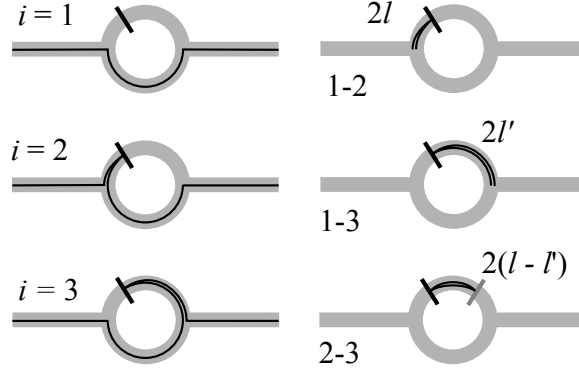


Figure 3.6: Electron paths: Figures on the left side show first three possible paths ($i = 1, 2, 3$) an electron can take inside the ring. Differences in length between these paths are shown on the right side.

$\lambda = 243 \text{ \AA}$. Because of the smooth lead-ring connections used in the simulation, predictions for the interference maxima based on the 1D model are not accurate in these regions (the lead-ring connection points). Figure 3.3(a) still shows first three maximums in the input and output lead-ring connections, originating from the 1–2 and 1–3 interferences. Maximums produced by the 2–3 interference are clearly visible in the ring arms, half way between the input and the output lead.

Compared with the experimental results in Ref. [31], conductance map in Fig. 3.3(a) shows more periodic radial oscillations along the ring arms. There are several possible reasons for this difference. The geometry of the system studied here has a reflection symmetry in both x and y direction, and the tip potential function is chosen to be the same in every point. Real, experimental systems are not fully symmetric due to the existence of charged impurities or rough edges. Electron scattering from the impurities alone, or double scattering from the tip and the impurities will in general modify the oscillation patterns seen in Fig. 3.3. Although it is hard to determine the tip potential profile in real experiments, our results suggest that the ratio between the width of the tip potential and the width of the ring's arm is very important. The tip potential used here is wide enough that it covers the whole ring arm in the radial direction, and completely blocks the passage of electrons. When the ring arm is wider than the tip potential, this blockade (and thus the backscattering) is only partial. There will be new paths, where electron scatters from the tip, but still progress forward through the ring.

Including these new paths will modify the oscillation patterns inside the ring.

Another aspect to be considered is the relationship between the width of the ring's arm and the electron wavelength. In our simulation, the packet wavelength (obtained from the average value of k_x) is 243 Å or 130 Å, which is comparable to the width of the ring's arm. In the case when electron wavelength is much smaller than the ring's arm, the situation is more complex, since the electron can backscatter within the ring's arm. This situation is investigated in Ref. [21], where it is shown that radial fringes in this case can originate from these internal electron reflections.

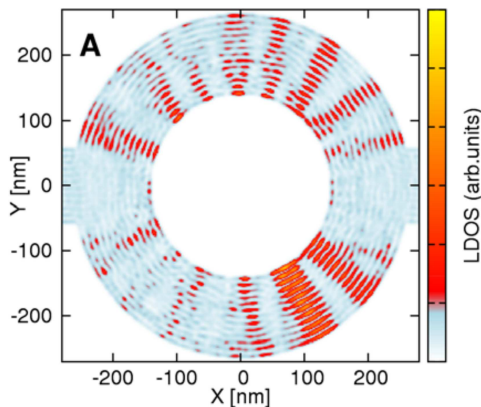


Figure 3.7: Local density of states at $E_F = 95.9$ meV (the ring's arm width is 125 nm). Figure taken from Ref. [21].

3.3.2 Concentric fringes

As noted in the experiments on QRs, concentric oscillations of the conductance outside of the ring are related to electron phase. Tip potential slows the wave packet, leaving a trail of modified phase behind it, as it can be seen in Fig. 3.4(d). The value $\Delta\varphi$ plotted in 3.4(d) is defined as a relative difference in wave function phase, when the tip is present and when there is no tip

$$\Delta\varphi(x, y, t, V_t) = \varphi(x, y, t, V_t) - \varphi(x, y, t, V_t = 0). \quad (3.18)$$

Red and blue stripes in the upper arm in Fig. 3.4(d) are fully saturated, meaning that the phase difference is very close to π . On the other hand, in the lower arm, the phase is changed by a value far less than π . Since the

wave packet energy is a distribution, rather than a single value, this phase difference $\Delta\varphi$ varies in time as the packet moves through the ring. In order to quantitatively describe the phase difference that the tip introduces between the two arms, we average the spatial phase difference from Fig. 3.4(d) in two areas: the upper-right part of the ring (area S_u : $x > 0$, $y > 0$), and the lower-right part of the ring (area S_d : $x > 0$, $y < 0$).

$$\langle |\Delta\varphi(t)| \rangle_{S_u} = \frac{1}{A(S_u)} \iint_{S_u} |\Delta\varphi(x, y, t)| dx dy \quad (3.19)$$

then represents the total phase difference in the upper arm at the time moment t , while $\langle |\Delta\varphi(t)| \rangle_{S_d}$ represents the phase difference for the lower arm. $A(S_u)$ is the surface area of S_u . Difference between these two

$$\Delta\varphi_{ud}(t) = \langle |\Delta\varphi(t)| \rangle_{S_u} - \langle |\Delta\varphi(t)| \rangle_{S_d}, \quad (3.20)$$

gives the average phase difference that the tip introduces between the arms at the time moment t . In Fig. 3.8(a) we show how this difference changes with time, as we move the tip in the radial direction along the y -axis ($x_t = 0$). For comparison, Fig. 3.8(b) gives the conductance profile as a function of the tip position.

In order to better explain the features of Fig. 3.8(a), we divide the propagation time into three different intervals. In the first interval (I), most of the wave packet is in the left part of the system ($x < 0$), and has not reached the area where $\Delta\varphi_{ud}(t)$ is calculated. In this region, $\Delta\varphi_{ud}$ increases as tip approaches one of the ring arms. Note that the value of $\Delta\varphi_{ud}$ in this time interval is not reflected in the final conductance in Fig. 3.8(b). Region A_2 of a very high phase difference does not cause a decrease in the conductance in Fig. 3.8(b). This is because most of the wave packet is still in the input, left part of the system.

In the second interval II, the wave packet enters the area where we calculate $\Delta\varphi_{ud}$, and this is followed by a decrease of $\Delta\varphi_{ud}$. In the area above A_1 ($y_t > 500 \text{ \AA}$) the phase does not recover, because of the tip backscattering. In the third time interval (III) $\Delta\varphi_{ud}$ decreases again. The reason is the mixing of the parts of the wave packet coming from the two arms at the output lead-ring junction. Part of the wave packet that traveled in the lower arm starts to enter the upper arm, and part from the upper arm enters the lower arm. This mixing changes the value of $\Delta\varphi_{ud}$, making it less useful in telling the phase difference between the arms. We mark the time moment when this mixing starts to considerably affect $\Delta\varphi_{ud}$ as the beginning of the third time

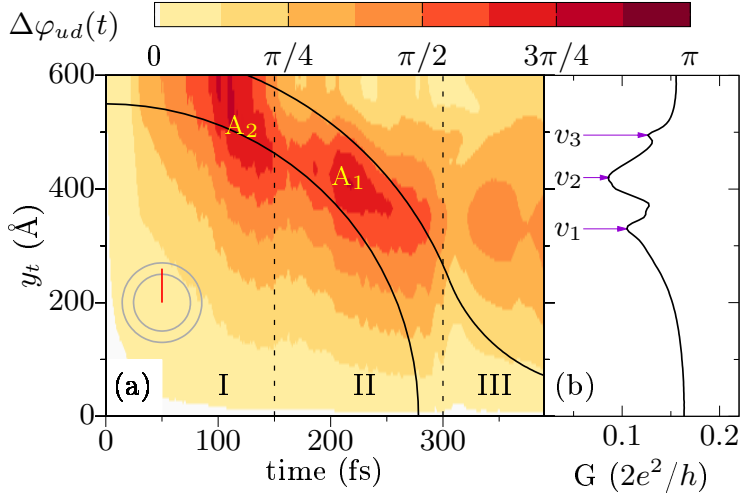


Figure 3.8: (a) Averaged phase difference as defined by Eq. (3.20) for the tip with $V_t = 70$ meV and $w_t = 140$ Å, positioned along the y axis ($x_t = 0$). Tip trajectory is marked with the red line in the small ring scheme (two gray circles). For better orientation, we also superimposed ring geometry in relation to the y axis (black curves). (b) Conductance for a tip scan in the radial direction $(0, y_t)$. Wave packet energy is $\epsilon_1 = 115.4$ meV, and magnetic field is set to zero.

interval III. In this interval, there is no obvious connection between $\Delta\varphi_{ud}$ and the ring conductance.

After time evolution, and we turn to the effects produced by the tip movement. For $y_t = 0$ (and $x_t = 0$) the system is fully symmetric with respect to mirror reflection over the x -axis, and the tip affects both arms equally. The phase difference between the ring arms is then zero, as shown in Fig. 3.8(a). As the tip moves along the radial direction, it starts affecting the packet phase in one arm more than that in the other arm. The increase in phase difference $\Delta\varphi_{ud}$ with y_t (in the region below v_1 in the second time interval in Fig. 3.8(a)) is followed by a decrease in G in Fig. 3.8(b). Also, for the largest phase difference (the region A_1 in Fig. 3.8(a)) the conductance experiences the largest suppression (the valley around v_2 in Fig. 3.8(b)). This valley corresponds to concentric, low conductance fringe in Fig. 3.3(a). As the tip moves closer to the upper arm, it causes the backscattering as explained previously, and the conductance increase above the v_3 comes from this backscattering. The only feature in Fig. 3.8(b) without a clear connection with $\Delta\varphi_{ud}$ is the peak between v_1 and v_2 . As said before, due to the mixing of

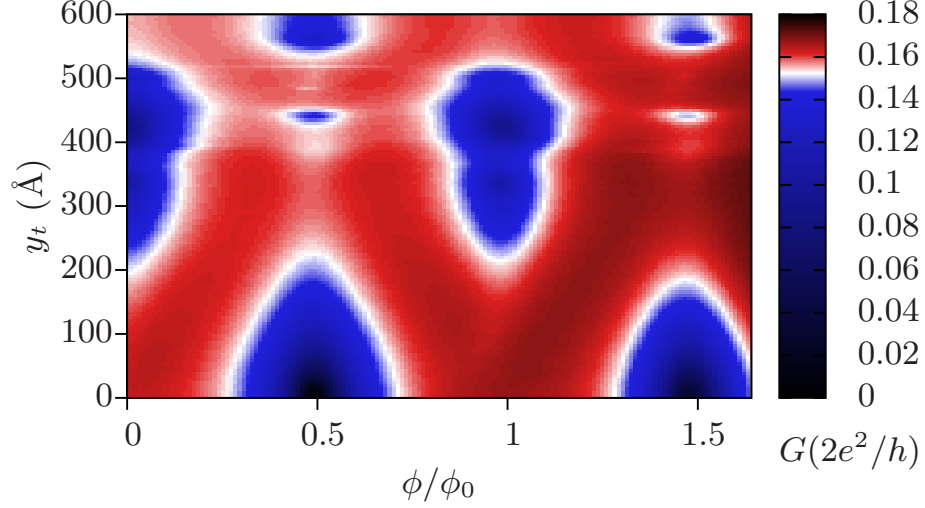


Figure 3.9: Conductance oscillations with magnetic flux for the AFM tip scan along the y axis ($x_t = 0$). All parameters are the same as in Fig. 3.8.

different parts of the wave packet, $\Delta\varphi_{ud}$ describes phase difference accurately only in short time interval.

3.3.3 Magnetic field dependence

Applying a perpendicular magnetic field in the absence of the tip will cause known AB oscillations in the conductance. Parts of the wave packet travelling in the opposite arms will acquire different phase, and interfere constructively or destructively depending on the field strength. The tip potential will change the packet phase (as shown in Fig. 3.4(d)), and create a phase difference between the parts travelling in the two arms (as shown in Fig. 3.8(a)). This phase will then modify the AB oscillation pattern. This is shown in Fig. 3.9, where we compare the conductance change with the magnetic flux and the radial tip movement. As the tip approaches the ring and creates the phase difference, ϕ_0 periodic AB oscillations continuously turn into $\phi_0/2$ periodic Altshuler-Aronov-Spivak [43, 2] (AAS) oscillations. AB oscillation minima disappear because phase difference created by the tip compensates the one created by the $\phi_0/2$ magnetic flux. AAS oscillations are more resistant to the tip potential, because they are produced by the interference of parts of the wave packet that traveled across the whole ring circumference, and therefore

gained equal phase. Since the phase difference created by the tip never exceeds π , these AAS oscillations do not fully turn into a $\phi_0/2$ translated initial AB pattern. Because the phase difference decreases, they start to change back to the initial AB oscillation pattern. This suppression of AB oscillations and occurrence of $\phi_0/2$ oscillation pattern was shown in previous works on quantum rings [40, 44], where impurity potentials inside the ring were used to create a phase difference between the ring arms. Here we show that such an impurity is not needed, and that the tip potential can already lead to shortening of the AB oscillation period.

This modification of the AB oscillation pattern is characterised by the occurrence of “V” shaped regions in Fig. 3.9. As the AFM tip approaches the arm, AB maxima split in two parts and each part starts to move toward the initial AB minimum. When phase difference created by the tip is equal to π these two parts, originating from two different maxima, should combine and create a new maximum. At this point, the initial AB oscillation pattern is completely inverted. V shaped regions shown in Fig. 3.9 are somewhat similar to conductance patterns observed in the real experiments. In Fig. 3.10 we present experimental data showing conductance change in the radial direction versus the magnetic flux (the figure is taken from [31]). By similarity here we mean that initially ϕ_0 periodic oscillation pattern for $y_t = 0$ in Fig. 3.9, and $d = 0.5 \mu\text{m}$ in the left inset of Fig. 3.10, turns into $\phi_0/2$ periodic oscillation pattern for $y_t \sim 200 \text{ \AA}$ and $d \sim 0.4 \mu\text{m}$ in the respective figures (we additionally marked this pattern in Fig. 3.10 with two black lines).

The conductance pattern inside the ring is created by interference of backscattered parts of the wave packet, and although the magnetic field changes the amplitude of these oscillations, positions of all maxima and minima remain unchanged, as shown in Fig. 3.3(b). This can be explained by the fact that electron does not gain any AB phase when moving back and forth along the same path, as in the case of backscattering. Differences between Figs. 3.3(a) and 3.3(b) show which G -map features can be related with the change in the electron phase, and similarities show features which are phase independent.

3.4 Multiband transport

In real systems, the total conductance is a sum of contributions coming from electrons moving in several subbands. We populate the second subband in

3.4. Multiband transport

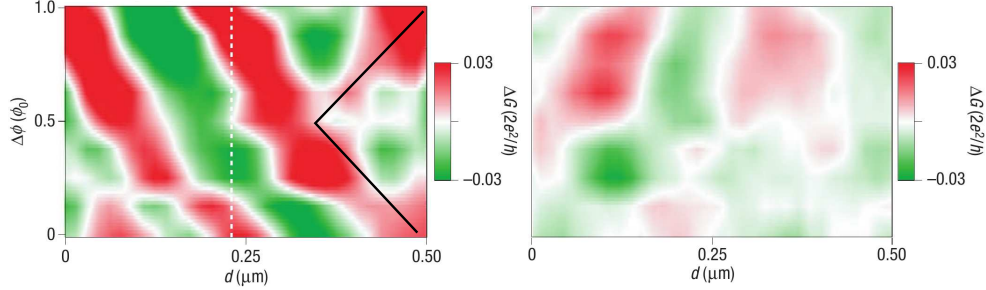


Figure 3.10: Conductance change ΔG as a function of magnetic flux through the ring versus the radial distance d from the ring. Figure is taken from [31]. Notice that instead of a single radial line, these conductances were obtained by averaging results in narrow rectangles. Graph on the left is obtained by averaging radial conductances on the left side of the ring (the ring is shown in Fig. 3.1(b)), while graph on the right is obtained by averaging radial conductance on the right side of the ring. In both cases d is used to measure radial distance, but it is relative to the averaging rectangle, and not to the ring center. We mark with two black lines in the left figure the V-shaped region similar to that obtained in our Fig. 3.9.

our system by raising the total wave packet energy to $\epsilon_2 = 270$ meV. This energy is set so that the kinetic energy for an electron in the second subband is equal to the kinetic energy for an electron in the first subband (studied previously). This allows us to analyze the influence of confinement along the y , since the transverse wave function is symmetric for the first subband, and asymmetric for the second subband.

Conductance maps for an electron in the first subband, and the second subband are presented in Figs. 3.11(a) and 3.11(b), respectively. In Fig. 3.11(c) we show the sum of these two. For a particle in the first subband, there is a drastic difference when compared with the results from the previous section. Tip parameters are the same, therefore all the differences come from an increase in the particle kinetic energy. The wave packet wavelength is ~ 130 Å, and the radial fringes inside the ring are smeared out.

For the second subband, the results are similar to the ones presented in the previous section. Positions of the radial fringes inside the ring match those for a particle in the first subband (from the previous section), since their kinetic energy along the x is equal. Conductance map outside of the ring shows the

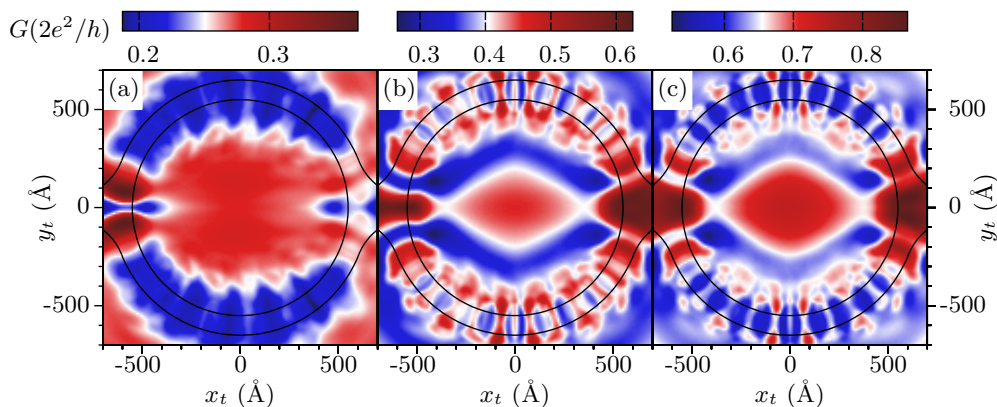


Figure 3.11: Multiband transport: Conductance map for the wave packet with energy $\epsilon_2 = 270$ meV situated in the first subband (a), and the second subband (b). (c) Conductance map obtained by summing (a) and (b). Magnetic field is set to zero, the tip potential is $V_t = 70$ meV, and the potential width is $w_t = 140$ Å.

effects of the wave function symmetry along the y direction. Regions of a low conductance for a symmetric packet (presented in the previous section) turn into regions of a high conductance for the asymmetric packet.

Summing the conductance maps for the first and the second subband, we obtain the total conductance map as presented in Fig. 3.11(c). Contributions from the second subband are clearly visible in the total conductance map. This is because the amplitude of the conductance oscillations is larger for a particle in the second subband than that for a particle in the first subband, as a consequence of lower ϵ_k^n/V_t ratio and therefore more backscattering (ϵ_k^n is the kinetic energy of a particle traveling in the n -th subband). These results suggest that, in case of a multiband transport, the tip might be more selective to higher modes, which lack the kinetic energy in the direction of propagation. These modes will backscatter from the tip and create the interference patterns, while the lower modes (with the kinetic energy several times larger than the tip potential) will manage to go through the tip potential and contribute to the total conductance.

To test this further, we perform a tip scan along the average ring circumference (in the upper part of the system, $y_t > 0$) and continuously increase the tip potential. We calculate the average deviation of the conductance for each subband separately

3.4. Multiband transport

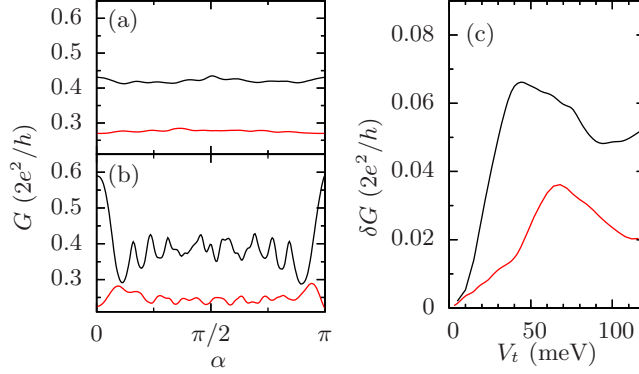


Figure 3.12: Conductance profile along the average ring circumference $\alpha(R_{in} + R_{out})/2$ in the upper part of the system ($y_t > 0$) for $V_t = 10$ meV (a), and $V_t = 40$ meV (b). Red (black) line shows results for the first (second) subband. α is the angle between the tip position vector (x_t, y_t) and the $-x$ axis. Wave packet energy is $\epsilon_2 = 270$ meV. (c) Average conductance deviation calculated along the average ring circumference as a function of the tip strength. Magnetic field is set to zero.

$$\delta G_n = \sqrt{\langle G_n^2 \rangle - \langle G_n \rangle^2} \quad n = 1, 2, \quad (3.21)$$

where

$$\langle G_n \rangle = \frac{1}{\pi} \int_0^\pi G_n(\alpha) d\alpha, \quad (3.22)$$

and

$$\langle G_n^2 \rangle = \frac{1}{\pi} \int_0^\pi (G_n(\alpha))^2 d\alpha. \quad (3.23)$$

Here, α is the angle between the tip position vector and the $-x$ axis, and $G_n(\alpha)$ is the conductance in the n -th subband when the tip is placed at $(-R_m \cos \alpha, R_m \sin \alpha)$. Results are presented in Fig. 3.12. For a weak tip potential, there is no backscattering and the conductance profile in Fig. 3.12(a) shows weak G oscillations. As the tip potential rises so does the backscattering, and the interference pattern becomes visible. The amplitude of these oscillations is a linear function of the tip potential strength, with linear coefficient being inversely proportional to the particle kinetic energy in the direction of propagation ϵ_k^n . When the tip potential exceeds ϵ_k^n this curve saturates, because most of the wave packet has already backscattered from the tip. These results are in agreement with experiments on QRs [32], where

measurements show similar conductance behavior with the tip potential (see Fig. 2(d) in Ref. [32]). Conductance profile along the average ring circumference in Fig. 3.12(b) shows that for a stronger tip there is a mixing of different interference patterns discussed previously, as with larger tip potential they extend further through the ring. As a result of this mixing, the average distance between the interference maxima and minima is not constant along the conductance profile. The value of δG_n shows how visible will the subband n be in the total conductance map. Higher subbands reach saturation quickly and they become clearly visible even for weak tip potentials, while lower subbands saturate for very high tip potentials, exceeding their kinetic energy.

A recent work by T. Chwiej and B. Szafran [41] also focuses on multiband transport in QRs, in the case when many subbands are occupied. They solved the Schrödinger and Poisson equation self-consistently, and investigated the scattering problem. This allowed them to calculate the linear conductance. Using this method, conductance maps for as much as eight subbands in the channel were calculated. Although this is very different from the two subband case considered here, results turned out to be remarkably similar. One of the possible explanations of this similarity lies in previously noted tip selectivity to higher subbands. If lower subbands do not contribute to conductance oscillations in the final conductance map, then simulating electron transport with the weak tip potential and several subbands in the channel is equivalent to performing simulations with one or two subbands and a stronger tip.

Next, we compare previously calculated conductance maps with the electron probability density. Early experiments [32, 22] showed that the conductance maps probe the interference patterns in the electron density. This was done for a weak tip-induced potential. We obtain the electron density by numerically solving 2D Schrödinger equation in case with no external magnetic field. Leads are excluded from the calculation, and the electron motion is confined to the ring and the smooth lead-ring connections. Since the wave packet energy is given by a distribution of values, rather than a single value, we consider only those states with energy as close as possible to the average wave packet energy. Results for electrons with energies $\epsilon_1 = 116.39$ meV, and $\epsilon_2 = 270.35$ meV are presented in Fig. 3.13. Comparing $|\psi|^2$ with the previous conductance maps, we can conclude that (for a strongly interacting tip) there is no direct correspondence between the conductance oscillations inside the ring and the electron probability density. The conductance maps are richer in features than $|\psi|^2$. As we explained earlier, these features origi-

3.5. SGM of AB rings: Conclusions

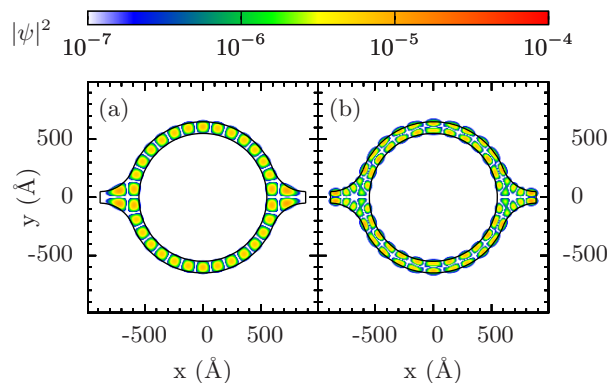


Figure 3.13: Electron probability density for energy levels $\epsilon_1 = 116.39$ meV (a), and $\epsilon_2 = 270.35$ meV. Magnetic field is set to zero.

nate from the tip acting as a scattering center for electrons moving in different subbands. In that sense, our results are closer to [45] where conductance maps of a Hall bar were calculated in the ballistic transport regime, but for classical electrons. Similar results were obtained for Hall bars in the diffusive regime [46]. Since we consider electrons as quantum particles, our results exhibit interference effects not present in the previous two works [45, 46].

3.5 SGM of AB rings: Conclusions

In this chapter, we investigated the position dependent conductance of a small quantum ring made from 2DEG. In case of a single subband transport, we showed that concentric conductance oscillations outside the ring are connected with the phase difference created by the AFM tip in the two ring arms. The radial conductance oscillations inside the ring originate from the interference of parts of the wave packet backscattered from the tip potential. The oscillations of the conductance inside the ring are not necessarily $\lambda_F/2$ periodic, since they are the sum of several interference patterns, each dominant in different parts of the ring. In regions where the ring is smoothly connected to the leads, the oscillations depend on the shape of the lead-ring connection. The relation between the wave function phase and the conductance pattern outside of the ring is shown explicitly, as was intuitively hinted in the first experiments on QRs [31]. As compared to the previous interpretation, where the conductance change at a particular point was connected with the electron probability density $|\psi|^2$, our approach is different, since we

considered the tip acting as a scattering center.

The tip-induced phase difference between the two arms will modify the Aharonov-Bohm interferences. This modification of AB oscillations is characterized by the occurrence of V shaped features, i.e. ϕ_0 periodic patterns in the conductance maps, very similar to the experimentally observed V patterns. We found a linear dependence between the amplitude of the conductance oscillations and the tip potential strength, for weak tip potentials. For stronger tip potentials (of the order of the electron kinetic energy) there is no longer a linear dependence. In case of the multiband transport, the coefficient of this dependence is different for different subbands, and depends on ϵ_k^n . These results suggest that the contribution of each subband in the final conductance map is not equal, and that the tip might be more selective to higher modes.

3.5. SGM of AB rings: Conclusions

CHAPTER 4

Fano resonances in the conductance of graphene nanoribbons with side-gates

4.1 Introduction

In the introductory chapter we already described the electronic structure of graphene.⁴⁷ Before we start investigating SGM in graphene, it is important to understand how this band structures changes when we cut graphene into ribbons, and what happens if we apply electrostatic gating*. Another question is what are the effects of different edge types introduced after cutting? Although large sheets of graphene have no band gap, measurements [48, 49] have shown that cutting them into narrow ribbons leads to the opening of a so called transport gap, a narrow region of suppressed conductance near the neutrality point (see Figs. 4.1(a) and 4.1(b)). The influence of side gates on electron transport in these systems was measured in Ref. [50], and it was found that the side gates shift the position of the gap in the back-gate voltage. Similar experiments were performed in wider Hall bars [51], where the effect of the side gates was explained in terms of two parallel conducting channels running along the edges and inside the Hall bar.

*Results presented in this chapter are based on our publication: M. D. Petrović, F. M. Peeters, *Fano resonances in the conductance of graphene nanoribbons with side gates*, Physical Review B **91**, 035444 (2015).

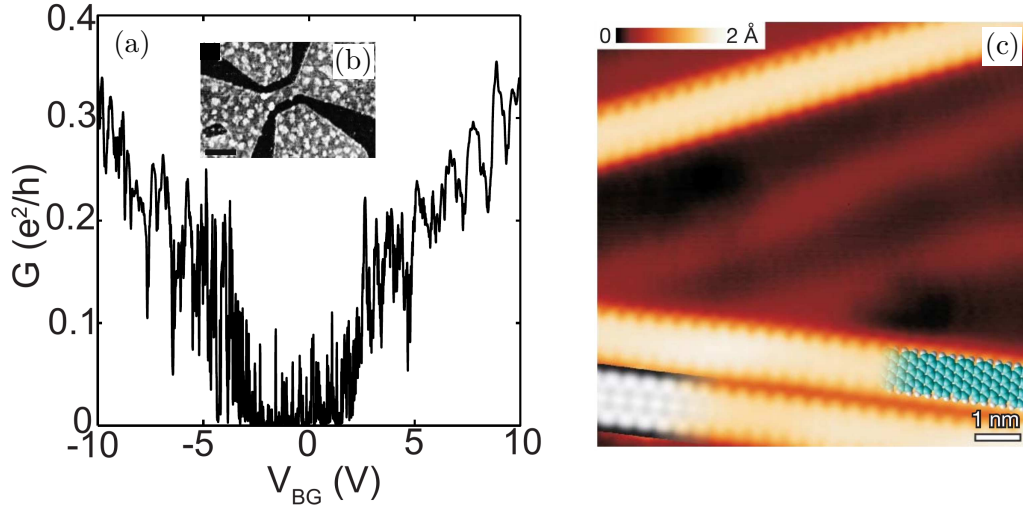


Figure 4.1: (a) Transport gap measured in narrow graphene nanoribbon shown in (b). Both figure are taken from Ref. [50]. (c) STM image of chemically produced GNRs with ideal armchair edges. Image taken from Ref. [52].

The understanding of nanoribbons is also important from another point of view. Graphene nanostructures are usually connected with metallic contacts through leads which can be modeled as semi-infinite nanoribbons, therefore understanding of nanoribbons is very important if we want to understand more complicated geometries.

In this chapter we analyze the electronic transport through a potential constriction in narrow graphene ribbons. The transport gap is usually considered to originate from localisation due to the edge disorder. Although all to date experiments utilize ribbons with some degree of disorder, whether on the edges or in the bulk, there is a possibility of creating atomically precise ribbons. In Ref. [52] production of ideal armchair ribbons was achieved using the bottom-up approach from precursor monomers (see Fig. 4.1(c)). Experiments like this suggest that pure side-gated ribbons could be experimentally obtainable in the future. Based on this, we restrict ourselves to ideal ribbons, and study the influence of a side potential on the electronic transport (However, at the end of this chapter, we will comment on the effects introduced by disorder in the form of carbon vacancies).

Previous theoretical research on bearded zigzag ribbons and ribbon junc-

tions [53, 54] found zero-conductance dips in the low energy region, near the neutrality point, and explained them as Fano resonances. Similar theoretical results were obtained for constrictions induced by electrical potentials in zigzag ribbons [55], where it was shown that the energy of those dips strongly depends on the impurity distribution inside the ribbon. Another work on potential constrictions [56] reported abnormal paths of electron current flowing along the high potential regions. In this chapter we will investigate what happens in the center of the constriction when several modes are present in the input lead. Four ribbons with different edge orientation (zigzag or armchair) and conducting properties are studied.

The studied ribbon system is described in the next section, where we briefly repeat our discussion on the graphene tight-binding model. First, we investigate the dispersion relations of graphene ribbons and their transmission functions. Next, we show what are the effects of the side-gate misalignment in zigzag ribbons. The conductance of these ribbons exhibits peaks for specific combinations of Fermi energy and side-side gate potential. We give a comparison between the conductance as a function of the Fermi energy and the side-gate potential $G(E_F, U_c)$ and the eigenenergies in a closed system $E_n(U_c)$. Peaks in the conductance closely follow the eigenlevels in a closed system. At the end of the chapter, we study the behaviour of current density and LDOS at the resonant energies.

4.2 System and Methods

The studied system is schematically shown in Fig. 4.2(a). It is a graphene nanoribbon (GNR) connected to two leads and exposed to a symmetric potential from the two side gates. We consider four different ribbon types, two with zigzag (Fig. 4.2(b)) and two with armchair (Fig. 4.2(c)) edges. The two ribbons with zigzag edges differ in width only by a single line of carbon atoms. We call the one with even number of carbon lines (n_y) the zigzag ribbon, while the one with odd n_y is called the anti-zigzag ribbon. The spatial distribution of the potential from a side gate (U_g) is chosen to be a Gaussian function, so the total potential is modeled by

$$U(x, y) = U_{g1}(x, y) + U_{g2}(x, y), \quad (4.1)$$

where

$$U_{g1(2)}(x, y) = U_c e^{-(x-x_{g1(2)})^2/(2\sigma_x)^2} e^{-(y-y_{g1(2)})^2/(2\sigma_y)^2}. \quad (4.2)$$

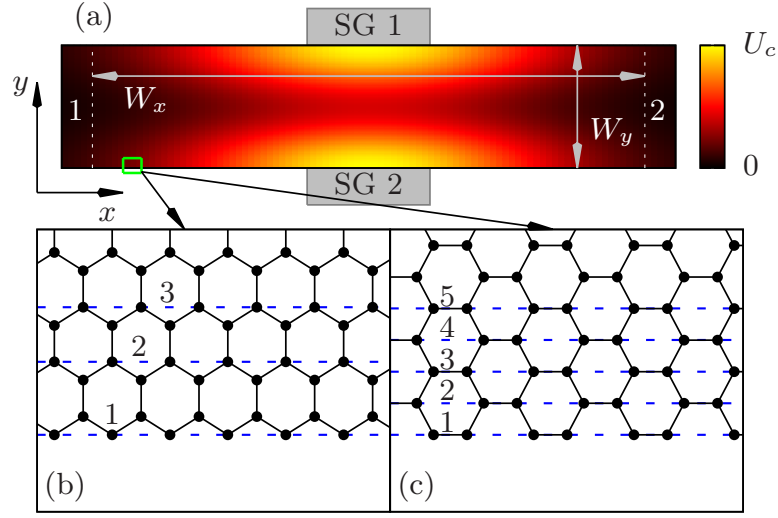


Figure 4.2: (a) Graphene nanoribbon system: colormap represents the change in the electron on-site energy caused by the two side gates SG1, and SG2. (b)–(c) Zoom of the nanoribbon showing the zigzag, and the armchair edge. Ribbon width (W_y) is defined by a number n_y of atom lines (horizontal dashed blue lines) in the y direction. Four ribbon types are considered: the zigzag ($n_y = 46$, $W_y = 9.66$ nm), the anti-zigzag ($n_y = 47$, $W_y = 9.87$ nm), the semiconducting armchair ($n_y = 82$, $W_y = 9.96$ nm), and the metallic armchair ($n_y = 80$, $W_y = 9.72$ nm). All of these have a length (W_x) of 45 nm.

Maxima y_{g1} , and y_{g2} are positioned on the upper, and lower edge of the ribbon, respectively. We took $\sigma_x = 6$ nm, and $\sigma_y = 2$ nm. A small misalignment between the side gates is described using a parameter $\Delta x = x_{g1} - x_{g2}$. Δx is used to modify the ratio of backward and forward intervalley scattering in ribbons with zigzag edges. Usually, just x_{g1} is changed, while x_{g2} is kept constant.

As described in the introduction, our results are obtained using KWANT.²⁷ KWANT uses the wave function approach to solve the scattering problem in a tight-binding system. Due to the Fisher-Lee relation the wave function approach is mathematically equivalent to non-equilibrium Green's functions formalism. The graphene tight-binding Hamiltonian is defined as

$$\hat{\mathbf{H}} = \sum_{\langle i,j \rangle} (t_{ij} \hat{c}_i^\dagger \hat{c}_j + h.c.) + \sum_i U_i \hat{c}_i^\dagger \hat{c}_i + \sum_{\langle i,k \rangle} (t'_{ik} \hat{c}_i^\dagger \hat{c}_k + h.c.), \quad (4.3)$$

where \hat{c}_i^\dagger and \hat{c}_i are the creation and annihilation operators for π electrons on the i -th carbon atom, U_i is the on-site potential, and t_{ij} and t'_{ik} are the hoppings between pairs of nearest $\langle i, j \rangle$ and next-nearest $\langle i, k \rangle$ neighbours. We implement this Hamiltonian by setting $t_{ij} = -2.7$ eV for all pairs of neighbouring carbon atoms, and $U_i = U(x_i, y_i)$, where (x_i, y_i) is the position of i -th carbon atom. Most of the following results are obtained without consideration of the next-nearest neighbour hopping ($t'_{ik} = 0$), but in later subsections, we test the effects of next-nearest neighbour hopping on our results.

4.3 Dispersion relation

To better understand the electron behaviour inside the leads, and in the constriction region, we calculate the dispersion relations for an infinitely long ribbon. The transverse potential across this ribbon is equal to the potential in across the constriction

$$U'(y) = U(x_{g1}, y), \quad (4.4)$$

with Δx set to zero. Results are presented in Fig. 4.3. For no side-gate potential (thick black lines), the dispersion describes states in the input and output lead, while for $U_c = 0.2$ eV (thick blue lines), it describes states inside the constriction region.

Results for the zigzag ribbon in Fig. 4.3(a) show the lowest conduction and the highest valence band consisting of the well known dispersionless edge states [57, 58] in the $(\frac{2\pi}{3a_0}, \frac{4\pi}{3a_0})$ range of k_x values. The side gate potential has the strongest influence in this part of the dispersion relation, moving these states in energy by U_c . It was shown previously [59], that applying two oppositely-biased side gates can open up an energy gap in a ribbon with zigzag edges. Here, the gates are equally biased and therefore there is no gap opening. This one-to-one connection between the gate potential and the band energy of the edge states depends on their spatial overlap. States at $k_x = \pi/a_0$ are completely localized on the edges, and for them this connection always holds. States outside of the $(\frac{2\pi}{3a_0}, \frac{4\pi}{3a_0})$ range extend across the whole ribbon, and they move in energy proportionally to U_c . This different influence on different parts of the dispersion relation causes a deformation of the lowest conduction band. With this deformation (encircled in Fig. 4.3(a)) the maximum energy of the highest valence band becomes larger than the minimal energy of the lowest conduction band. This band bending allows

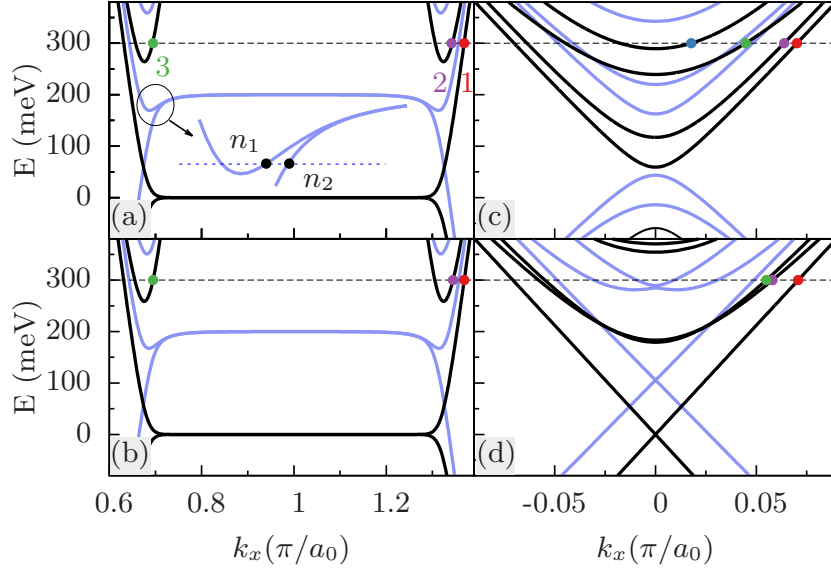


Figure 4.3: The dispersion relations for the considered four types of ribbons: the zigzag (a), the anti-zigzag (b), the semiconducting armchair (c), and the metallic armchair (d) ribbon. The thick black lines show bands for no side gate potential ($U_c = 0$), while the thick blue lines show bands for $U_c = 0.2$ eV. We mark the incoming modes at $E_F = 0.3$ eV with colored dots, and in (a) they are labeled by the decreasing value of their k_x vector. The encircled area in (a) is shown enlarged and it emphasizes the deformation of the first conduction band and the opening of new modes n_1 and n_2 .

modes from both bands to coexist in the constriction region (for a certain range of U_c and E_F values), as well as new modes to open up (see the zoomed area in Fig. 4.3(a)).

Results for the anti-zigzag ribbon (Fig. 4.3(b)) are almost identical to the previous, which is expected, since the two ribbons differ in width only by a single line of carbon atoms. In the semiconducting and metallic armchair ribbons all bands move in energy as a linear function of U_c . Beside this, there is a shift of the band minima in k_x for the metallic ribbon.

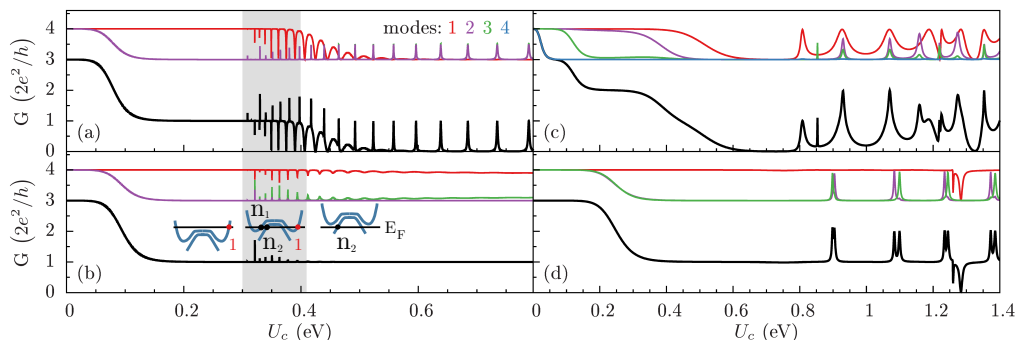


Figure 4.4: Conductance (thick black curves) as a function of the side gate potential at $E_F = 0.3$ eV for the zigzag (a), the anti-zigzag (b), the semiconducting armchair (c), and the metallic armchair (d) ribbon. Colored curves show the transmission probabilities of individual modes, and they are vertically displaced by $\Delta T = 3$ for clarity. The legend in (a) indicates which line color corresponds to which incoming mode (the modes are numbered in Fig. 4.3(a)). Gray areas in (a) and (b) mark U_c values for which modes from both conduction and valence bands coexist in the constriction region. This is illustrated schematically in insets of (b), which show the dispersion in the constriction for different side gate potentials. The band bending is exaggerated for better view.

4.4 Transmission of individual modes

We calculate the conductance of these ribbons using the Landauer formula

$$G(E) = \frac{2e^2}{h} T(E). \quad (4.5)$$

The transmission functions $T(E)$ are obtained using KWANT [27], directly as is implemented in the software package. The conductance of the four ribbons as a function of the side gate potential is presented in Fig. 4.4. Next to the total conductance, we separately plotted the transmission probability of each individual incoming mode. These probabilities are obtained by summation of the squared amplitudes in the transmission part of the scattering matrix related to a specific mode.

Results for the zigzag ribbon (Fig. 4.4(a)) exhibit an array of transmission and reflection peaks. They appear when U_c goes above the Fermi energy (0.3 eV), when states from the valence band open in the constriction region (see the insets in Fig. 4.4(b) for the dispersion in the constriction), and pn inter-

faces start to form near the edges. It is relevant to know that a pn interface near the edge can be a source of strong intervalley scattering [60], responsible for the valley valve effect [61]. All reflection peaks originate from the first incoming mode, while peaks in the transmission relate to electrons in the second and the third mode. These abrupt changes of the conductance appear whenever a combination of E and U_c matches one of the resonant states as described in Ref. [55], and demonstrated below. The zero-conductance resonances occur when U_c goes above the electron energy but, due to band deformation, the first incoming mode is still open in the constriction region (gray area in Fig. 4.4(a)). In this regime the electrons in the first mode are transmitted normally (not changing modes) unless they hit a resonant state in which case they undergo a backward intervalley scattering. Behaviour of electrons in the other two modes (2nd and 3rd) is different. They have identical transmissions, and the sum of conductance peaks coming from these two modes equals one conductance quantum, which could be explained if they both scatter into a single open n_2 mode in the constriction.

For the anti-zigzag ribbon (Fig. 4.4(b)), which exhibits forward intervalley scattering of electrons in the first mode [60], results significantly differ. The ribbon is conductive even for high side gate potentials, because electrons in the first mode are almost fully transmitted. Although the overall conductance does not show any resonant reflection peaks, peaks are visible in transmission of electrons in the first mode. The complementary reflection and transmission peaks coming from the first and the third mode suggest that these two now scatter into the available n_2 state in the constriction. On the other hand, electrons in the second mode show only small transmission peaks, and only when state n_1 is open.

The ratio of backward and forward intervalley scattering determines how modes reorganise in the constriction region, because incoming modes compete to populate a small number of states available in the constriction. When electrons in the first mode scatter backward, the electrons in the second mode are transmitted (Fig. 4.4(a)), and when electrons in the first mode scatter forward, the ones in the second mode are blocked (Fig. 4.4(b)).

At higher potentials, conductance peaks also appear in the armchair ribbons. In the semiconducting ribbon, all modes transmit at specific side potentials. In the metallic ribbon the electrons in the first mode are fully conducting, while peaks originate from the electrons in higher subbands. There are two possible explanations for these peaks. They occur every time a new mode opens in the constriction, or every time there is an eigenstate in

a closed system. Below we demonstrate that similarly to the zigzag ribbons, the latter is the case.

4.5 Mirror symmetry and intervalley scattering

Figure 4.5 shows colormaps of the conductance versus the Fermi energy and the side gate potential. In ribbons with zigzag edges the conductance plateaus are unaffected by the gate potential for negative energies, and in armchair ribbons they are weakly affected (not shown). For all four ribbons the results are asymmetric with respect to changing sign of U_c (not shown), i.e. $G(E, -U_c) = G(-E, U_c)$. Similar results were obtained in the experiments of Ref. [50] (see Fig. 4(b) in this reference).

In order to explain these data in terms of the number of occupied modes inside the constriction, we plotted the minimal (maximal) energies of the electron (hole) bands on top of the conductance colormap. These energies are obtained from the dispersion relations of infinite ribbons with transversal potential profile equal to the one in the center of the constriction.

In general, the conductance plateaus of all four ribbons follow the extreme energies of electron and hole bands, most of which behave as a linear function of U_c . Particularly interesting are the zigzag ribbons, where due to previously described band bending the maximal energy of the highest hole band goes above the minimal energy of the lowest electron band. In this specific regime (area in Fig. 4.5(a) bounded by the highest green and the lowest blue line and marked with I) states from both bands coexist in the constriction region, and also a new state (n_1) opens up. This is the area where most of the peaks appear. The main difference between the zigzag (Fig. 4.5(a)) and the anti-zigzag (Fig. 4.5(b)) ribbon is seen in the area below the lowest blue line (regions II and III), when no open electron states exist in the constriction. In area III in the zigzag ribbon the electron transport is completely blocked, since there is only one incoming mode in the input lead, while in area II (when the second and the third mode open in the input lead) positive conductance peaks appear. This is consistent with previous results in Fig. 4.4(a) where the positive conductance peaks originated from the second and the third mode. The anti-zigzag ribbon is completely conducting in this region (II and III), due to the forward intervalley scattering.

The main difference between the zigzag and the anti-zigzag case origi-

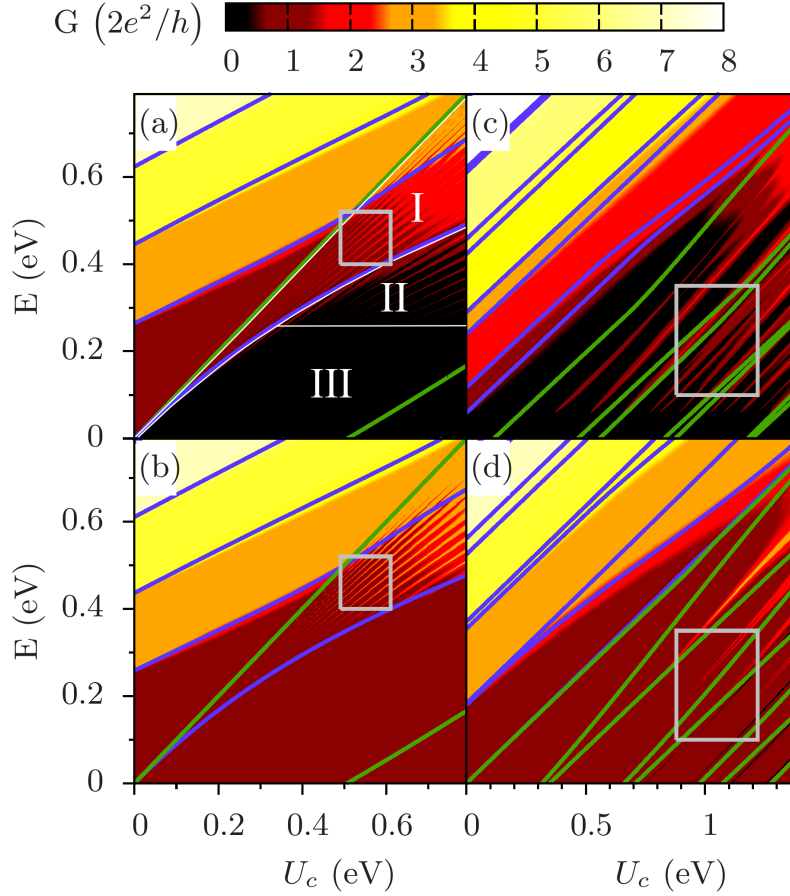


Figure 4.5: The conductance as a function of the Fermi energy and the side gate potential U_c for zigzag (a), anti-zigzag (b), semiconducting armchair (c), and metallic armchair (d) ribbon. The blue (green) lines mark the minimal (maximal) energies of the electron (hole) bands. The white boxes highlight the areas with resonance peaks where a comparison with the eigenstates is made.

nate from the valley-valve effect [61]. In Ref. [62], the valley-valve effect was interpreted in terms of the honeycomb topology and crystal structure symmetry. The perfect electron reflection in zigzag ribbons with pn junction was explained using the parity of the wave function under the mirror reflections with respect to the central line of the ribbon. This study treated a special case of a potential step, where the potential across the ribbon (the y direction) is constant. On the other hand, the potential in our system

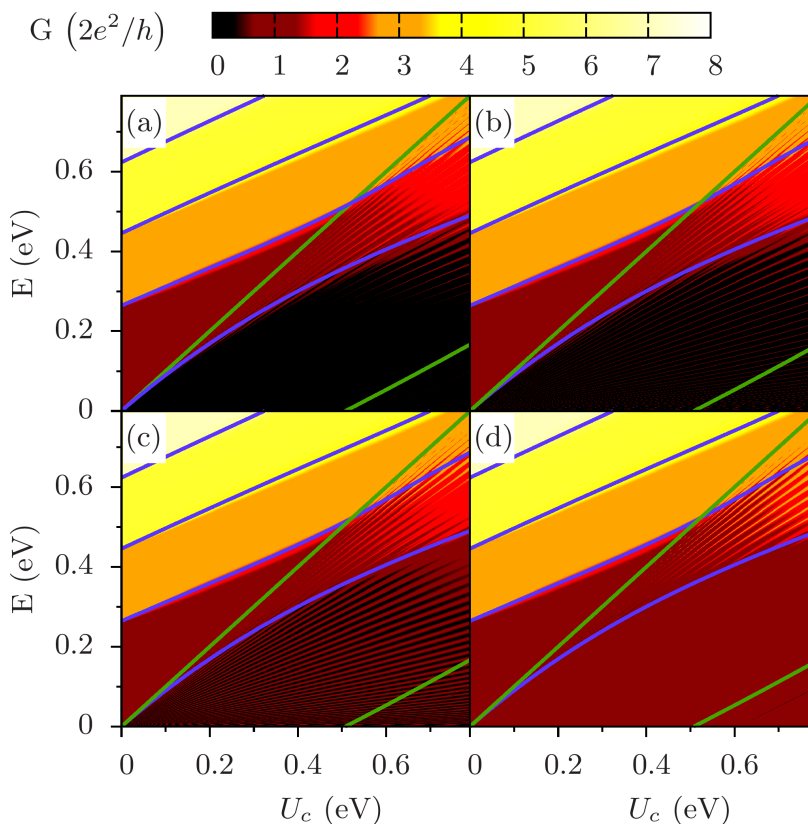


Figure 4.6: Conductance of the zigzag ribbon ($n_y = 46$) for different misalignments between the side gates: (a) $\Delta x = 0$, (b) $\Delta x = l_c/2$, (c) $\Delta x = l_c$ and (d) $\Delta x = 3l_c/2$, where l_c is the graphene lattice constant.

is not constant, but possesses a mirror symmetry with respect to the central line of the ribbon. Since we still observe the valley-valve effect, we predict that the results of Ref. [62] could probably be extended to a case of potential with mirror symmetry, where instead of a constant potential condition ($V_{mj} = V_m$), a more general condition of mirror symmetry ($V_{mj} = V_{m(2N_z+j-1)}$) could be used. Note that this does not imply that all symmetric potentials will cause a perfect reflection, just the ones creating a pn junction.

Conductance in the armchair ribbons (Figs. 4.5(c) and 4.5(d)) also exhibits abrupt changes. These peaks do not coincide with new modes opening in the constriction. This leads us to search for a different explanation of their origin.

The two studied zigzag ribbons are just two extreme cases of intervalley

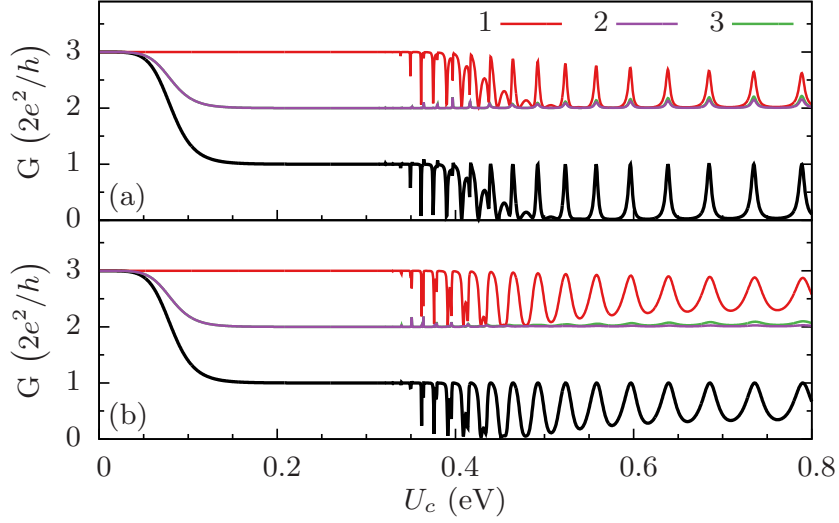


Figure 4.7: Conductance (thick black lines) through the zigzag ribbon as a function of the side gate potential for $\Delta x = 0.5l_c$ (a) and $\Delta x = l_c$ (b). The Fermi energy is 0.3 eV. Similarly to Fig. 4.4, transmissions of individual modes are displaced by $\Delta T = 2$.

scattering according to Ref. [60]. Here we show that by introducing a small misalignment between the side gates (which tunes the ratio of forward and backward intervalley scattering) the results for the zigzag ribbon can be continuously changed to resemble the ones for the anti-zigzag ribbon. The ratio of backward and forward intervalley scattering can be tuned by changing the misalignment between the two side gates (Δx). Results for the zigzag ribbon for different misalignments are presented in Fig. 4.6. With increasing Δx , the conductance map of the zigzag ribbon starts to resemble the one of the anti-zigzag ribbon shown in Fig. 4.5(b). At first, narrow conductance peaks appear, and as the forward scattering rises they broaden until the ribbon becomes fully conductive in the low energy region. These results, and that of Ref. [60] point out that beside the purity of the nanoribbon, one of the main prerequisites for observation of the valley-valve effect in experiments is a good control of the ribbon gating. Perfect electron reflection or perfect transmission can be observed in both ribbon types, zigzag and anti-zigzag, depending on the gate misalignment. Therefore control of the misalignment between the side-gates or in other words, between the p - n interfaces on the opposite ribbon edges, is of crucial importance for experimental observation of this effect.

Behaviour of individual modes with changing Δx is presented in Fig. 4.7. The abrupt positive conductance peaks in Fig. 4.7(a) are very similar to the ones in Fig. 4.4(a), but now they all originate from the first mode, and not from the second and the third mode. Change of the ratio of intervalley scattering has led to recomposition of scatterings inside the constriction, blocking the second and the third mode in favor of the first mode.

4.6 Fano resonances

Previously it was pointed out [55] that sudden changes in the conductance of the zigzag ribbons are Fano resonances [63]. To confirm this, and to extend it to the armchair ribbons, we plotted the eigenenergies of a closed system (a ribbon detached from the leads) on top of the conductance data in Fig. 4.8. We focus on a narrow range of E and U_c values as indicated by the white rectangles in Fig. 4.5. A closed system is defined by the two new lateral edges along the y direction. In the zigzag and anti-zigzag ribbons these new edges are of the armchair type, while in the armchair ribbons they are of the zigzag type.

The sudden changes in the conductance follow closely the eigenlevels of a closed system. In all four ribbons the eigenlevels go along and switch between two groups of lines. The first group appears not to depend on the gate potential and spans over the whole range of Fig. 4.5 (not shown). The second group is linearly dependent on U_c . Differences between these two groups of eigenlevels are best seen if we look at their corresponding wave functions. The probability densities of the four states labeled in Fig. 4.8 (Ψ_i , $i=1, 2, 3, 4$) are shown in Fig. 4.9. Because of the similarity of results for ribbons with the same edge type (for example between the zigzag and the anti-zigzag ribbon) we showed results only for two ribbons with different edges.

States Ψ_2 and Ψ_4 are from the first group of states (not dependent on U_c) and they occur because of the quantization along the x and y direction due to the final dimensions of a closed system. These states appear even when there is no side gate potential. For a finite potential their probability distributions are pushed toward the lateral edges, leaving a low probability region in the center of the constriction. States Ψ_1 and Ψ_3 , from the second group, occur because of the quantization due to the final dimensions of the high potential regions. Their eigenenergies are always lower than U_c , and

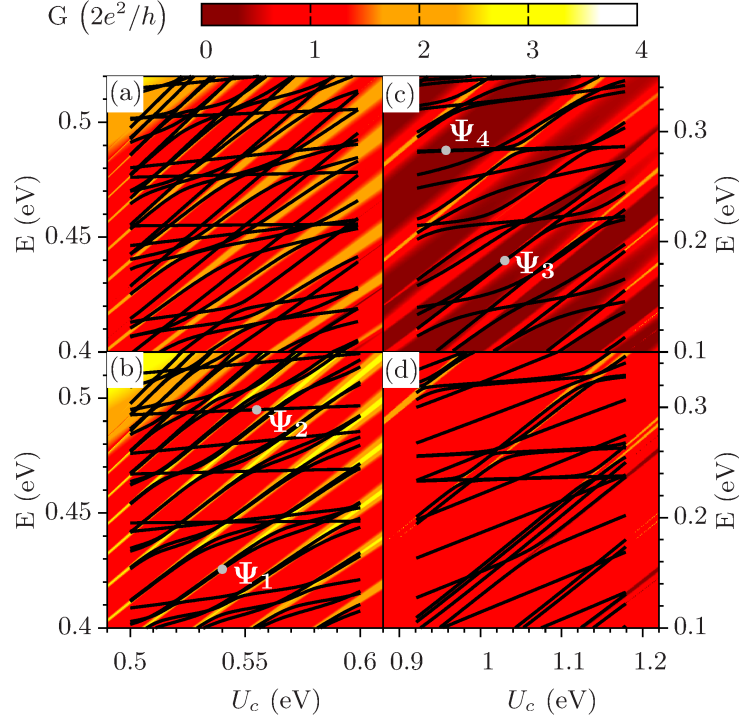


Figure 4.8: Comparison between the conductance of an open system and the eigenenergies (black lines) of a closed system (a ribbon detached from the leads) for the zigzag (a), the anti-zigzag (b), the semiconducting armchair (c), and the metallic armchair (d) ribbon. E and U_c run over the ranges bounded by the white rectangles in Fig. 4.5.

they are localized in areas where $U(x, y)$ goes above their eigenenergy. In the zigzag ribbon the $|\Psi_1|^2$ peaks on the p - n interfaces near the edges, with the wave function peaks of each sublattice associated with one of the edges.

The length of a closed system is set to 45 nm, which leaves some dangling atoms on the new lateral edges, particularly in the armchair ribbons. These atoms affect our results, but do not alter the states from the second group. Because these states are localized in the high potential regions, they do not significantly depend on the boundary conditions on the new lateral edges (along the y direction), or for example the length of the ribbon.

It has been shown [64, 65] that considering only the nearest neighbour interaction in graphene quantum dots and zigzag ribbons can lead to unphysical effects which vanish when next-nearest neighbor hoppings are added. To make a numerical verification that this is not crucial in a situation with

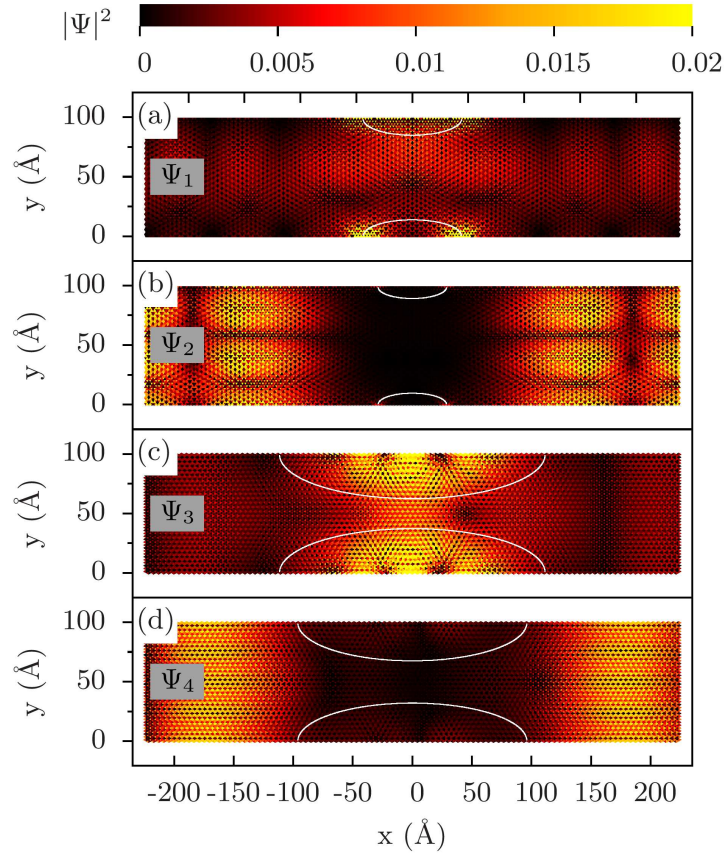


Figure 4.9: The probability density of the eigenstates Ψ_i ($i=1, 2, 3, 4$) from Fig. 4.8. The white lines are equipotential lines for which $U(x, y)$ is equal to the eigenstate energy.

nonuniform onsite potential, we include the next-nearest neighbour hoppings ($t'=0.1t$) and repeat the calculations from Fig. 4.8. Results are presented in Fig. 4.10. In general, the inclusion of next-nearest neighbour hoppings shifts the dispersion relations in energy for approximately ~ 0.8 eV and the dispersionless edge states in zigzag ribbons become dispersed. Beside the change of energy scale, the qualitative features of Fig. 4.8 remain unchanged when next-nearest neighbour interaction is included. The only difference that we noticed is the reduction of number of anti-resonances in the zigzag ribbon, We now observe just one of two anti-resonances, and they do not show a total reflection, meaning that G does not reach zero at anti-resonance point. One possibility is that narrow anti-resonances are smeared out due to this

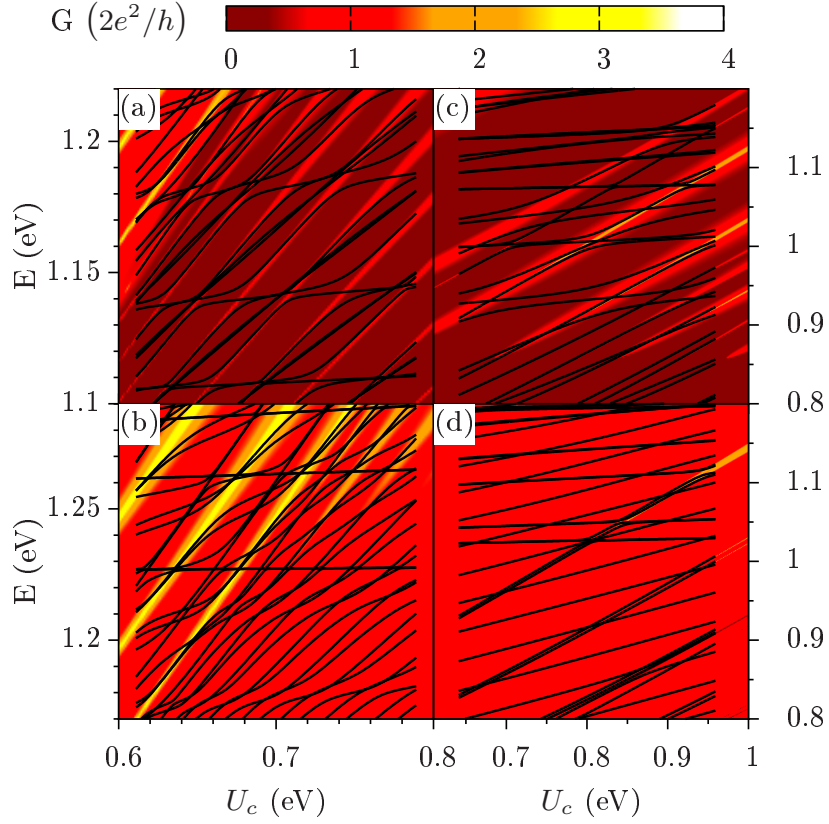


Figure 4.10: Comparison between the conductance of an open system and the eigenenergies (black lines) of a closed system (with next-nearest neighbor interaction included, $t' = 0.1t$) for the zigzag (a), the anti-zigzag (b), the semiconducting armchair (c), and the metallic armchair (d) ribbon.

partial reflection, the other is that they are very narrow, beyond the current resolution of our calculations.

The presented match between the conductance peaks and the positions of the eigenlevels indicate that these peaks originate from the Fano resonances. To test this further we fitted some of them with the normalized Fano curve

$$f(\epsilon) = \frac{1}{1+q^2} \frac{(\epsilon+q)^2}{1+\epsilon^2}, \quad \epsilon = (E - E_0)/\Gamma, \quad (4.6)$$

to obtain E_0 (the peak position), Γ (the width of the resonance), and q (the shape parameter). The fitted curves are shown in Fig. 4.11. Although all the peaks in Fig. 4.11 look symmetric, they actually exhibit a small asymmetry

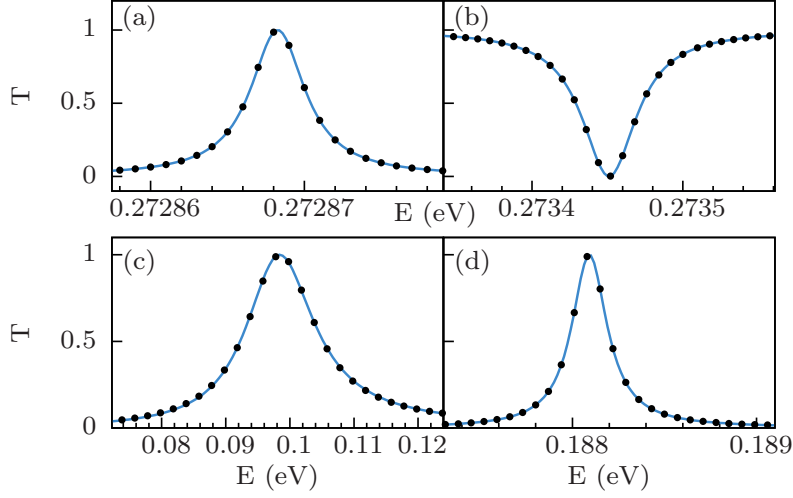


Figure 4.11: Fano resonances: comparison between the numerical results obtained by KWANT (dots) and lines fitted by the normalized expression for the Fano resonance. (a) The sum of transmissions of the second and the third mode for the zigzag ribbon $U_c=0.3$ eV. (b) The transmission of the first mode for the zigzag ribbon $U_c=0.3$ eV. (c) The transmission of the first mode for the semiconducting armchair ribbon $U_c=0.45$ eV. (d) The sum of transmissions of the second and the third mode for the metallic armchair ribbon $U_c=0.9$ eV.

which is best fitted by a Fano line shape, as is clearly apparent from the figure.

4.7 LDOS and the electrical current

Previous resonances are also characterized by a specific behaviour seen in the local density of states (Fig. 4.12) and the electron current (Fig. 4.13).

The fact that most of the electron transport in ribbons with zigzag edges in the low energy regime is a consequence of intervalley scattering [60] can be seen in Figs. 4.12(a) and (b). The kinetic energy of the edge states decreases as they propagate through the constriction, and they are pushed closer to the edge of the ribbon, creating peaks in the LDOS at the p - n interfaces. Peaks on the two sublattices appear on the opposite edges, similarly to peaks in the wave functions of the eigenstates.

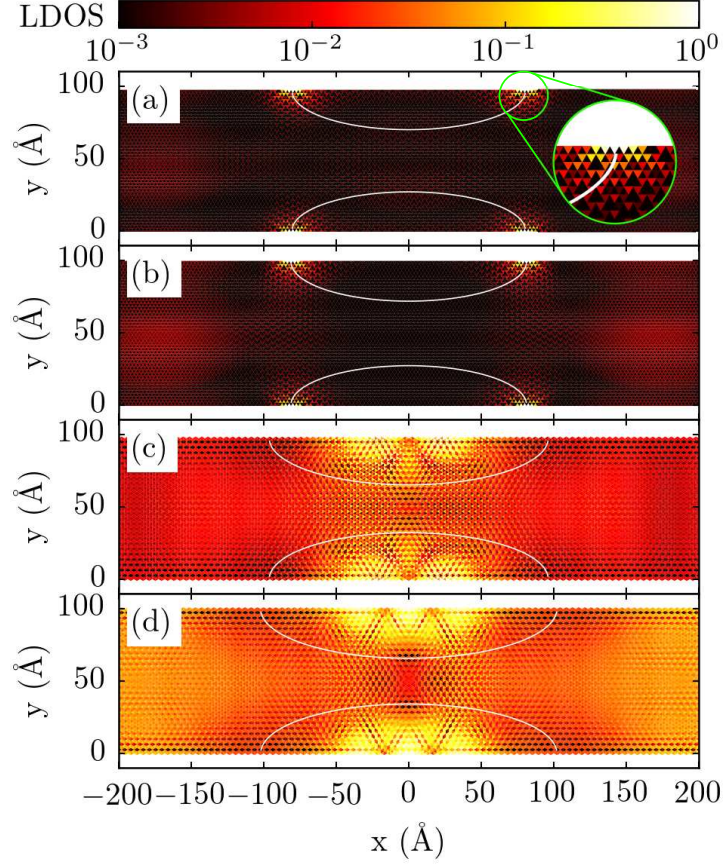


Figure 4.12: LDOS at $E = 300$ meV for the zigzag ribbon at $U_c = 737$ meV (a), the anti-zigzag ribbon at $U_c = 750$ meV (b), the metallic armchair ribbon at $U_c = 1084$ meV (c), and the semiconducting armchair ribbon at $U_c = 1276$ meV (d). The white lines are equipotential lines for which $U(x, y) = E$.

In armchair ribbons the LDOS starts decreasing in the areas of applied gate potential as U_c rises from zero to E_F . When U_c goes above the Fermi energy, a high local density of states appears in the gate potential regions. Very high densities occur at conductance peaks, resembling the wave functions in a closed system.

Since KWANT does not provide a direct procedure to obtain the electron current, we calculated current on the i -th atom using

$$\mathbf{j}_i(E) = \frac{4e}{h} \sum_n \sum_{j=1}^3 \text{Im} [\Psi_i^{n*}(E) H_{ij} \Psi_j^n(E)] \mathbf{d}_{ij}, \quad (4.7)$$

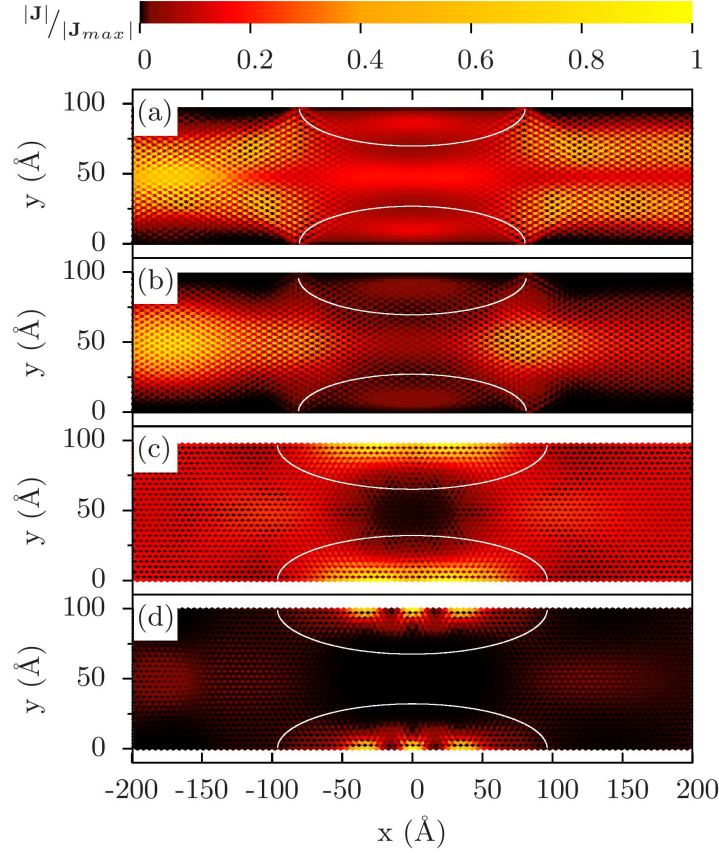


Figure 4.13: The relative current density at $E = 300$ meV for the same parameters as in Fig. 4.12.

where H_{ij} is the Hamiltonian element between i -th and j -th atoms, Ψ_i^n is the wave function of the n -th incoming mode on the i -th atom, and \mathbf{d}_{ij} is a unit vector between the two neighbouring atoms. In order to present all results in one graph (Fig 4.13), we scaled the current intensities relative to the maximal current in the system $|\mathbf{j}_{\max}|$.

The current behaviour in the zigzag ribbon, near one of the conductance peaks, is shown in Fig. 4.13(a) and in the anti-zigzag ribbon in 4.13(b). In both these ribbons, the current in the constriction experiences a uniform flow in the x direction. Current in the zigzag ribbon shows no change in direction when U_c goes from one side of the conductance peak to the other.

In armchair ribbons, when there is no gate potential, the current near the edges flows only along certain separate horizontal lines of carbon atoms.

Further away from the edges these lines mix, meaning that the current flows between them. Similar results were reported in Ref. [66] where it was shown that the current flow along these *streamlines* depends on the ribbon width, and these streamlines are used to explain how the sensitivity of the ribbon conductance depends on a transverse position of a single adsorbate. Our results point out additionally that when exposed to the side gate potential, these streamlines mix at the beginning of the constriction, with most of the current tending to flow near the edges in the high potential regions (Figs. 4.13(c) and 4.13(d)).

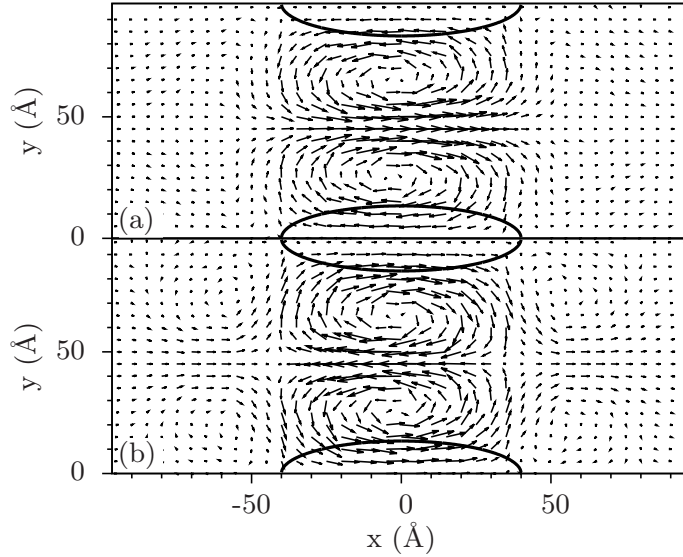


Figure 4.14: The current in the zigzag ribbon at $E = 0.3 \text{ eV}$ for (a) $U_c = U_{\min} - \Delta u$ before the zero-conductance dip, and (b) $U_c = U_{\min} + \Delta u$ after the zero-conductance dip ($U_{\min} = 374.82 \text{ meV}$, $\Delta u = 0.15 \text{ meV}$). For clarity, results are averaged and presented on a square mesh.

Another transport property is different behaviour of the electrical current in the zigzag ribbon near the positive conductance peaks as compared to the behaviour near the zero-conductance dips. The current near one of the zero-conductance dips is shown in Fig. 4.14. It is characterized by the occurrence of two vortices (one in the upper and one in the lower half of the ribbon) rotating in the opposite directions. When U_c crosses the zero-conductance potential, the spinning direction of these vortices changes. As U_c approaches closely the anti-resonance potential, the current inside the

constriction starts flowing in a closed loop, and its intensity starts decreasing, reaching almost zero at the anti-resonance minimum. This is similar to Kekulé like currents reported in bearded ribbons and ribbon junctions. [53, 54] According to these references, the anti-resonances are interpreted as superpositions of two states mutually connected by time reversal operation. Breaking of the time reversal symmetry (for example, by introduction of external magnetic field) eliminates these dips and smooths out the conductance. Including the next-nearest neighbor interaction in calculations does not lead to qualitative change in the current patterns, except for the anti-resonance points. As we noted previously, including the next-nearest neighbor interaction reduces the number of anti-resonances. Change in the current flow direction at anti-resonance points still occurs, but it is less pronounced than in the case without additional hopping terms, meaning that narrow current vortices appear close to the edges.

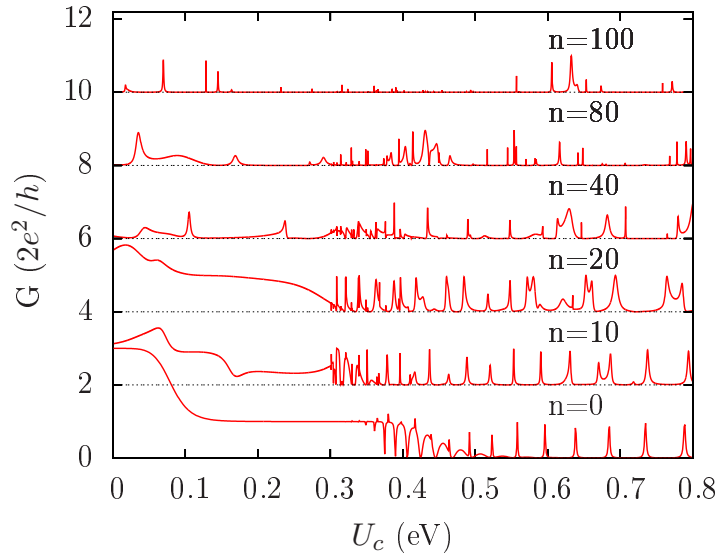


Figure 4.15: Conductance through the zigzag ribbon as a function of the side gate potential for different number (n) of randomly removed carbon atoms. The Fermi energy is $E = 300$ meV. For clarity, results for different n -s are moved vertically by $\Delta T = 2$.

4.8 Fano resonances in GNR: Conclusion

Before stating our conclusions, we make few notes regarding actual experiments [50, 51]. Although ideal armchair nanoribbons can be produced by bottom-up approach [52], and production of ideal zigzag ribbons could be possibly achieved in the near future using different precursors, the experiments up to now deal with disordered ribbons. The presence of bulk and edge disorder suppresses electron transport, and leads to localisation. In contrast to this, our system is in different (ballistic) regime where interference effects are seen more clearly. Here we investigate the effects of a special type of disorder, a random distribution of vacancies, on our results (a more detailed study of vacancy effects in graphene in high magnetic fields is given in the following chapter). Figure 4.15 shows how conductance of the zigzag ribbon presented in Fig. 4.4(a) changes when we randomly remove n carbon atoms. For the reference, the whole ribbon contains approximately ~ 19000 atoms. Conductance is considerably suppressed with increase in the number of random vacancies. Notice that some of the resonance peaks (for U_c approximately above 0.5 eV) remain unaffected for small number of vacancies. New resonant peaks also appear due to change in the ribbon structure. These results suggest that our findings could be still applicable in the limiting case of very low level of disorder created by the vacancies, where just few carbon atoms are removed from the graphene lattice, with addition of new resonances originating from these vacancies.

To conclude, in this chapter we investigated electron transport in four types of graphene nanoribbons with potential constriction created by two side gates. In zigzag ribbons, the application of side gate potential deforms of the lowest conduction band, which allows for modes from both conduction and valence bands to coexist in the constriction region. The change in the ratio of backward and forward intervalley scattering, introduced through the side gate misalignment, leads to a reorganisation of modes that are transmitted through ribbons with zigzag edges. The reason is that in the low energy regime, the individual modes compete to populate a small number of states available in the constriction.

Transport in these narrow ribbons is characterized by abrupt changes in the conductance, which occur whenever there is an eigenstate in a closed system. These resonances have a specific signature in their current patterns and the LDOS. In zigzag ribbons, LDOS peaks at the pn interfaces near the edges, while in the armchair ribbons it is concentrated in the high potential

areas, resembling the bound states in a closed system. In zigzag ribbons the current is suppressed at the zero-conductance anti-resonances, flowing along vortices and changing the flow direction as the system goes through the anti-resonance dip. On the other hand, at positive conductance peaks, the current flows uniformly across the whole constriction. In the armchair ribbons there is a mixing of individual horizontal current streamlines at the beginning of the constriction, and the current inside the constriction tends to flow along high potential areas, near the edges of a ribbon.

4.8. Fano resonances in GNR: Conclusion

CHAPTER 5

Vacancy disorder in graphene Hall bars

5.1 Introduction

At the end of the previous chapter we briefly touched upon the subject of disorder in graphene. The disorder was introduced in the form of carbon atom vacancies. In this chapter* we will further investigate effects of vacancy disorder, but in the quantum Hall regime, when graphene sheets are exposed to quantizing external magnetic fields. Ever since its discovery [47], graphene generated new interest in the quantum Hall effects governed by relativistic particles. Quantum Hall resistance plateaus different from those of a classical 2DEG were observed in graphene [67, 68]. A comparison between experimentally measured quantized resistances in a classical 2DEG and in graphene is presented in Fig. 5.1. Later experiments reported new, more detailed features such as the splitting of the zeroth Landau level (LL) due to breaking of the valley and spin degeneracies [69, 70].

Disorder in experimentally available honeycomb graphene lattices is inevitable, whether it is structural like reconstructed and non-reconstructed vacancies, substituted carbon atoms, or it originates from charged impurities such as adatoms. Therefore disorder in graphene is a very active area of

*Results presented in this chapter are based on our publication: M. D. Petrović, F. M. Peeters, *Quantum transport in graphene Hall bars: Effects of vacancy disorder*, Physical Review B **94**, 235413 (2016).

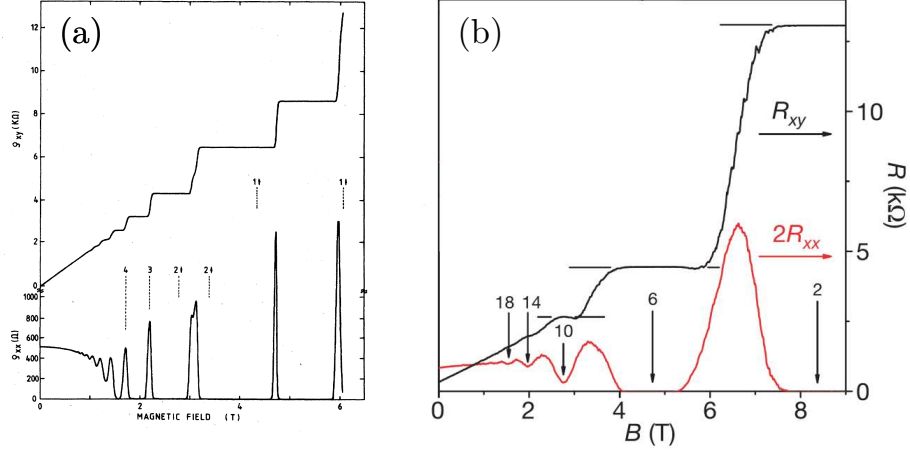


Figure 5.1: Comparison between experimentally measured quantization in the Hall resistance for (a) semiconductor heterostructure (b) graphene. Quantization in graphene is different due to its valley degrees of freedom. Figures are taken from Refs. [71] and [72], respectively.

research, both experimentally in devising ways to characterize it [73], and theoretically in studying its influence on electron transport [74, 75], with even possible applications in future spintronic devices [76]. Carbon atom vacancies can be introduced in graphene by ion irradiation. An STM image of monovacancies on the surface of graphite is shown in Fig. 5.2 (the figure is taken from Ref. [73]). Due to the relativistic nature of its charge carriers, disordered graphene offers a tabletop environment for the study of previously experimentally inaccessible phenomena, such as the atomic collapse reported recently in charged vacancies in graphene [77]. Vacancy disorder in case of a zero external magnetic field was extensively studied in Refs. [78, 79, 80], where new states localized around missing carbon atoms were reported. Effects of vacancies in the quantum Hall regime were studied in Refs. [81, 82], which reported on the occurrence of a zero-resistance quantum Hall plateau, and breaking of the Landau level degeneracy. Graphene with on-site potential disorder was also used in Ref. [83] to test a new numerical approach to calculate the Kubo conductivities.

In this chapter we simulate the transport of electrons in a Hall bar made from a single layer of graphene. Our main goal is to study the influence of various types of vacancy disorder on the electron transport in the quantum

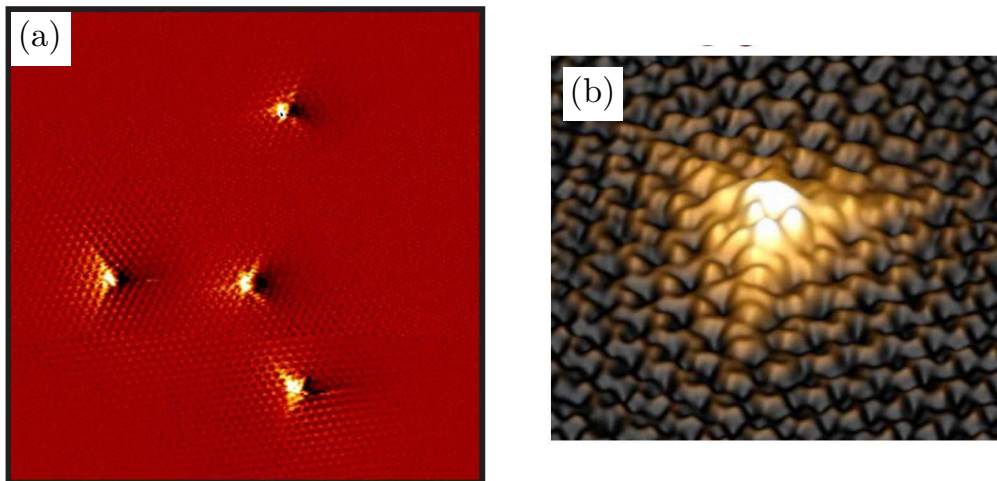


Figure 5.2: (a) Single atom vacancies imaged using STM on an irradiated surface of graphite. (b) a 3D image of a single monovacancy. Both insets are taken from Ref. [73].

Hall regime. We report that vacancy disorder can cause the appearance of new states in the Landau spectrum, which are observable in the bend resistance as well as in the total density of states (DOS) and in the distributions of eigenenergies in a closed system (a system detached from the leads). For monovacancies the energies of these new states scale as the square root of the magnetic field, similarly to the energies of relativistic Landau levels, but with a different scaling coefficient. The local density of states (LDOS) reveals a strong localization around the monovacancy sites, with localization length proportional to the cyclotron radius. The localization on divacancies is somewhat different: their localization energy scales linearly with the magnetic field, while their localization radius appears to be constant. We further study how the electron current flows in the presence of vacancies, and what are the effects of the next nearest neighbor interaction (NNN).

The rest of this chapter is organized as follows: In Sec. 5.2 we describe our system and methods used to obtain our results. The graphene tight-binding Hamiltonian was already introduced in previous chapters, but here we additionally implement magnetic field in graphene through Peierls phase factor, and we also use the specific four-terminal formula derived by Büttiker, which is a special case of the more general N -terminal formula introduced in the previous chapters. In order to focus on specific aspects of the problem,

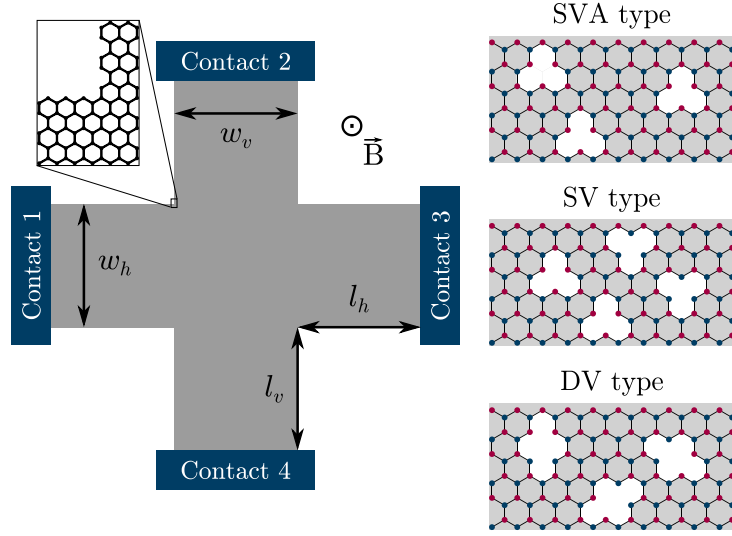


Figure 5.3: Graphene Hall bar system (left), and three studied disorder types (right). Widths of the horizontal and vertical leads are set to $w_h = 49.71$ nm, and $w_v = 49.94$ nm, respectively, while lengths of the horizontal and vertical arms (l_v and l_h) are equal, and set to 50 nm. Before disorder is introduced, all edges are considered to be clean, meaning that there are no dangling bonds on them.

ranging from vacancy concentration to NNN hopping, we discuss our results (Sec. 5.3) in several subsections (from 5.3.1 to 5.3.5). All these insights are combined and summarized at the end of this chapter, in the last (concluding) section (Sec. 5.4).

5.2 System and Methods

The studied system is shown in Fig. 5.3, it is a graphene Hall bar with zigzag edges along the horizontal leads, and armchair edges along the vertical leads. The width of the vertical, armchair, arms (w_v) is chosen so that the corresponding leads are metallic, meaning that there is no gap around zero energy.

We introduce vacancy disorder in this system by randomly removing carbon atoms from the graphene lattice. Three different disorder types are studied, as shown in the right insets in Fig. 5.3. The first is a single vacancy/single sublattice disorder (SVA). Here, we randomly remove carbon

atoms only from one sublattice (e.g. sublattice A). The second type is ordinary single vacancy disorder (SV), where carbon atoms are removed without any respect to the sublattice to which they belong. The third type is a double vacancy disorder (DV), where only pairs of neighbouring atoms, each belonging to a different sublattice, are removed. It is known that single vacancies (or monovacancies) break the sublattice symmetry, while divacancies preserve it. Here we choose two types of monovacancy distributions, since one (SV) should preserve the sublattice symmetry on the average, while the other (SVA) is the extreme case of sublattice symmetry breaking.

When discussing the effects of vacancy disorder it is important to investigate the general effects introduced by disorder and to separate them from effects that occur only for some specific disorder distributions. Therefore we will present two types of results. In order to capture the general disorder effects, for each disorder type and concentration, we perform calculations over a sample of $N = 10$ different vacancy distributions. Results for specific distributions R_i ($i = 1, 2, \dots, 10$) are then averaged $\bar{R} = \sum_{i=1}^N R_i/N$ (we mark the averaged quantities with a bar line on top). On the other hand, in order to better understand the origin of these effects, we often analyze results for some specific distribution, or compare results of several different distributions.

As in the previous chapter, for our numerical calculations we use KWANT.²⁷ The graphene tight-binding model Hamiltonian

$$\hat{\mathbf{H}} = \sum_{\langle i,j \rangle} (\tilde{t}_{ij} \hat{c}_i^\dagger \hat{c}_j + H.c.) + \sum_{\langle\langle i,k \rangle\rangle} (\tilde{t}'_{ik} \hat{c}_i^\dagger \hat{c}_k + H.c.) \quad (5.1)$$

is now slightly different than that presented in Chapter 4. Operators \hat{c}_i^\dagger (\hat{c}_i) still create (annihilate) a p_z electron on the i -th carbon atom, but no external electric potential is included, except that of the back gate which controls the Fermi energy. The hopping terms $\tilde{t}_{ij} = t e^{i\varphi_{ij}}$ and $\tilde{t}'_{ik} = t' e^{i\varphi_{ik}}$ are defined using the electron nearest neighbor hopping energy $t = -2.7$ eV, the NNN hopping term t' , and the Peierls phase factor φ_{ij} (which we discuss below). Although most of our results deal only with nearest neighbor interaction ($t' = 0$), in the last subsection of the next part (5.3.5) we comment on the effects of a nonzero NNN term.

Defining a magnetic field in a multi-lead system, where some leads point in different directions, is a problem that needs to be carefully considered. The vector potential along the leads needs to be translatory invariant in order to simulate each lead as a semi-infinite system. Following this condition, we

set the vector potential in horizontal leads using the Landau gauge $\mathbf{A}_H = -By\mathbf{e}_x$, and that in vertical leads as $\mathbf{A}_V = Bx\mathbf{e}_y$. To connect these two, the gauge in the main region is set to change smoothly from \mathbf{A}_H to \mathbf{A}_V in the upper and lower arms of the cross. This is achieved by using an additional scalar function $f(x, y)$ which rotates the vector potential $\mathbf{A}' = \mathbf{A} + \nabla f$ locally, without changing the orientation and strength of the magnetic field. This scalar function is defined in Ref. [84] as

$$f(x, y) = Bxy \sin^2 \theta + \frac{1}{4}B(x^2 - y^2) \sin 2\theta, \quad (5.2)$$

where θ is the angle of rotation. In order to apply $f(x, y)$ only in a specific subregion of the cross, we multiply it with a smooth step function $\xi_i(y) = \frac{1}{2}[1 + \tanh(2(y - y_0)/d)]$, which is nonzero only very close to one of the vertical leads (here the index i specifies the lead number). Previous expression defines y_0 as a crossover position, where $\xi_i(y_0) = \frac{1}{2}$, and d as a width of the crossover region, where ξ_i smoothly goes from 0 to 1. For our numerical calculations we used $d = l_v/5 = 10$ nm. Based on this, we can define a rotation function for the second lead

$$\begin{aligned} F_2(x, y) &= f(x, y)\xi_2(y) \\ &= \frac{1}{2}Bxy \left[1 + \tanh \left(2\frac{y - y_u}{d} \right) \right], \end{aligned} \quad (5.3)$$

and similarly for the fourth lead

$$\begin{aligned} F_4(x, y) &= f(x, y)\xi_4(y) \\ &= \frac{1}{2}Bxy \left[1 + \tanh \left(2\frac{y_d - y}{d} \right) \right]. \end{aligned} \quad (5.4)$$

In both cases θ is set to $\pi/2$ (since neighboring leads are perpendicular to each other), and $y_u = -y_d = (l_v + w_h)/2$. We also define the sum of the two rotation functions as $F = F_2 + F_4$.

In order to check that the modified vector potential $\mathbf{A}'(x, y) = \mathbf{A}(x, y) + \nabla F(x, y)$ is properly defined, this function is presented in Fig. 5.4. The \mathbf{A}_H gauge oriented in the x direction in the horizontal part of the cross transforms smoothly to a y oriented gauge \mathbf{A}_V in the vertical part of the cross, thus confirming the correctness of \mathbf{A}' .

Note that functions ξ_2 and ξ_4 are chosen because they are smooth, thus guaranteeing the smoothness of the vector potential. But in a tight-binding system, due to its discreteness, and the constant distance between the atoms,

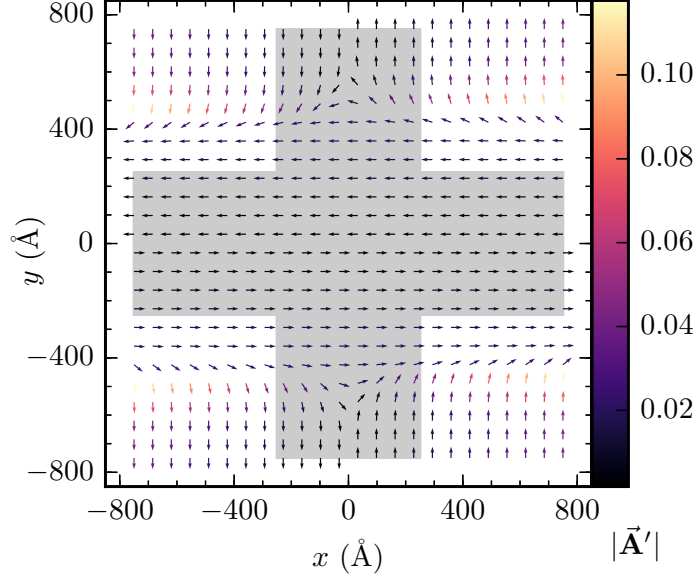


Figure 5.4: Modified vector potential $\mathbf{A}'(x, y)$: arrows show the direction of $\mathbf{A}'(x, y)$, and their color represents its intensity. System shape is marked by the gray area. The derivation of the vector potential is presented in Appendix B.

this is not a necessary condition. The discontinuous Heaviside step function could also be used instead. We tested this by changing the width d from a value used in all our calculations ($d = l_v/5$), to values well below the carbon-carbon distance (equivalent to a discontinuous step function), with no observable changes in the final results.

The Peierls phase factor between sites i and j for the modified vector potential is

$$\begin{aligned}
 \varphi_{ij} &= \frac{e}{\hbar} \int_{\mathbf{r}_j}^{\mathbf{r}_i} (\mathbf{A}_H + \nabla F) \cdot d\mathbf{r} \\
 &= \frac{e}{\hbar} \int_{\mathbf{r}_j}^{\mathbf{r}_i} \mathbf{A}_H \cdot d\mathbf{r} + \frac{e}{\hbar} (F_i - F_j) \\
 &= \varphi_{ij}^L + \Phi_i - \Phi_j,
 \end{aligned} \tag{5.5}$$

where φ_{ij}^L is the Peierls phase factor for the translatory invariant Landau

gauge in the x direction

$$\varphi_{ij}^L = -\frac{e}{\hbar} B \frac{(y_i + y_j)}{2} (x_i - x_j), \quad (5.6)$$

as is also explained in Ref. [85]. Note that φ_{ij}^L does not depend on the x coordinates, since differences $x_i - x_j$ are constant.

Resistances in this four-terminal device are obtained using the Landauer-Büttiker formula [86, 87, 28]

$$R_{mn,kl} = \frac{h}{2e^2} (T_{km}T_{ln} - T_{kn}T_{lm}) / D, \quad (5.7)$$

where $R_{mn,kl}$ is a resistance measured when the current is injected from lead m and collected at lead n , and the voltage is measured between leads k and l . T_{ij} is the transmission function between the corresponding leads, while parameter D is defined as

$$D = (\alpha_{11}\alpha_{22} - \alpha_{12}\alpha_{21}) S, \quad (5.8)$$

where

$$\alpha_{11} = (T_{21} + T_{31} + T_{41}) - (T_{14} + T_{12})(T_{41} + T_{21})/S, \quad (5.9)$$

$$\alpha_{22} = (T_{12} + T_{32} + T_{42}) - (T_{21} + T_{23})(T_{12} + T_{32})/S, \quad (5.10)$$

$$\alpha_{12} = (T_{12}T_{34} - T_{14}T_{32})/S, \quad (5.11)$$

$$\alpha_{21} = (T_{21}T_{43} - T_{41}T_{23})/S, \quad (5.12)$$

with

$$S = T_{12} + T_{14} + T_{32} + T_{34}. \quad (5.13)$$

The previous resistance formula (Eq. 5.7) defines six different resistances, and when used with transmission functions at a specific Fermi energy $T_{ij}(E_F)$ it provides resistances for the zero temperature case. To obtain the resistances at a nonzero temperature, the previously calculated transmission functions need to be additionally convoluted in energy

$$T'_{ij}(E_F, T) = \int_{-\infty}^{\infty} T_{ij}(E') F_T(E' - E_F) dE', \quad (5.14)$$

where the convolution function [4]

$$F_T(E, T) = \frac{1}{4k_B T} \operatorname{sech}^2 \left(\frac{E - E_F}{2k_B T} \right), \quad (5.15)$$

is the temperature dependent negative derivative $F_T(E) = -\partial f/\partial E$ of the Fermi-Dirac distribution

$$f(E) = \frac{1}{\exp[(E - E_F)/k_B T] + 1}. \quad (5.16)$$

Since vacancy disorder introduces a considerable amount of noise in all calculated quantities, in some cases we perform temperature smoothing by setting $T = 16$ K, the temperature is considered to be zero otherwise. In case of the averaged results, the temperature smoothing is always performed before the averaging.

5.3 Results

5.3.1 Effects of different disorder types

Here we discuss the general transport effects of the three disorder types, observable in the Hall ($R_H = R_{13,42}$), and the bend ($R_B = R_{12,43}$) resistances. Note that actual Hall measurements are usually performed on devices with six or more terminals, with current and voltage probes usually set on different terminals. That is why we focus here on the bend resistance R_B , and not on $R_{13,13}$, since R_B should be closer to experimentally measured R_{xx} .

It is widely known [14] that the Hall resistance in graphene exhibits quantized plateaus

$$R_H = \left(\frac{h}{2e^2}\right) \frac{1}{1 + 2n}, \quad n = 0, \pm 1, \dots \quad (5.17)$$

between the energies of the Landau levels

$$E_n = \text{sgn}(n) \sqrt{2eBv_F^2 \hbar |n|}, \quad (5.18)$$

where n is the Landau level number, and v_F is the Fermi velocity ($v_F = 3|t|a/2\hbar \approx 10^6$ m/s, with parameter $a = 1.42$ Å being the carbon-carbon distance). At the steps in the Hall resistance, the longitudinal resistance exhibits peaks. Beside these expected features, our results for a disordered system (presented in Fig. 5.5) show some additional features. Disorder type and concentration are shown in every subplot of Fig. 5.5, in the lower-left corner. Results for the bend resistance depend strongly on the vacancy concentration, therefore we scale \bar{R}_B by multiplying it with a scaling coefficient. This scaling is done in order to present all results in the same range. A scaling coefficient is presented in every subplot, above the vacancy concentration.

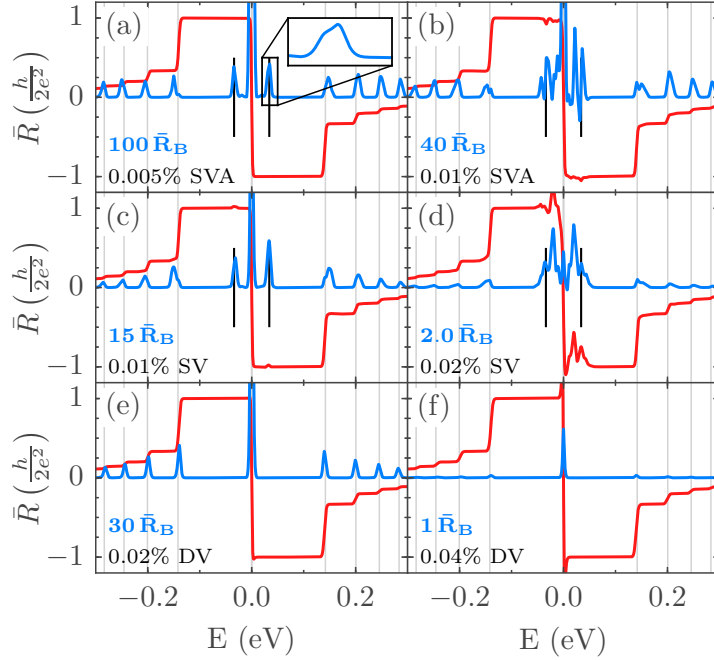


Figure 5.5: Average Hall ($\bar{R}_H = \bar{R}_{13,42}$, red curves) and bend ($\bar{R}_B = \bar{R}_{12,43}$, blue curves) resistances for various types and concentrations of vacancy disorder. Thin gray vertical lines mark the energy of Landau levels given by Eq. (5.18) for $B = 20$ T, while black vertical lines mark the position of the new peaks at $E = \pm 33.9$ meV. The temperature is 16 K.

Monovacancy disorders (SV and SVA) induce two new peaks in the bend resistance, around $E = \pm 33.9$ meV. These peaks do not agree with the analytic formula for Landau levels given by Eq. (5.18). In contrast, peaks induced by double vacancies (DV) appear to agree with Eq. (5.18) (i.e. they correspond to the expected Landau levels, broadened by temperature and vacancy scattering). Each row in Fig. 5.5 presents data for one type of vacancy disorder, for two different concentrations. For each vacancy type, the increase in vacancy concentration leads to an increase in R_B , which can be seen in a decreasing scaling coefficient (given in the insets of the figure). The higher the vacancy concentration the larger the bend resistance, and consequently the smaller the scaling coefficient. For higher concentrations (Figs. 5.5(b) and (d)), two peaks in \bar{R}_B are not well defined, and \bar{R}_H also slightly deviates from the expected Hall plateaus. Although we discuss the effects of a vacancy concentration further below, it is important to state that new peaks

in \bar{R}_B occur only in a certain range of concentrations, and that above some critical concentration, these peaks broaden and merge. This critical concentration depends on the ratio of the average vacancy-vacancy distance and the magnetic length. It also depends on the type of monovacancy disorder, since for SVA disorder, the two peaks disappear for smaller concentrations (0.01% in Fig. 5.5(b)) as compared to SV disorder (0.02% in Fig. 5.5(d)). Another interesting feature is the negative bend resistance in Fig. 5.5(b). As explained in Ref. [87] (page 321, below Eq. 13 in that reference), and in Ref. [28] (section 3.4.4.2 in that reference), Büttiker formula for a four terminal device can produce negative non-local resistances. This is usually the case when the second term in the numerator of Eq. (5.7) is larger than the first term. We obtain negative R_B peaks for almost all concentrations, but for low concentrations they do not appear often (because the scattering is weak), and are not very pronounced (they usually disappear after temperature smearing). In general, if the number of vacancies exceeds the critical value, vacancy scattering becomes too strong that no general features exist in the low energy region. The bend resistance then strongly depends on a particular vacancy distribution.

Another characteristic of the averaged resistance \bar{R}_B is that it is fairly symmetric with respect to electrons and holes, whereas results for individual distributions (used to calculate \bar{R}_B) are not. This means that in general a random monovacancy distribution induces two new peaks in the bend resistance, but the actual relative height of those two peaks depends on a particular arrangement of vacancies. For some distributions there is only one peak in R_B , at positive or negative energy, and for some distributions there are no peaks at all (a question which we address in subsection 5.3.4). This asymmetry between electrons and holes is expected, since exchanging electrons for holes is equivalent to flipping the magnetic field, which in turn is equivalent to keeping the field fixed and flipping the system around the z axis. A clean system is symmetric with respect to this transformation, but a disordered system is not. After the flip the incoming electrons see a different arrangement of vacancies. A vacancy distribution can be constructed to be symmetric with this flip transformation, in which case all results would also be electron-hole symmetric. This asymmetry between electrons and holes occurs only for a fixed field orientation ($R_B(E, B) \neq R_B(-E, B)$), and should not be confused with the case when both magnetic field and Fermi energy change sign. Results for electrons and holes are then symmetric: $R_B(E, B) = R_B(-E, -B)$.

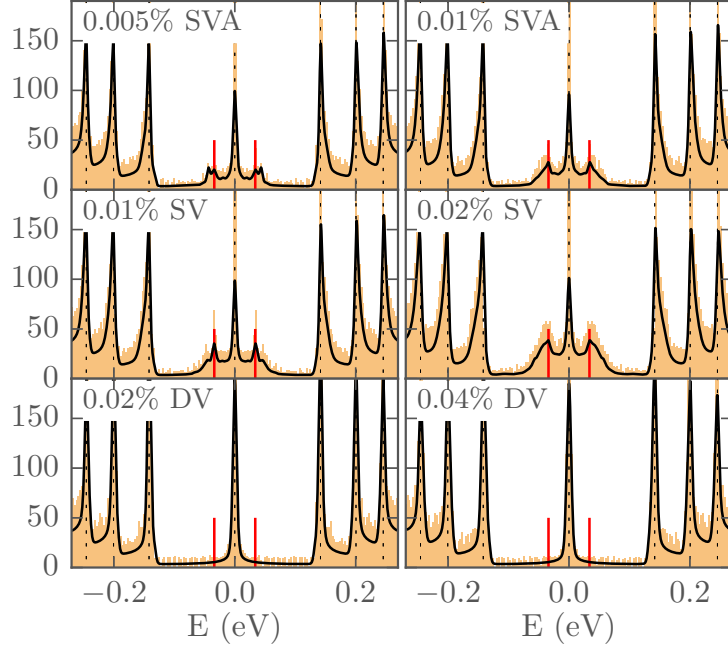


Figure 5.6: Averaged DOS (black curves, arbitrary units) and distributions of eigenenergies in a closed system (orange histograms in the background). Red lines mark the positions of the two new peaks at $E = \pm 33.9$ meV, while dotted lines mark the energies of Landau levels. Magnetic field is $B = 20$ T, and $T = 16$ K.

Results for the averaged total density of states (DOS) and distributions of eigenlevels in a closed system, presented in Fig. 5.6, are obtained for the same set of vacancy distributions as in Fig. 5.5, and they exhibit similar effects to those seen in the bend resistance in Fig. 5.5. For every vacancy type and concentration, the DOS is first smoothed and then averaged over $N = 10$ different vacancy samples. In case of the eigenenergies, results for positive energies for $N = 10$ distributions are summed without smoothing or averaging, and mirrored around $E = 0$ axis.

Monovacancy distributions induce two new broad peaks in the total DOS (around $E = \pm 33.9$ meV, marked with red lines in Fig. 5.6), while double-vacancy distributions appear only to broaden the DOS around the expected Landau levels. We show below that the energy of these broadened peaks ($E = \pm 33.9$ meV) corresponds to an energy of a monovacancy localized state. Similar behaviour is seen in distributions of eigenlevels in a closed system (a

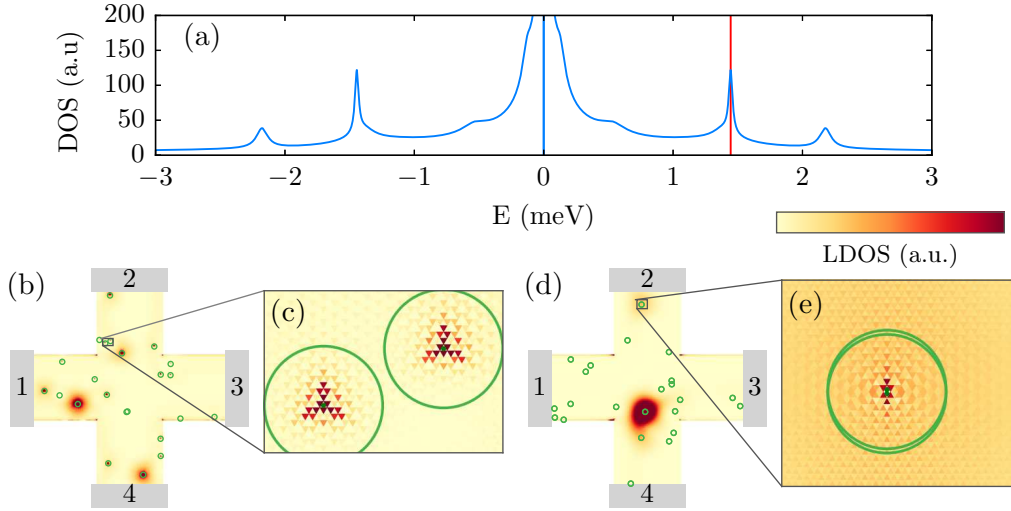


Figure 5.7: (a) DOS for a single DV distribution ($n = 0.01\%$, $B = 14$ T) (b) LDOS for a single SVA distribution ($n = 0.005\%$, $B = 20$ T) at the vacancy localization energy ($E = 33.9$ meV). (d) LDOS for a single DV distribution ($n = 0.01\%$, $B = 14$ T) at the localization energy ($E = 1.45$ meV, marked with red vertical line in (a)). (c) and (e) Zoom around particular vacancies in (b) and (d). Vacancies are marked with green circles and green dots in the center. Temperature is set to $T = 0$ K.

Hall bar detached from the leads). Usually, the eigenlevels of a closed system in a high magnetic field tend to cluster around the energies of the Landau levels. Here we plot histograms (orange areas in Fig. 5.6) showing how many eigenlevels occupy a narrow energy range around each energy, and these plots also show two distributions around $E = \pm 33.9$ meV.

According to Refs. [88, 81], divacancies in graphene should also induce new states in the Landau spectrum. Our results for DV distributions appear to contradict those of these two references. However, a higher resolution DOS plot around the zeroth Landau level (shown in Fig. 5.7(a)) for one particular DV distribution, reveals additional DOS peaks. These peaks are positioned only few meV away from the LLs, and that is why they were not well distinguishable from the LLs in the previous results. This suggests that additional peaks coming from the divacancies would be harder to observe experimentally, since they would be usually smeared by temperature.

Previous experiments on graphene in high magnetic fields [70] reported splitting of the zero Landau level, which was attributed to the breaking of

5.3. Results

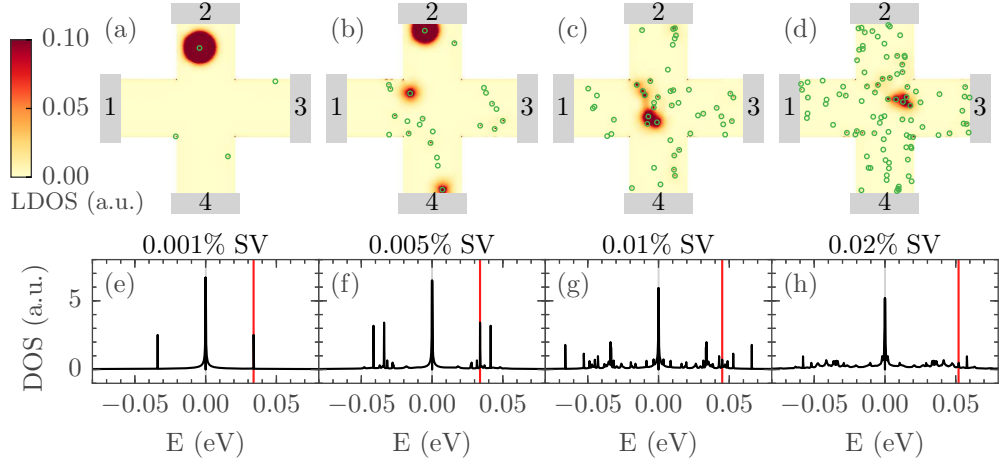


Figure 5.8: (a-d) LDOS for SV disorder type, for different vacancy concentrations: 0.001%, 0.005%, 0.01%, and 0.02%, and at different energies: 33.9 meV, 33.9 meV, 45 meV, and 52 meV, respectively. Vacancy positions are marked with green circles. (e-h) DOS for SV disorder type, for the corresponding concentrations. Energies at which we calculated LDOS in (a-d), are marked with red vertical lines in (e-h). Magnetic field is $B = 20$ T, and $T = 0$ K.

the sublattice symmetry. One of the possible explanations of the new DOS peaks is that they correspond to the occurrence of new states, localized in areas close to the vacancies. The unsplit zeroth Landau level is still present in the DOS of the whole device (for all disorder types), since it originates from local density of states (LDOS) in areas which are vacancy free. This connection between the new DOS peaks and the vacancy localized states becomes apparent if we look at the LDOS at one of the two peak energies. A LDOS at one of the two new peaks, for one particular SVA distribution, is shown in Fig. 5.7(b). The LDOS is highly localized around the vacancies (marked with green circles). A zoom in Fig. 5.7(c) shows states localized mostly on one sublattice, which could be connected with the breaking of sublattice symmetry. These states that are localized around single vacancies are the origin of the two new peaks in R_B and DOS. Similarly, in Figs. 5.7(d) and (e) we show LDOS for one particular DV distribution, at energy of one of the new peaks (marked with red line in Fig. 5.7(a)). Divacancies also induce localized states, but these states are localized equally on both sublattices, since divacancies do not break the sublattice symmetry. For

other energies (when there is no localization), divacancies act similarly to graphene structural armchair edges, namely LDOS spreads in areas between them, as if they repel it. Similar behaviour was observed in Ref. [81].

5.3.2 Changing vacancy concentration

As stated previously, all these results depend strongly on the vacancy concentration. To illustrate this, we present in Fig. 5.8 how DOS and LDOS change with increasing number of vacancies belonging to a SV disorder type. Here, we show results for specific vacancy distributions without any temperature smoothing or averaging. For low concentrations (Figs. 5.8(a) and 5.8(e)) DOS shows two well-defined peaks at ± 33.9 meV. These correspond to one state localized around one monovacancy. Other vacancies in Fig. 5.8(a) are very close to the system edges and localization on them is very weak. These results explain why smoothed and averaged R_B and DOS exhibit strong peaks around ± 33.9 meV, because this corresponds to the energy of a state localized around one isolated monovacancy. The localization happens at this specific energy only if a vacancy is in the bulk and sufficiently away from the system edges, but also far from the other vacancies, which is satisfied only for low concentrations. With increasing concentration, the average distance between the vacancies decreases, and vacancies start to “see” each other, meaning that they start to influence the formation of localized states on their neighbours. This is demonstrated in Figs. 5.8(b) and 5.8(f), where several peaks appear in the total DOS. However the peak at the monovacancy localization energy (± 33.9 meV) is still well defined. This is because there is still one well isolated monovacancy in the upper arm of the cross (see Fig. 5.8(b)). For even higher concentrations there are no longer well isolated vacancies, therefore there is no well defined localization energy. Instead, the monovacancies start to form something which resembles bond states. In a vague analogy with atoms and molecules, these bond states correspond to groups of vacancies which are sufficiently close to each other so that localization occurs over the whole group, and not on separated, individual vacancies. This bonding, shown in Figs. 5.8(c) and 5.8(d), is responsible for spreading of the localization energy and consequently for broadening of the new peaks in R_B and DOS.

5.3.3 Changing the magnetic field

In this part we investigate how these localized states behave when we change magnetic field B . In Figs. 5.9(a) and 5.9(b) we show that the localization energy for monovacancies scales with the square root of the magnetic field $E \sim \pm\sqrt{B}$, similarly to the relativistic Landau levels. The blue curves in Figs. 5.9(a) and 5.9(b) show the parabolic function $B = \alpha E^2$, where parameter $\alpha = 17500 \text{ T}/(\text{eV})^2$ is set to fit the peak positions. This dependence can also be expressed as $E = \pm\sqrt{\gamma 2ev_F^2\hbar B}$, where $\gamma \approx 0.057$. It is important to note that Fig. 5.9(a) presents results for the same vacancy distribution as Fig. 5.8(a), with only one monovacancy capable of sustaining the localized states. The DOS in this case exhibits two narrow peaks at positive and negative localization energy. For weak fields ($B < 5 \text{ T}$) these peaks are almost unobservable, whereas for stronger fields they become better and better defined in energy. Beside these two localization peaks, Fig. 5.9(a) shows some additional peaks for $B = 0 \text{ T}$ (e.g. two peaks at approximately $\pm 35 \text{ meV}$). According to Pereira et al. [78], localization of electrons on vacancies also occurs for $B = 0 \text{ T}$, but localization energy is then equal to zero, therefore these extra peaks should not be connected with the localized states. Indeed, a closer study reveals that these peaks originate from new modes opening in the leads, and can be predicted by calculating the lead minimal subband energies.

For larger concentration of monovacancies (Fig. 5.9(b)) the localization energy is not well defined, and the two narrow DOS peaks from Fig. 5.9(a) split into two distributions of peaks. As we explained in the previous subsection, this is mainly due to a decrease of the average vacancy-vacancy distance and is thus due to an increase of the interference between vacancies, resulting in the formation of bond localized states. Since the localization radius around a monovacancy is inversely proportional to the square root of the magnetic field (as we show below), the field strength determines how far a single vacancy actually “sees” its surroundings (i.e. it determines the bond length of previously described bond states). Because this length changes with magnetic field, various groups of vacancies bond together at different field strengths and the two distributions of DOS peaks in Fig. 5.9(b) evolve quite unpredictably with B . However, the average energies of the two distributions still tend to follow the parabolic B dependence as is apparent from the graph. Thus, for extremely large fields, the localization would be so strong that the bond length will go below the average vacancy-vacancy distance, and the vacancies would no longer “see” each other. All these separate DOS

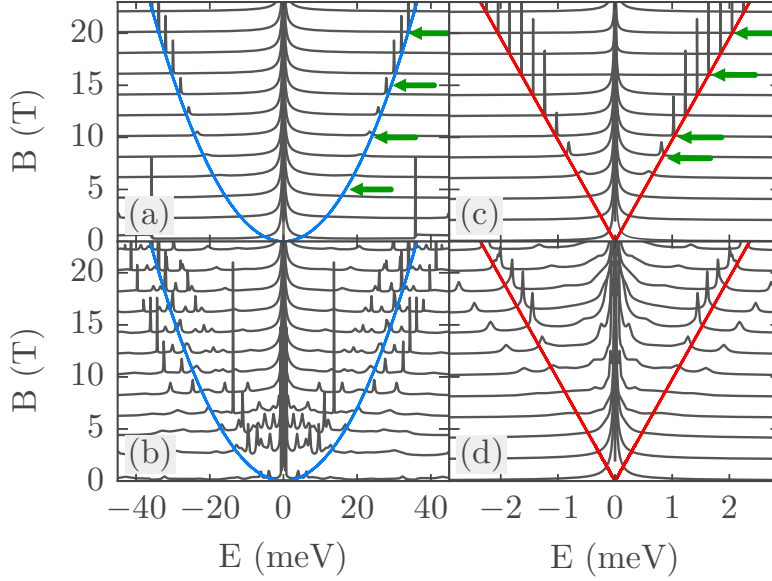


Figure 5.9: DOS for different values of magnetic field and different disorder distributions: (a) $n = 0.001\%$ SV distribution, (b) $n = 0.005\%$ SV distribution, (c) single divacancy located at the center of the system, (d) $n = 0.01\%$ DV distribution. The two distributions of monovacancies are the same as those used in Figs. 5.8(a) and 5.8(b), respectively. In all four cases $T = 0$ K. The green arrows mark (E, B) points at which we study LDOS in Figs. 5.10, 5.11, and 5.13.

peaks would then converge to a single energy—equal to that of an isolated monovacancy.

Scaling of the localization energy with magnetic field is different for divacancies. As Figs. 5.9(c) and 5.9(d) show, the localization energy for divacancies scales linearly with the magnetic field. The red lines in these two figures mark the linear dependence $B = \beta E$, where $\beta \approx 9700$ T/eV. Contrary to monovacancies, where the bond states evolve rather unpredictably with magnetic field, the bond states of divacancies evolve very predictably with the field. The two DOS peaks at positive energies, and the two peaks at negative energies in Fig. 5.9(d), move proportionally to the magnetic field. There are no additional peaks which would correspond to different bonding of divacancies. These results suggest that bonding of divacancies is weaker when compared to monovacancies. One of the possible reasons for this weaker

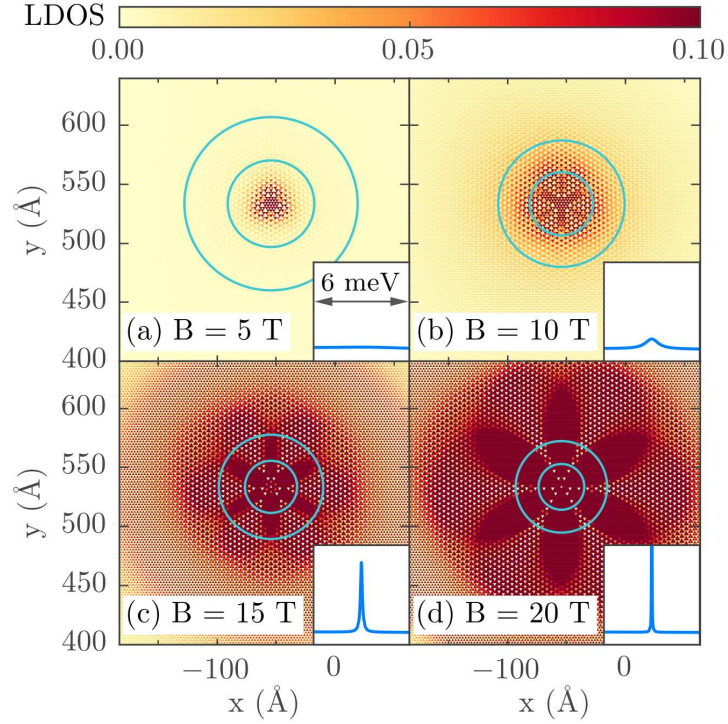


Figure 5.10: The evolution of LDOS around a single monovacancy. The magnetic field strengths are 5 T, 10 T, 15 T, and 20 T. The two circles mark radii R_c , and $2R_c$. Insets in the lower-right corners show the total DOS in a 6 meV energy range around the localization energy.

bonding might be the constant localization length for divacancies, which we discuss below.

Reference [88] also studied the $E(B)$ dependence of the new (localized) states, and for both mono- and divacancies found it to be neither linear, nor parabolic. However, the lowest field considered in that reference (beside $B = 0$ T) was around 300 T, therefore our results can be understood as a low field limit of those presented in Ref. [88].

As we stated previously, the localization radius for monovacancies r_L is inversely proportional to the square root of the magnetic field. It is also proportional to the cyclotron radius $r_L \sim R_c = E/(ev_F B)$, and since $E \sim \sqrt{B}$, then $r_L \sim 1/\sqrt{B}$. To demonstrate this, in Fig. 5.10 we follow how LDOS around an isolated monovacancy evolves as we increase the magnetic field. In other words, we follow the localized state along the αE^2 parabola in Fig. 5.9(a). The two circles in each inset in Fig. 5.10 have radii R_c and $2R_c$, and they

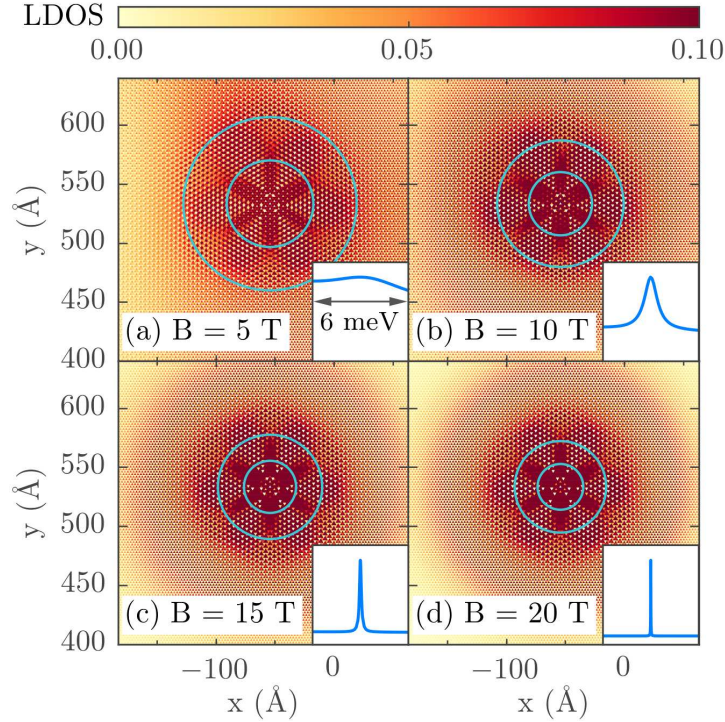


Figure 5.11: Same as Fig. 5.10 but now showing normalized LDOS, where LDOS in each subplot is divided by a maximum LDOS value for that subplot. The lower-right insets (showing the total DOS around the energy of a localized state) are also scaled, so that the DOS peak maximum is equal to one.

are centered on the vacancy site. The corresponding energies and cyclotron radii are: $E = 16$ meV, $R_c = 36.7$ Å (a), $E = 23.4$ meV, $R_c = 26.8$ Å (b), $E = 29$ meV, $R_c = 22.1$ Å (c), and $E = 33.9$ meV, $R_c = 19.4$ Å (d).

A first look at Fig. 5.10 suggests that localization radius is not proportional to the cyclotron radius R_c . While R_c decreases with rising magnetic field, the localization radius appears to increase and LDOS forms intricate flower-like patterns. The answer to this contradiction lies in the lower-right insets in Fig. 5.10, which show the total DOS around the localization energy. For stronger fields the localized state is better defined in energy, therefore the total DOS is larger. In order to properly compare these four cases, we need to normalize the LDOS in each subplot. This is done in Fig. 5.11, where each LDOS distribution is divided by its maximal value. With these normalized results the localization radius scales proportionally to the cyclotron radius

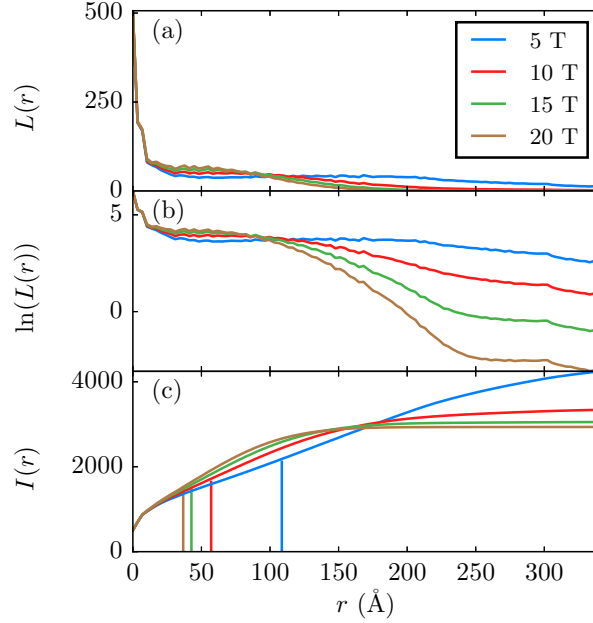


Figure 5.12: (a) Radial distribution $L(r)$ of DOS around a single monovacancy shown in Fig. 5.11, for the same values of E_F and B . For each r , the distribution is obtained by integrating LDOS in circular region of radius r and width Δr , $L(r) = \int_0^{2\pi} \int_r^{r+\Delta r} LDOS(r', \varphi) d\varphi dr'$. (b) Logarithm of $L(r)$. (c) Sum of the radial distribution $I(r) = \int_0^r L(r') dr'$ showing radial distance (vertical lines) for which the given distribution reaches half of its maximal height.

R_c , as is intuitively expected. The scaled results also point to another interesting feature. We stated earlier that the LDOS around a monovacancy is localized mostly on one sublattice—opposite to that of the vacancy. However, the scaled results show that at the localization energy, LDOS around a monovacancy spreads over both sublattices. Nonzero LDOS on the vacancy sublattice is located mostly in the symmetric—flower-like area. Outside of this area, states are still localized only on one sublattice. LDOS is also C_{3v} symmetric, which can be connected with the underlying C_{3v} (structural) lattice symmetry.

Another way to look at results presented in Fig. 5.10 and 5.11 is to plot the radial distribution of DOS around a single monovacancy. We show this distribution in Fig. 5.12. The high concentration of LDOS close to the vacancy, and the dependence of $L(r)$ on the width of a circular region over

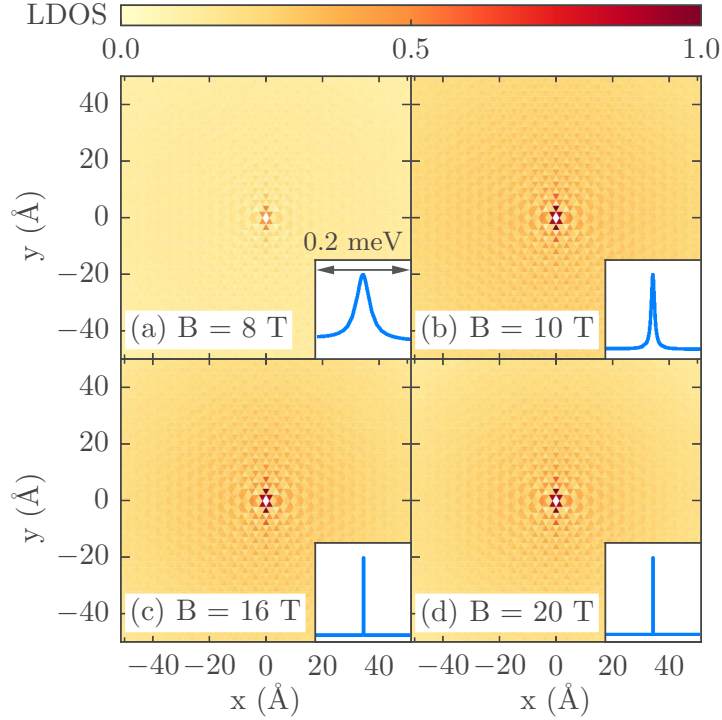


Figure 5.13: Same as Fig. 5.11 but now showing normalized LDOS and DOS for a single divacancy located at the center of the system. The (E, B) points at which we calculated LDOS and DOS are marked with green arrows in Fig. 5.9(c).

which we perform the angular integration for each r , presents an obstacle to accurately determine the half-width of these distributions. Another approach, which does not depend on the details of angular integration, is to calculate the radial integral $I(r)$ and to determine the distance at which this integral reaches one half of its maximal (saturated) value. These distances are presented as vertical lines in Fig. 5.12(c), and they are proportional to R_c (their values are 108 Å, 57 Å, 42.7 Å, and 36.7 Å, respectively).

A similar LDOS comparison as in Fig. 5.10, but for an isolated divacancy, is presented in Fig. 5.13. Contrary to monovacancies, a divacancy localization length does not change significantly with magnetic field. This can be understood just based on the linear $E(B)$ dependence of the divacancy localization energy. If we assume that localization length is still proportional to the cyclotron radius, then since $E = B/\beta$, it follows that $r_L \sim R_c = E/(ev_F B) = 1/(\beta ev_F)$. The LDOS around a divacancy is C_{2v}

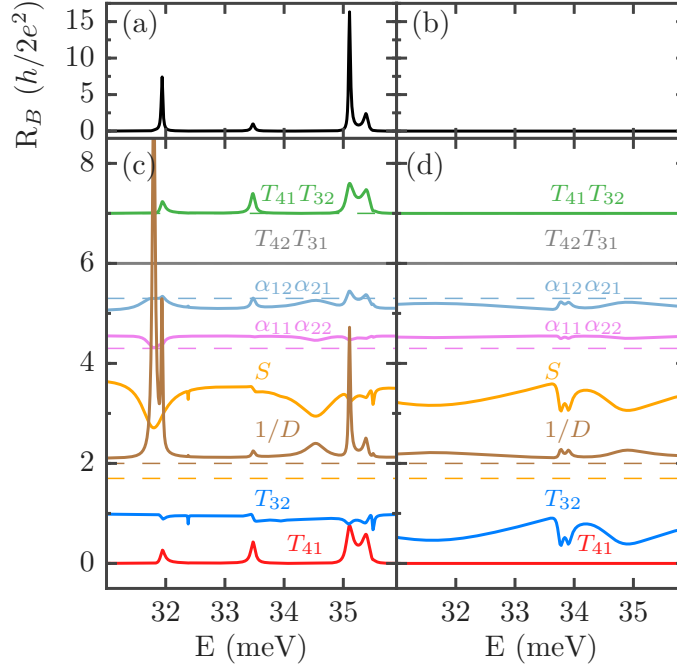


Figure 5.14: Decomposition of the bend resistance $R_B = (T_{41}T_{32} - T_{42}T_{31})/D$, where $D = (\alpha_{11}\alpha_{22} - \alpha_{12}\alpha_{21})S$. Results for two SV distributions ($n = 0.01\%$) in (a) and (b) are decomposed in (c) and (d), respectively. Most of the terms in (c) and (d) are vertically displaced, with dashed lines marking the corresponding positions of the zero axes. Magnetic field is $B = 20$ T, and $T = 0$ K.

symmetric, which is also related with the underlying lattice symmetry. Contrary to monovacancies, divacancies preserve the sublattice symmetry, and this is the origin of the different behaviour of these two disorder types.

5.3.4 Decomposition of R_B and the current density

When discussing results for the averaged bend resistances \bar{R}_B in 5.3.1, we mentioned that although the averaged results appear to be symmetric for electrons and holes, the results for individual distributions are not, and for some distributions there are no new peaks in R_B . In this subsection we study why this is the case. We compare bend resistances for two specific monovacancy distributions: one for which there are new peaks in R_B , and one

for which there are not. In order to understand how these peaks come into existence from the different transmission terms in the S matrix, we decompose R_B on its constituent parts according to the Landauer-Büttiker (LB) formula [86]. Results are presented in Fig. 5.14. Here we focus only on a narrow energy range where new peaks in R_B appear. Analysis of the main LB terms in Fig. 5.14(c) reveals that only one term ($T_{41}T_{32}$, green curve) is responsible for the appearance of the R_B peaks. The other term in the numerator ($T_{42}T_{31}$, gray line) is always equal to zero. A further decomposition of the first term ($T_{41}T_{32}$, green curve) shows that one transmission function (T_{32} , blue curve) is very close to unity, and that only T_{41} (red curve) dictates where a new R_B peak appears. Only when this transmission (T_{41}) is nonzero, we have peaks in R_B . Therefore (to a first approximation) we can say that R_B is proportional to modulated T_{41} . One might argue that T_{32} is also important, but since B is perpendicular, T_{32} will always be close to unity in this energy range, because of the edge states that go from the second to the third lead. This R_B - T_{41} connection is also confirmed in Figs 5.14(b) and 5.14(d), where both main LB terms in the numerator are equal to zero as well as T_{41} , and thus R_B is also equal to zero.

The only way to understand why for some vacancy distributions the particular T_{41} transmission is equal to zero, and for some it is not, is to investigate how electron current flows in the presence of vacancy disorder. This is presented in Fig. 5.15 for the same two SV distributions as those used in Fig. 5.14. In a clean system without vacancies, and with a perpendicular magnetic field, all current from the first lead would go to the second lead because of the current carrying edge states. This is mostly what we see in both cases (Figs. 5.15(a) and 5.15(b)) where T_{21} term is the most dominant when compared with the other transmission functions. This is also visible in Fig. 5.15(c), where most of the current from the first lead travels to the second lead along the edges. The two vacancy distributions differ in the way they scatter this edge current from the first to the second lead. The first distribution (Fig 5.15(a)) is causing more backscattering (T_{11}), and scattering to the fourth lead (T_{41}), whereas the second distribution is causing more scattering to the third lead (T_{31} in Fig 5.15(b)). Where this edge current is diverted depends mostly on a particular arrangement of vacancies, since current flow is pinned by the vacancies. For example, T_{41} (and consequently R_B) exhibits narrow peaks because of a particular arrangement of vacancies in the central part of the cross. As shown in Fig. 5.15(d), the current starts to flow around these vacancies, and it is diverted to the fourth lead. In a

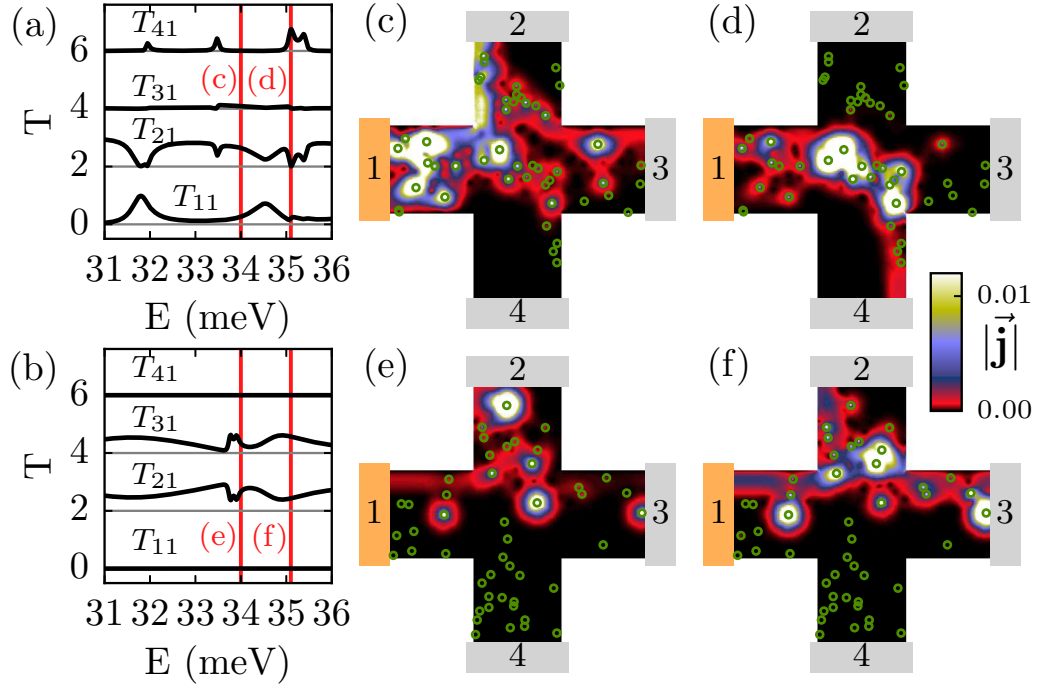


Figure 5.15: (a)-(b) Electron transmission functions from the first lead for two specific disorder distributions (the same two distributions as used in Figs. 5.14(a) and 5.14(b), respectively). The transmission functions are vertically displaced by $\Delta T = 2$ for clarity. (c)-(f) Current densities at energies marked in (a) and (b) by vertical red lines. Magnetic field is $B = 20$ T, and temperature is $T = 0$ K.

similar way, the current flow in Figs. 5.15(e) and 5.15(f) is also pinned by the vacancies and diverted to the third lead.

Reference [4] (and particularly Chapter IV in this reference) gives a valuable explanation of the QHE in terms of electron propagation along the sample edges. According to this reference, the rise of longitudinal resistance (for Fermi energies coinciding with the Landau levels) occurs due to the existence of states in the interior of the sample. These bulk states connect the otherwise separated edges channels, and give rise to their backscattering, and this backscattering manifests in a nonzero longitudinal resistance. The existence of vacancy localized states in our system, with energies in-between the Landau levels, leads to the expected LL broadening. Additionally, these vacancy states can provide a narrow pathway between the channels propa-

gating along the opposite edges of the system. In our particular setup, the nonzero T_{41} term is due to a backscattering between a channel going from the 1st to the 2nd lead (1→2), and the one going from the 3rd to the 4th lead (3→4). This edge state scattering is responsible for the nonzero bend resistance.

Similar analysis can also explain the asymmetry between the resistance results for electrons and holes (when the field direction is fixed). In a clean sample with no vacancies, $T_{21} = 1$ and $T_{41} = 0$ for electrons, while $T_{21} = 0$ and $T_{41} = 1$ for holes. Also $T_{32} = 1$ for electrons, while $T_{32} = 0$ for holes. We already showed that the first term in the Büttiker formula (term $T_{41}T_{32}$ in Eq. (5.7)) determines the bend resistance. For electrons this term depends mostly on T_{41} , since $T_{32} = 1$. For holes, on the other hand, it depends on T_{32} , since $T_{41} = 1$. Because $T_{32}(-E, B) \neq T_{41}(E, B)$, the bend resistance in a disordered system is not the same for electrons and holes. The bend resistance becomes equal only if we additionally change the magnetic field direction (from \mathbf{B} to $-\mathbf{B}$) when we switch from electrons to holes.

In summary, although the two new peaks in R_B should in general appear at the vacancy localization energy, they are very sensitive to a particular distribution of vacancies. The vacancies significantly disrupt and divert the current flow. However, if not in R_B , this current guiding will probably manifest itself in measurements of some other non-local resistance.

5.3.5 NNN interaction

In this section we study the effects of a nonzero hopping between the second nearest neighbours ($t' \neq 0$). Figure 5.16 shows the averaged results for the SV disorder type, for increasing value of the next-nearest neighbour (NNN) hopping. According to Pereira et al. (Refs. [79, 78]), for the $B = 0$ case, there are vacancy localized states even when $t' \neq 0$. Although NNN hopping breaks the electron-hole symmetry, the localized states are still preserved. Here, we study the non-zero magnetic field case, and we still observe localization peaks. Breaking of the e-h symmetry leads to a displacement of the two peaks, and this displacement (as we show in Fig. 5.16) depends linearly on the NNN hopping energy t' . One of the peaks moves toward the $n = -1$ Landau level, whereas the other moves to the zeroth Landau level. Although the two new peaks are clearly visible in the bend resistance, they are not so distinguishable in the DOS. DOS exhibits considerable broadening, and the two peaks are barely visible after temperature smoothing. A closer look

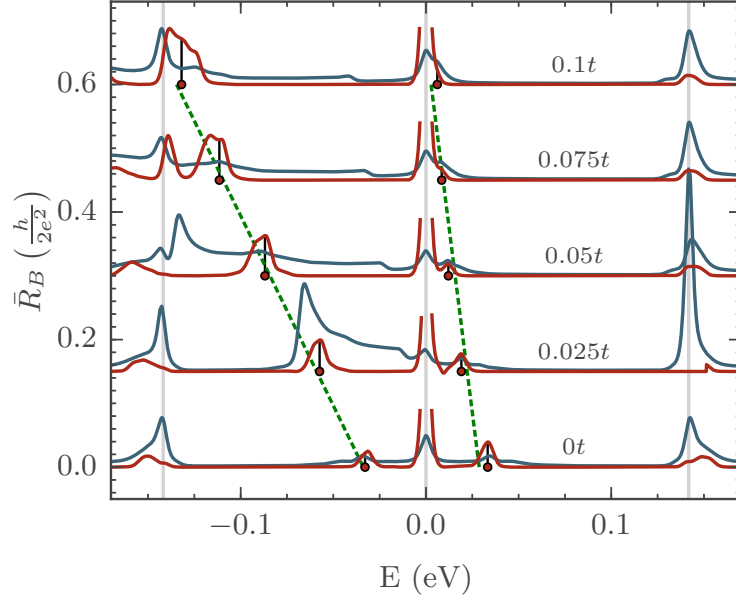


Figure 5.16: Smoothed and averaged bend resistances (\bar{R}_B , red curves), and total DOS (blue curves) for increasing value of the next-nearest neighbour hopping energy t' . All results are obtained for the SV disorder type ($n = 0.01\%$), for $N = 10$ different disorder distributions. Magnetic field is $B = 20$ T, and $T = 16$ K. Green, dashed lines are linear fits of the \bar{R}_B peak energy versus the NNN hopping energy t' . Results for $t' \neq 0$ are displaced horizontally by $\Delta E = -3|t'|$ in order to align the Landau levels. The R_B peaks at the zeroth Landau level are cut-off above $0.09 h/(2e^2)$ for clarity.

in the LDOS for $t' \neq 0$ (not shown) reveals a strong localization on the horizontal, zigzag edges. This edge localization causes this wide background in DOS and masks the narrow vacancy localization peaks.

The linear energy dependence of the new peaks can be further explained if compared with the zero field results of Ref. [78]. The introduction of a nonzero NNN hopping shifts the whole Landau spectrum by $\Delta E = 3|t'|$. According to Ref. [78], the shift of the *zero mode* is less than ΔE , and proportional to t' . If we assume the two localized states that we obtain originate from this shifted zero mode, than we expect them to also shift linearly and follow the zero mode. On the other hand, the two linear coefficients in Fig. 5.16 are different (the distance between the peaks increases with t'). If we assume the parabolic $E(B)$ dependence is preserved, than we can conclude that t'

also modifies the scaling coefficient α , which is then a linear function of t' .

5.4 Conclusions

In this chapter we studied electron transport in graphene Hall bars in quantizing magnetic fields in the presence of three different types of vacancy disorder. All three types of vacancy disorder induce new states in the relativistic Landau spectrum, but these states behave differently depending on the disorder type. The new states localized around monovacancies, are indirectly observable in the bend resistance and in the total DOS, but only for vacancy concentrations below a critical concentration. These states are localized mostly only on one sublattice, but at the localization energy they spread on both sublattices in C_{3v} symmetric, flower-like patterns.

Another interesting feature is different behaviour of the two monovacancy distribution types. SVA disorder, although inducing approximately equal number of states as SV disorder (compare DOSs in Fig. 5.6 for these two disorder types for $n = 0.01\%$) creates considerably different results in the bend resistance. The origin of these differences is not known and requires further study. We speculate that these differences might come from different current flow patterns around different types of vacancy pairs. For example, Ref. [88] showed that vacancy coupling does not depend on their type, however, we showed that these states have a certain symmetry, therefore the coupling strength will also depend on direction, and not only on distance. Divacancies also cause localization, but for fields that we consider, their localization energies are much closer to those of the relativistic LLs, which makes them harder to observe experimentally. Since they do not break the sublattice symmetry, they are usually C_{2v} symmetric, and they have a constant localization length.

Depending on the ratio between the average vacancy-vacancy distance (which depends on the vacancy concentration) and the field strength, localized states around several monovacancies can bond together—forming localized bond states. These bond states have a localization energy different from that of an isolated monovacancy, but on average they spread equally around this energy. The localization energy around a single monovacancy is proportional to the square root of the magnetic field, while the localization radius (and consequently the possible radius of the bond states) scales with the cyclotron radius. The behaviour of divacancies is different. Their localization energy scales linearly with the field, and their localization length

5.4. Conclusions

is independent of the field. Based on this, whether they form bond states depends solely on their mutual distance, and not on the field strength.

A decomposition of the bend resistance reveals that only one transmission function (T_{41}) is responsible for the appearance of additional peaks in R_B , which we additionally connect with the vacancy guided current flow inside the system. All these results are slightly modified when a next-nearest neighbor interaction is included, and the symmetry between electrons and holes is broken.

CHAPTER 6

Electron guiding in graphene

6.1 Introduction

In this chapter* we investigate electron guiding in graphene in high magnetic fields. Quantum Hall measurements^{67,68} in graphene⁴⁷ revealed the relativistic nature of its charge carriers and its gapless spectrum. Long before the discovery of graphene, it was known that carriers in a conventional two-dimensional electron gas (2DEG) tend to move along snake like paths when exposed to inhomogeneous magnetic fields, the so called *snake states*.^{89,90} Similar effects were explored even earlier in the studies of electron propagation on the boundary of magnetic domains in metallic systems.^{91,92,93,94} Experiments in non-planar 2DEG⁹⁵ and in systems with a ferromagnetic stripe⁹⁶ indirectly measured the effects of snake states on the longitudinal and the Hall resistance. In graphene, theoretical predictions of snake-states⁹⁷ were quickly followed by experiments confirming their existence.⁹⁸ Snake states in a Hall bar were previously studied in Ref. [99] using a classical billiard model. A top-gate was used to create a *pn*-junction along the main diagonal of the Hall cross, and oscillations of the bend resistance were connected with electron guiding along the snake-like paths at the *pn*-interface. Two very re-

*Results presented in this chapter are based on our publication: M. D. Petrović, F. M. Peeters, *Quantum transport in graphene Hall bars: Effects of side gates*, Solid State Commun. **257** 20–26 (2017).

cent studies^{100,101} on graphene Josephson junctions reported electron guiding near nanoribbon edges due to an edge potential. This guiding was visible in the local current density, which was obtained using Fourier methods.

In this chapter we study quantum transport of electrons in graphene Hall bars surrounded with four side-gates (see Fig. 6.1). This chapter combines the side-gate potential (introduced in Chapter 4) with the high magnetic fields (introduced in the previous chapter), and shows that this combination leads to interesting effects such as electron guiding. The gates modify the local electron density on the edges of the Hall bar, and induce a local electric potential. If the system is placed in an external magnetic field, this edge potential guides the charge carriers along specific equipotential lines. For weak fields, these states move along the previously mentioned snake-like paths, while for stronger fields, we prefer to call them guided states. Our main goal in this chapter is to understand how this guiding occurs locally, and which paths electrons take in the system. Our second goal is to predict measurable effects of this guiding. We start by investigating how side-gate potential modifies the electron dispersion relation in each lead. By studying the current density profiles of the incoming and outgoing states in two representative leads, we are able to build a physical picture of electron transport in this inhomogeneous system. This picture, in combination with the Landauer-Büttiker formalism, allows to analytically predict the quantization of the bend and Hall resistances. The quantized resistance values match the ones that we obtain with our numerical (tight-binding) method. Although we choose one specific potential configuration, with asymmetrically biased side-gates, our results are equally extendable to other gate configurations, and possibly even to other geometries.

This chapter is organized as follows: In Section 6.2 we describe our system and we briefly repeat discussion on our numerical methods. Section 6.3 is divided in four parts. In the first part (6.3.1) we analyze the dispersion relations of the leads, and in the second (6.3.2) we show how guided states look in real space. A scheme for electron guiding is presented in the third part (6.3.3), and we use this scheme to analytically calculate the bend and the Hall resistances in the last subsection (6.3.4). Our conclusions are given at the end of the chapter, in Sec. 6.4.

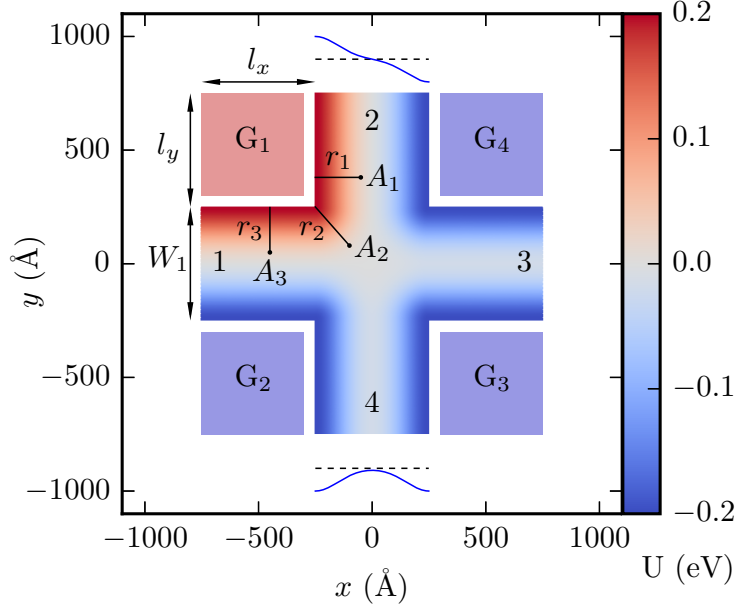


Figure 6.1: Side-gated Hall bar system: four leads are marked with numbers, and they all have approximately equal widths ($W_1 = W_3 = 49.71$ nm, and $W_2 = W_4 = 49.94$ nm, $l_x = l_y = 50$ nm). Horizontal leads have zigzag edges, while vertical leads have armchair edges. All dangling bonds are removed. Three lines r_1 , r_2 , and r_3 show the minimal distances from the system edge to three arbitrary points A_1 , A_2 , A_3 , respectively. These distances are used in Eq. (6.1) to calculate the gate potential of the 1st lead at the corresponding points A_1 , A_2 , and A_3 . The potential profiles inside the leads are depicted by the blue curves above the 2nd and below the 4th lead (black dashed lines mark the position of the zero potential).

6.2 System and Methods

The studied system is shown in Fig. 6.1, it is a graphene cross with four side gates (G_1 , G_2 , G_3 , G_4) placed between four orthogonal leads. When biased, the gates create a local potential at the system edges which decreases towards the interior of the system. We model the potential of a single side gate by a Gaussian function

$$U_g(r_n) = U_0 \exp(-r_n^2/2\sigma^2), \quad (6.1)$$

where r_n is the minimal distance from the present point to the system edge (see Fig. 6.1). Potential width σ is set to 10 nm, so that potentials of neighbouring gates do not overlap. We use G_1 as a reference gate, and set po-

tentials of other gates (G_2 , G_3 , and G_4) opposite to that of G_1 , as shown in Fig. 6.1.

As explained in previous chapters, for our numerical calculations we use KWANT.²⁷ We already explained previously how we model the graphene TB Hamiltonian, therefore we do not repeat that explanation here. We would just point out that the hopping term $\tilde{t}_{ij} = te^{i\varphi_{ij}}$ is defined using the electron hopping energy $t = -2.7$ eV, and the Peierls phase factor

$$\varphi_{ij} = \frac{e}{\hbar} \int_{\mathbf{r}_j}^{\mathbf{r}_i} \mathbf{A}(\mathbf{r}) \cdot d\mathbf{r}, \quad (6.2)$$

where $\mathbf{A}(\mathbf{r})$ is the vector potential. The vector potential in the horizontal leads is set using the Landau gauge $\mathbf{A}_H = -By\mathbf{e}_x$, and that in the vertical leads is $\mathbf{A}_V = Bx\mathbf{e}_y$. These two potentials are smoothly connected in the main scattering region using the procedure described in the previous chapter (see also Refs. [84, 85]).

6.3 Results

6.3.1 Dispersion relations

First we study the dispersion relations (presented in Fig. 6.2) of the side-gated graphene leads. We compare three cases with different combinations of side-gate potential and magnetic field. The dispersion relations are obtained by considering semi-infinite graphene nanoribbons with the same transversal potential profile as potentials presented in Fig. 6.1. Dispersion relations of clean nanoribbons (without magnetic field or external potential) were extensively studied in Refs. [57, 58], and therefore we do not present them here. Dispersions for a nonzero potential ($U_0 = 100$ meV) are shown in the first row in Fig. 6.2. In Chapter 4 we investigated dispersions of symmetrically gated leads using the same Gaussian potential as given by Eq. (6.1). Here, for zigzag leads, we focus on a narrow wave-vector range in close proximity of the two valleys (K and K'). The edge potential in zigzag leads determines the energy of dispersionless bands. In case of a symmetric potential, as in the 3rd lead, dispersionless bands shift in energy to a value of $-U_0$. On the other hand, in asymmetrically gated 1st lead, the side-gates open a small energy gap between the two flat bands. The gap energy is determined by the lead width. Asymmetric potential in the 2nd (armchair) lead preserves the electron-hole symmetry, while symmetric potential in the 4th lead moves the Dirac point towards the negative energies.

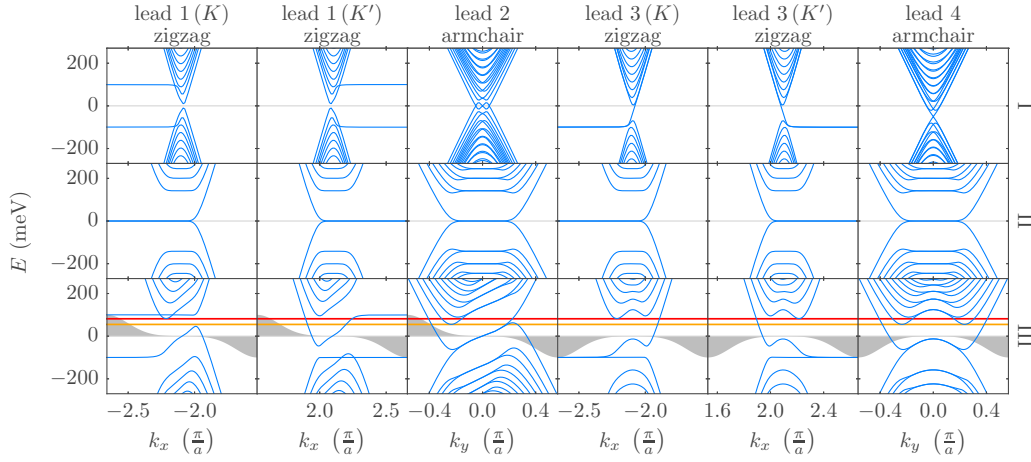


Figure 6.2: Lead dispersion relations (columns) for different combinations of magnetic field and side-gate potential (rows): $B = 0$ T, $U_0 = 100$ meV (case I, first row), $B = 20$ T, $U_0 = 0$ meV (case II, second row), and $B = 20$ T, $U_0 = 100$ meV (case III, third row). Gray horizontal lines mark the zero energy, while gray areas in the third row show the lead potential profile along the positive x and y directions. Since KWANT produces dispersions along the lead direction, we inverted the dispersions of the first and the fourth lead, because they point in negative x and y directions. The red line in the third row marks the minimal energy of the first band in the zigzag leads—compare it with the minimal energy of the first band in the armchair leads (orange line).

Results for a nonzero magnetic field (second row in Fig. 6.2) were explained in Ref. [102]. In this case, both armchair and zigzag leads show dispersionless surface states, appearing exactly at the energy of Landau levels (LLs). In this regime, graphene exhibits specific quantization of the Hall resistance, as was measured in Refs. [67, 68].

The most relevant case for us is when both magnetic field and side-gate potential are present in the system (third row in Fig. 6.2). First noticeable difference introduced by the side-gates is twisting of the otherwise flat bands of the surface states (compare the second and the third row in Fig. 6.2). As a consequence of this twisting, surface states become dispersed and new states appear in the bulk. As we show below new states appear only in specific areas of the sample. In general, symmetry of the lead potential is reflected in the lead dispersion. We plot potential profile of each lead in the third row of Fig. 6.2 (gray areas) to show this connection. Asymmetrically gated

leads (the 1st and the 2nd lead) have asymmetric dispersions, while symmetrically gated leads (the 3rd and the 4th lead) have symmetric dispersions. For symmetrically gated leads this connection can be explained in the following way: suppose we are interested in how the dispersion relation changes when, instead along the lead, we look in the opposite direction (towards the system). To do this we have to invert the potential profile relative to the middle line of the lead. In the inverse space (the space of wave vectors k) this view change is equivalent to inverting the dispersion relative to the $k = 0$ axis (all k values go to $-k$, and the opposite). If the lead potential is symmetric, then this change of view has no effect. We would obtain the same potential and the same dispersion relation. In other words, the inverted dispersion is equal to the initial one $E_n(-k) = E_n(k)$. This is the case with the 3rd and the 4th lead.

For asymmetrically gated leads this connection between the lead potential and the dispersion is not so straightforward. If the magnetic field is sufficiently strong, states moving along the opposite edges are completely separated. These edge states on the opposite edges then feel different potentials. For example, when there is no edge potential, electrons in the 2nd lead with positive velocity (and positive k) move along the left edge, while electrons with negative velocity (and negative k), move along the right edge. For holes, states with positive k (and negative velocities) move along the left edge, while states with negative k (and positive velocities) move along the right edge. From this we see that states with positive k always move along the left edge, while states with negative k always move along the right edge. Therefore, if we apply a potential on the left edge, it will only affect states with positive k , while if we apply a potential only on the right edge, it will only influence states with negative k . Assuming that an electron state with positive k is shifted in energy (due to the side gate potential) by some value ΔE , then electrons with negative k are shifted by $-\Delta E$, as well as hole states with the same negative k . From here, we see that the dispersion is asymmetric $E_n(k) = -E_{-n}(-k)$. This explanation is similar to the one given in Chapter 4 in Ref. [4].

Before we proceed to the next part, we would like to stress one very important difference between armchair and zigzag leads. Although the minimal band energies appear to be similar for all leads, they are not precisely equal. The minimal band energy in armchair leads is slightly smaller than in the zigzag leads. The red and orange lines in the last row in Fig. 6.2 show this small misalignment. This difference introduces additional complexity in the

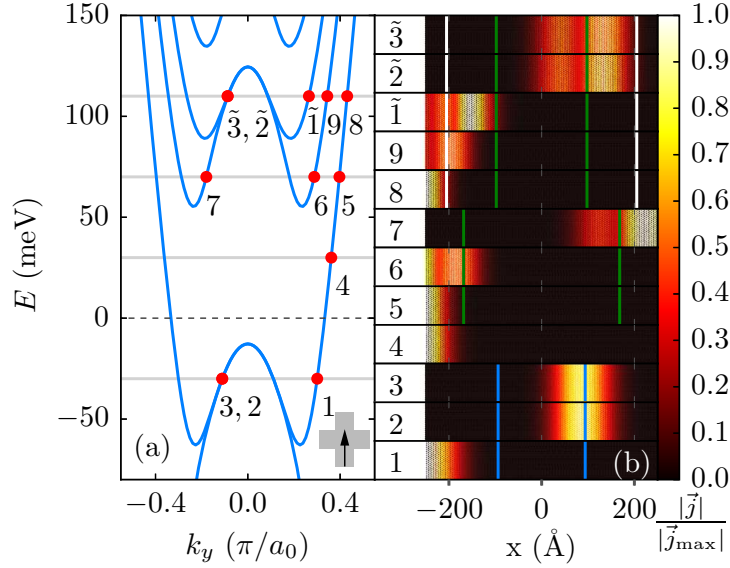


Figure 6.3: (a) Dispersion relation of the symmetrically gated 4th lead. (b) Normalized current density across the lead for incoming modes marked with red circles in (a). Figure (b) is divided vertically (1– $\tilde{3}$), with each inset corresponding to one state marked in (a). The considered Fermi energies are $E_F = -30, 30, 70,$ and 110 meV (horizontal gray lines in (a)). The blue lines in (1– $\tilde{3}$) mark the equipotential lines where $E_F - U_0 = E_{LL=0}$. Similarly, green and white lines mark the positions where previous difference is $E_{LL=1}$, and $E_{LL=2}$, respectively. Magnetic field is $B = 20$ T and $U_0 = 100$ meV. The direction of the modes and the considered lead are sketched in the lower right corner in (a).

system, since a new mode can open in one lead, but electrons can not travel to the neighbouring lead, since there are no open states there. Further below, we explain the importance of this misalignment in more detail.

6.3.2 Incoming and outgoing modes

To better understand the motion of charged particles in the system, here we analyze the incoming and outgoing modes of two representative leads: one with symmetric (the 4th lead), and one with asymmetric (the 2nd lead) side-gate potential. We focus on studying the evolution of current profile in each lead with increasing Fermi energy.

In Fig. 6.3(b), we present the current density profiles (insets from 1 to $\tilde{3}$ on

the right side of Fig. 6.3) for the incoming modes (red circles in Fig. 6.3(a)). As we previously mentioned, because of the potential symmetry, the dispersion relation is also symmetric. Therefore the current density profiles for the outgoing modes can be obtained by inverting the profiles shown in Fig. 6.3 along the middle line of the lead ($x = 0$). We can differentiate two groups of incoming states in Figs. 6.3(a) and 6.3(b): (1) the normal edge states (e.g. states 1, 4, and 9), and (2) the guided states (e.g. states $\tilde{2}$, and $\tilde{3}$) which move along specific equipotential lines. Electron kinetic energy along these equipotential lines matches the energy of Landau levels $E_F - U(x, y) = E_{LL}$. For symmetric potential two of these equipotential lines appear on the system edges for each new LL, and with increasing Fermi energy these lines move towards the middle of the lead ($x = 0$). If the applied potential is larger than the energy difference between two neighbouring LLs, then a pair of these equipotential lines appear simultaneously for each LL. For example, in Fig. 6.3 the energy difference between the 1st LL and the 2nd LL is smaller than the applied side-gate potential, and equipotential lines for the 1st and the 2nd LL coexist at higher Fermi energies (green and white lines in insets 8– $\tilde{3}$ in Fig. 6.3(b)). Although it looks like some of the states on the left edge (states 8, 9, and $\tilde{1}$ in Fig. 6.3(b)) are guided along the left white line, note that guided states for the white lines appear only at higher energies (not considered here). In analogy with the guided states for the zeroth Landau level (states 2 and 3), and with the first Landau level (states $\tilde{2}$ and $\tilde{3}$), guided states for the second Landau level should appear along the right white line. Because of the symmetry of the side-gate potential, these equipotential lines always appear in pairs: the line on the right side corresponds to guided electrons coming out of the lead (incoming states), while the line on the left corresponds to guided electrons coming into the lead (outgoing states). Each of these lines can accommodate two states coming from different valleys (in armchair leads this is not so obvious, because there are no separate valleys, but in zigzag leads each guided state can be connected with a specific valley). For the zeroth LL, the guided states are always centered on the equipotential line (states going along the blue lines in insets 2, and 3 in Fig. 6.3(b)), while for higher LLs there is significant broadening of the guided states (states going along the green lines in insets $\tilde{2}$, and $\tilde{3}$ in Fig. 6.3(b)). Similar behaviour was reported in Ref. [103].

The asymmetric potential case is presented in Figs. 6.4, and 6.5. Here, because of the asymmetry, the outgoing modes are not equivalent to the incoming ones, hence it is necessary to study them separately. In contrast to

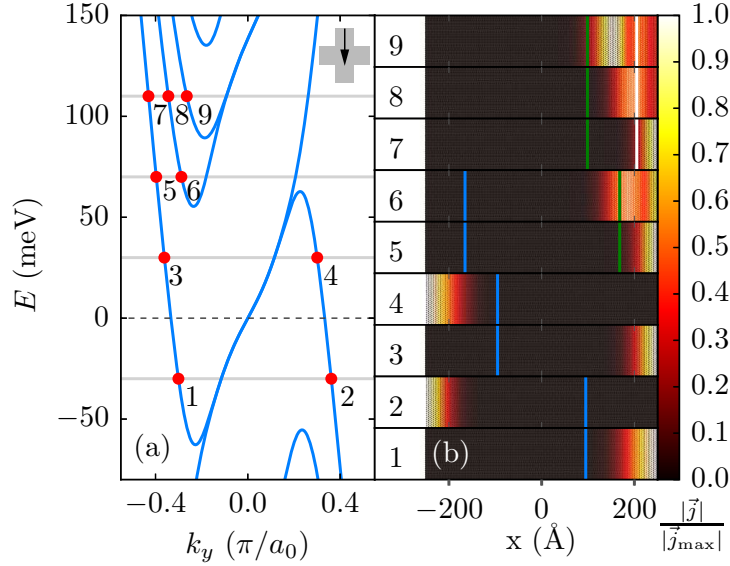


Figure 6.4: Same as Fig. 6.3, but now for incoming modes from the 2nd (asymmetrically gated) lead. Magnetic field is $B = 20$ T and $U_0 = 100$ meV.

symmetrically gated leads, here for each LL there is only one equipotential line satisfying the condition $E_F - U_0 = E_{LL}$. For each new LL this line appears on the right edge and moves towards the left edge as we increase the Fermi energy (see the blue lines in insets 1–6 in Fig. 6.4(b)). For the zeroth LL, these blue lines mark the separation point between electron and hole states (a pn border). For higher Fermi energies ($E_F = 70$, and 110 meV), the hole edge state on the left side disappears, and as we see below, it is replaced with an electron edge state moving in the opposite direction. Although there are no guided states among the incoming modes in Fig. 6.4, they appear among the outgoing modes in Fig. 6.5. The electrons are guided along the equipotential lines of the zeroth and the first LL, similarly as in the symmetric potential case (for example, compare insets 1, 2, 5, 7, and 8 in Fig. 6.5(b), with insets 2, 3, 7, $\tilde{2}$, and $\tilde{3}$ in Fig. 6.3(b)).

Although we only considered current profiles of the armchair leads, the corresponding incoming and outgoing modes in the (horizontal) zigzag leads are very similar. The only difference is that in zigzag leads each guided state can be connected with one of the valleys. The opening and closing of modes in neighbouring leads do not occur at the same energy because of a small subband misalignment mentioned above. There are situations where only one

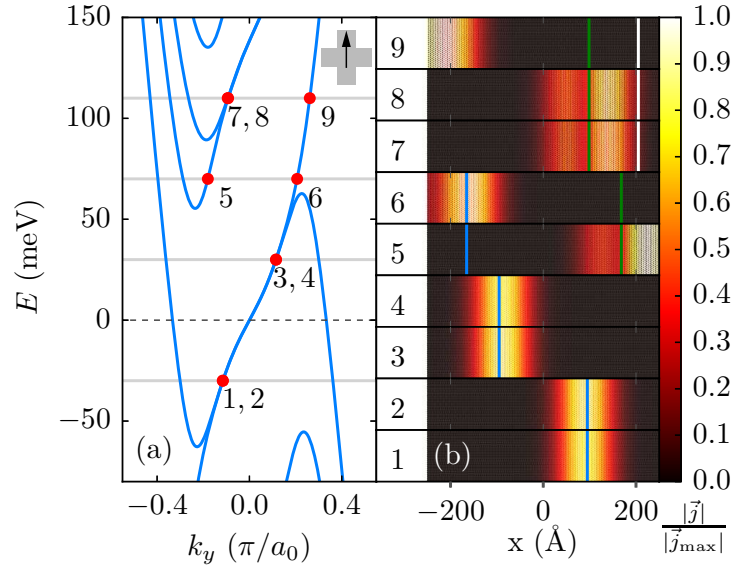


Figure 6.5: Same as Figs. 6.3, and 6.4, but now for outgoing modes in the 2nd lead. Magnetic field is $B = 20$ T and $U_0 = 100$ meV.

of the two guided states passes to the neighbouring lead, while the other are scattered backwards, because there are no open modes in the neighbouring lead.

6.3.3 Current guiding

The analysis of incoming and outgoing modes allows us to construct a picture of electron transport in this system. By extending previous results from the vertical (armchair) leads to the horizontal (zigzag) leads, in Fig. 6.6 we present a constructed scheme for electron guiding.

At the lowest energy ($E_F = -30$ meV, Fig. 6.6(a)), for each edge state on the negatively biased edges, there is a pair of guided states moving in the opposite direction. The guided states move along the pn -interface (the blue lines). Although there is only one pn -interface line with two identical guided states on it, here we show two separate blue curves in Fig. 6.6(a) to emphasize that there are two guided states. The position of these lines in the scheme do not match the actual position of the pn -interface. As the Fermi energy increases, the pn -interface shifts towards the central lines of the cross, and for positive Fermi energies, the pn -interface moves to the upper-left part

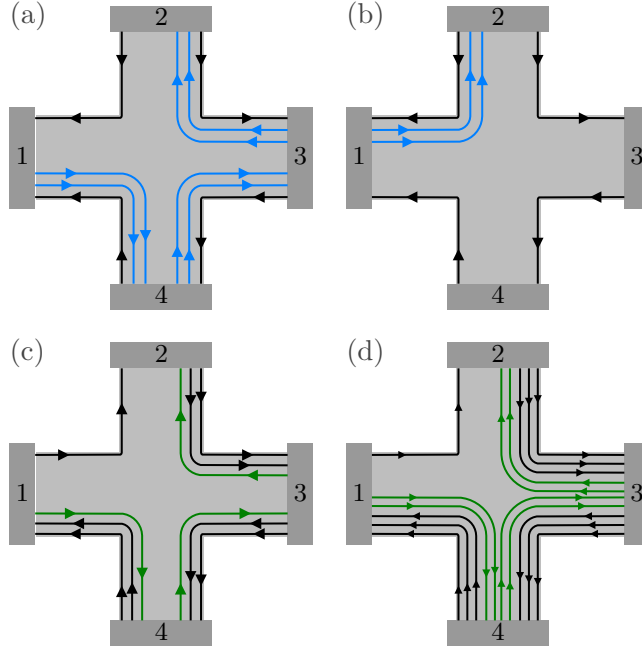


Figure 6.6: Scheme of the guided states (colored lines) and the edge states (black lines). The corresponding energies are similar to those used in Figs. 6.3, 6.4, and 6.5: (a) $E_F = -30$ meV, (b) $E_F = 30$ meV, (c) $E_F = 82$ meV, and (d) $E_F = 110$ meV. The magnetic field is $B = 20$ T, and the side-gate potential height is $U_0 = 100$ meV. Blue curves mark the guided states of the zeroth LL, while green curves mark the guided states of the first LL. The presented curves do not fully represent the actual current paths (they are separated from each other for better visualisation).

of the system. This is what we see in Fig. 6.6(b), for $E_F = 30$ meV. The two guided states are close to the hole state on the upper-left edge. For larger Fermi energies, the hole state on the upper-left edge disappears, and the pair of guided states turns into a single electron edge state, moving upwards along the upper-left edge (as in Fig 6.6(c)).

Due to the above mentioned mismatch of the band minimal energies in neighbouring leads, the case when Fermi energy is $E_F = 70$ meV is one of those situations where new modes open in the vertical (armchair) leads, but they backscatter due to the lack of open states in the horizontal (zigzag) leads. Therefore the scheme presented in Fig. 6.6(c) corresponds to larger energies (e.g $E_F = 82$ meV), when guided states open in all four leads. This

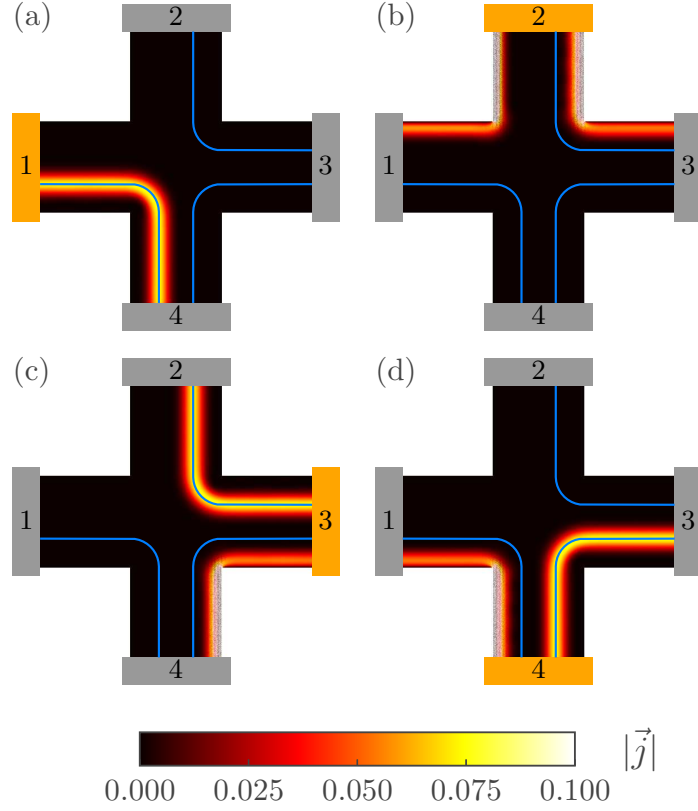


Figure 6.7: Current density for $E_F = -30$ meV, $B = 20$ T, and $U_0 = 100$ meV. Current is injected from the leads which are colored in orange. The blue lines are equipotential lines where $U(x, y) = E_F$.

situation is very similar to that presented in Fig. 6.6(a), except now there is only one guided state along the pn interface. As the Fermi energy further rises ($E_F = 110$ meV, Fig. 6.6(d)), a new edge state and a new guided state appear in the system.

The scheme presented in Fig. 6.6 can be generalized to higher LLs, assuming that the applied potential U_0 is smaller than the energy difference between the neighbouring LLs. For n -th LL ($n > 0$) on the negatively biased edges there will be $2n$ or $2n + 1$ edge states and one or two guided states, while on the positively biased edges there will be $2n - 1$ edge states. However for every U_0 , no matter how small it is, there will always be some minimal m for which all higher LLs ($m' > m$) are separated by an energy smaller than the applied potential. The present scheme is more complicated

for these higher LLs, because guided states from several LLs can coexist at the same Fermi energy. We do not consider these cases here.

To confirm the correctness of the scheme presented in Fig. 6.6, in Fig. 6.7 we show the current density profiles for all four leads at the Fermi energy $E_F = -30$ meV, as obtained from our numerical solution using KWANT. By combining all the currents presented in Fig. 6.7, we get the same picture as that presented in Fig. 6.6(a).

6.3.4 Bend and Hall resistances

Based on the pictures presented in Fig. 6.6, we are able to calculate the band resistance R_B by applying the Landauer-Büttiker formula. The most important property of the guided states is that they fully transmit without any backscattering. In that sense they are equivalent to edge states. As long as there is no backscattering the transmission coefficients are integers, and the transmission matrix is easy to write by hand by counting the incoming and outgoing modes.

To calculate the resistance we select one of the insets in Fig. 6.6—for example 6.6(d)—and write the current matrix

$$\begin{pmatrix} I_1 \\ I_3 \\ I_4 \end{pmatrix} = G_c \begin{pmatrix} 3 & 0 & -3 \\ 0 & 5 & -2 \\ -2 & -3 & 5 \end{pmatrix} \begin{pmatrix} V_1 \\ V_3 \\ V_4 \end{pmatrix}. \quad (6.3)$$

Here $G_c = 2e^2/h$ is the conductance quantum, and we choose $V_2 = 0$ (for details see Chapter 4 in Ref. [4]). We are only interested in the bend resistance

$$R_{12,34} = \frac{V_3 - V_4}{I_1}, \quad (6.4)$$

when current is passed from the first into the second lead (the currents are $(I_1 0 0)^T$). From the second row of Eq. (6.3) we obtain $V_3 = (2/5)V_4$, and from the third row we obtain

$$2V_1 = -3V_3 + 5V_4 = \frac{19}{5}V_4, \quad (6.5)$$

and therefore $V_1 = (19/10)V_4$. Substituting this back in the first row in Eq. (6.3), we obtain

$$\frac{1}{3} \frac{I_1}{G_c} = V_1 - V_4 = \frac{9}{10}V_4, \quad (6.6)$$

and therefore $V_4 = (10/27)I_1/G_c$, and $V_3 = (4/27)I_1/G_c$. Finally we can calculate the resistance as

$$\frac{V_4 - V_3}{I_1} = \frac{2}{9} \frac{1}{G_c}. \quad (6.7)$$

In a similar manner we can calculate the quantized resistances for the other situation depicted in Fig. 6.6. For Fig. 6.6(a) we obtain $R_B = (1/4)1/G_c$, and for Fig. 6.6(c) we also obtain $R_B = (1/4)1/G_c$. For Fig. 6.6(b) there is only one edge state connecting the 3rd and the 4th lead, therefore the potential on these two leads is equal ($R_B = 0$).

Previous calculations can be generalized for higher LLs. Assuming that applied potential U_0 is smaller than the separation between the neighbouring LLs, we can differentiate two cases. In the first case there is only one guided state open in each negatively biased lead (equivalent to Fig. 6.6(c)), while in the second case there are two such guided states (equivalent to Fig. 6.6(d)). In the first case the general current-voltage matrix relation

$$\begin{pmatrix} I_1 \\ I_3 \\ I_4 \end{pmatrix} = G_c \begin{pmatrix} 2n & 0 & -2n \\ 0 & 2n+1 & -1 \\ -1 & -2n & 2n+1 \end{pmatrix} \begin{pmatrix} V_1 \\ V_3 \\ V_4 \end{pmatrix}, \quad (6.8)$$

can be expressed in terms of LL index n . When solved this gives the quantized resistances

$$R_B = \frac{1}{4n^2} \frac{1}{G_c}. \quad (6.9)$$

For the second case, when both guided states are present in the system, the general Landauer-Büttiker matrix is

$$\begin{pmatrix} I_1 \\ I_3 \\ I_4 \end{pmatrix} = G_c \begin{pmatrix} 2n+1 & 0 & -2n-1 \\ 0 & 2n+3 & -2 \\ -2 & -2n-1 & 2n+3 \end{pmatrix} \begin{pmatrix} V_1 \\ V_3 \\ V_4 \end{pmatrix}, \quad (6.10)$$

which gives

$$R_B = \frac{2}{(2n+1)^2} \frac{1}{G_c}. \quad (6.11)$$

Comparison between numerical and analytical results is presented in Fig. 6.8. Quantized resistances obtained analytically agree well with the ones obtained numerically, at least for the first three Landau levels in Fig. 6.8(a). For higher Landau levels the match is not exact (see for example the line for $R_B = (2/49)1/G_c$ in Fig. 6.8(a)). We suspect the reason for this mismatch is a spatial widening of the guided states for higher LLs which leads to backscattering. A comparison with the band resistance obtained for higher field and

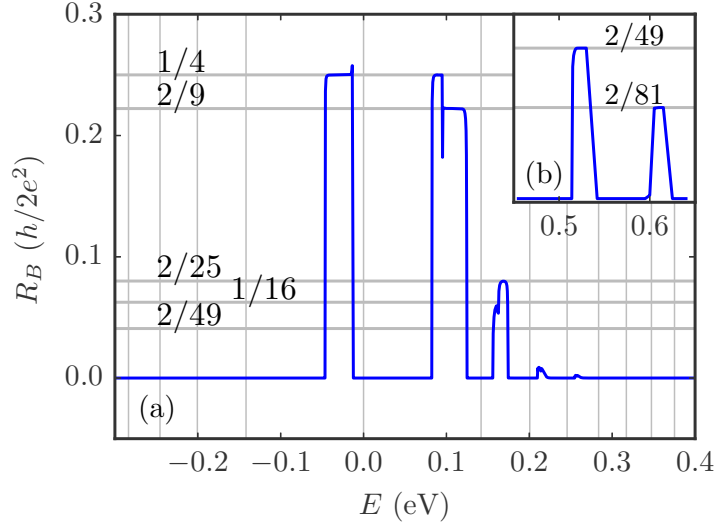


Figure 6.8: (a) Bend resistance (R_B , blue curve) obtained using KWANT, and the analytical solutions obtained from the current matrix (gray horizontal lines). Gray vertical lines mark the positions LLs for $B = 20$ T. The side-gate potential is set to $U_0 = 100$ meV. (b) Bend resistance for $n = 3$, and $n = 4$ Landau levels at higher fields $B = 100$ T, $U_0 = 50$ meV.

weaker gate potential in Fig. 6.8(b) reveals that the calculated resistance still matches the analytically obtained fractional values. Stronger field aligns the minimal band energies, since we do not observe $R_B = (1/4n^2)1/G_c$ set of resistances, where only one guided state is present in the system. Another characteristic of R_B is that it is not symmetric for electrons and holes. Plateaus appear only for zero and positive LLs. A narrow positive peak near the right corner of the first plateau, and a negative peak between the $1/4$ and $2/9$ plateaus originate from a small misalignment of subbands in the horizontal leads. Although gates G_2 and G_3 induce equal potential on the lower edge in the first and the third lead (see Fig. 6.1), this potential is slightly modified by gates on the upper edges (gates G_1 and G_2). Subbands are misaligned because of this small potential difference on the lower edge.

Results for the Hall resistance are presented in Fig. 6.9, for the same magnetic field and side-gate potential as in Fig. 6.8(a). Under the same conditions as in the case of the bend resistance, we can calculate quantization values for the Hall resistance. The conductance matrix is the same as given by Eqs. (6.8), and (6.10). But now the current is injected in the first lead

6.4. Conclusions

and collected in the third lead (the current column is $(I_1 \ -I_1 \ 0)^T$). The Hall resistance is calculated analytically as $R_{13,42} = R_H = V_4/I_1$ (because $V_2 = 0$). For two cases we obtain

$$R_H = \frac{-4n^2 + 2n + 1}{(2n)^3} \frac{1}{G_c}, \quad (6.12)$$

and

$$R_H = \frac{-4n^2 + 5}{(2n + 1)^3} \frac{1}{G_c}. \quad (6.13)$$

In Fig. 6.9 we compare the first three analytic results with the numeric ones. The main feature of the Hall resistance is that side gate potential separate the two valleys. Instead in steps of $h/4e^2$, the plateaus are separated by $h/2e^2$ (see horizontal grey lines).

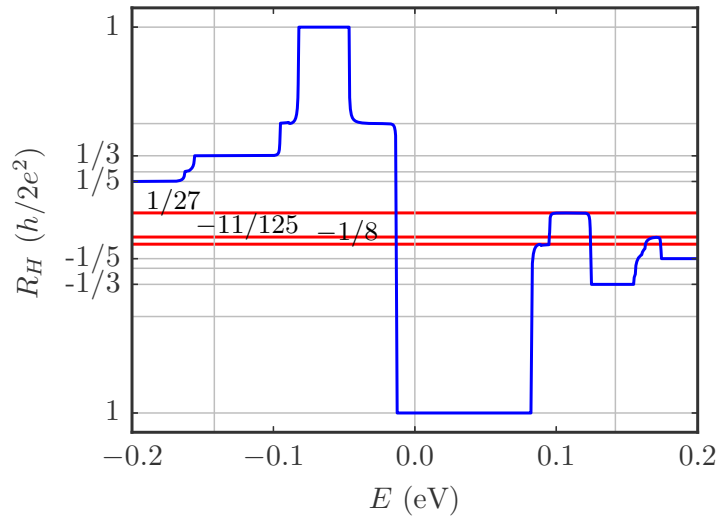


Figure 6.9: Hall resistance (R_H , blue curves) obtained using KWANT, and analytical solutions obtained from the current matrix (red horizontal lines). Magnetic field and side potential are the same as in Fig. 6.8(a).

6.4 Conclusions

In conclusion, in this chapter we investigated the quantum electron transport in side-gated Hall bars in high magnetic fields. Starting from the lead dispersion relations which reveal new states appearing in the Landau spectrum,

we proceeded to study the current density profiles of these new states in two representative leads. Spatially, the new states are guided along equipotential lines where the electron kinetic energy matches the energy of a LL. Due to a full transmission of these states the transmission matrix contains only integers, and can be solved analytically. We calculated the quantized resistances for this asymmetric gate configuration and obtained

$$R_B = \frac{1}{4n^2} \frac{1}{G_c},$$

and

$$R_B = \frac{2}{(2n+1)^2} \frac{1}{G_c},$$

for the bend resistance in two cases, when there is only one and when there are two guided states. For the Hall resistance we obtain

$$R_H = \frac{-4n^2 + 2n + 1}{(2n)^3} \frac{1}{G_c},$$

and

$$R_H = \frac{-4n^2 + 5}{(2n+1)^3} \frac{1}{G_c}.$$

The calculated quantized resistances match the quantized resistances obtained with the tight-binding method. Note that these results can be easily extended to symmetrically gated Hall bars, where potential is the same on all four gates. The derived pictures of electron guiding can be also applied to other geometries with side gates. In general, for every pair of edge states entering the system there will be a pair of guided states moving in the opposite direction.

6.4. Conclusions

CHAPTER 7

SGM microscopy of graphene magnetic focusing devices

7.1 Introduction

As explained in previous chapters, in this chapter* we deal with scanning gate microscopy (SGM) in graphene. Up to now, SGM has been successfully used to image local electron transport in various mesoscopic systems. In early applications SGM probed the interference effects produced by microscopic disorder in graphene,^{104,105} and it was later applied to image electron-hole puddles originating from extrinsic local doping.¹⁹ In the latter experiment,¹⁹ the tip was coated with a dielectric and placed directly in contact with graphene. The advantage of this approach is that AFM topography scans could be performed simultaneously with SGM scans, and the tip could be additionally used to clean the sample. Scanning technique was used in Ref. [106] to study the spatial inhomogeneity of the local neutrality point, and to measure the efficiency of intentionally embedding (writing) charges in graphene.¹⁰⁷ Tip-dependent resistance maps of a narrow quantum point contact (QPC), presented in Ref. [108], revealed a significant resistance in-

*Results presented in this chapter are based on our publication: M. D. Petrović, S. P. Milovanović, F. M. Peeters, *Scanning gate microscopy of magnetic focusing in graphene devices: quantum versus classical simulation*, *Nanotechnology* **28**, 185202 (2017).

crease when the tip was placed directly above the sample. The technique is also suitable for the investigation of localization effects. For example, concentric conductance halos were observed in SGM maps scanned around localized states in graphene quantum dots,^{24,109} narrow constrictions,^{110,111} and enhanced conductance was reported in narrow nanoribbons.¹¹² Scanning gate experiments of quantum point contacts were simulated in Ref. [113].

In this chapter, we investigate the scanning gate experiments of magnetic focusing devices reported in Refs. [20, 114, 115, 116]. Before, similar magnetic focusing measurements were performed on a semiconductor two-dimensional electron gas (2DEG) in parallel with the scanning technique.¹¹⁷ We model our device using both quantum and classical transport theory. Previously, classical simulation of such a focusing device was done in Ref. [20], and focusing without SGM tip was studied in Ref. [118]. A recent paper by Kolasiński *et al.*¹¹⁹ was the first to reproduce some of the experimental findings by applying a full quantum approach. In this chapter we implement the multi-terminal Landauer-Büttiker formalism and calculate the non-local resistances. We additionally compare the resistance maps of a 4-terminal and a 6-terminal device for different combinations of voltage probes. Due to a large size of the device, as compared to the electron wavelength, most of the simulated effects are already captured by the computationally less demanding classical model. In respect to that, we confirm that the classical billiard model can be successfully used to describe transport of relativistic carriers in the presence of inhomogeneous potentials, if the linear graphene spectrum is properly implemented.

Our analysis of simulated SGM maps confirms and expands on some of the experimental observations reported in Refs. [20, 114, 115, 116]. We consider both positively and negatively charged tip, as well as a tip acting in the mixed regime. We show that the main resistance feature (e.g. the spatial area of reduced resistance) can be explained by considering geometric relations between the device boundaries, the tip position, and the circular cyclotron orbits. One of the novel results is that the SGM tip is mainly acting on a set of trajectories that directly connect the injector lead with the tip position. The repelling tip leaves a shadow behind itself, situated in areas delimited by two direct cyclotron orbits connecting the tip with the two corners of the injector lead. The specific shape of the tip shadow, which depends on the relative position between the tip and the injector lead, determines the shape of the low resistance region. At the first focusing peak the tip is imaging a specific subset of direct trajectories connecting the two

focusing leads. This only applies for a repelling tip, or a tip operating in a mixed regime (repelling and focusing). For a tip acting as a focusing lens, the produced SGM maps do not show any significant changes in the resistance, therefore they do not provide much useful information to characterize electron transport. We additionally compare results between a 4-terminal and a 6-terminal device, and find them to be very similar, although the latter induces spatial asymmetry in the resistance maps. Results are similar because the resistance is mostly determined by the transmission function between the two focusing leads. In that sense, we confirm the approach taken in Ref. [20] which considered only transmission functions and not resistances. An important observation is that under proper conditions an SGM tip can induce a *pn* junction in the sample. This third (or mixed) regime provides much better response of the sample (due to the stronger backscattering), and results in higher contrast and resolution of the SGM resistance maps. However, this tip operation mode remains to be experimentally realized.

This chapter is organized as follows: in Sec. 7.2 we describe the focusing system, and indicate how we model the tip potential. Next, in Sec. 7.3 we scale the graphene tight-binding Hamiltonian and compare relevant quantities, such as the dispersion relation and the current density in a scaled and unscaled graphene lattice. The resistance of an unperturbed device (i.e. a device without the SGM tip) is studied in Sec. 7.4, while the analysis of SGM scans is done in Sec. 7.5. In Sec. 7.6 we present results for a six-terminal device, and discuss possible causes of the spatial asymmetry seen in the experiments. A short summary of our findings is given at the end of the chapter (Sec. 7.7).

7.2 Focusing system and SGM potential

The studied system is shown in Fig. 7.1. It is a four-terminal graphene device with the same dimensions as those used in Ref. [20]. The only major difference between our system and that of Ref. [20] is the absence of two upper leads. We implement these two leads in Sec. 7.6, and discuss the changes they introduce in the SGM maps.

Magnetic focusing occurs when electron trajectories from the 2nd lead (red curves in Fig. 7.1) bend into the 3rd lead due to an external magnetic field. Depending on the ratio between the width of the 3rd lead (l_R) and the distance between the leads (L), the diverted electrons can exit into the 3rd or the 4th lead. This switching of the exit lead manifests itself as oscillations

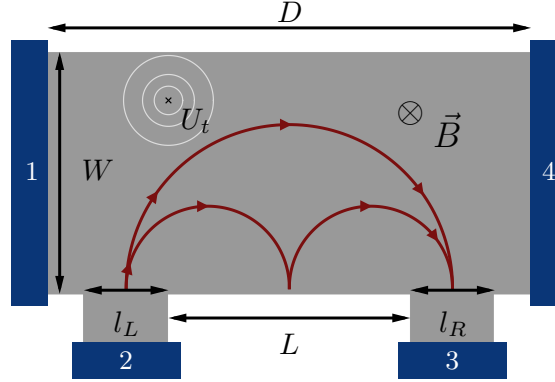


Figure 7.1: Graphene magnetic focusing device: the system width is $W = 2 \mu\text{m}$, while the system length is $D = 4 \mu\text{m}$. Both horizontal (armchair), and vertical (zigzag) leads are metallic. The vertical leads have the same width $l_L = l_R = 0.7 \mu\text{m}$, and their separation is $L = 2 \mu\text{m}$. Magnetic field is perpendicular to the graphene sheet and points in the negative z direction. Potential profile of the AFM tip is schematically represented by the white circles.

in the device resistance. Figure 7.1 shows two focusing orbits, where an even number of cyclotron radii matches the separation between the leads, $2nR_c = [L + (l_R + l_L)/2]$, where n is an integer. Focusing occurs as long as $2R_c > l_R$.

Although magnetic focusing is a local phenomena, which depends on specific paths an electron can take in the system, it is usually studied by measuring the resistance of a whole device. A lot of information is lost in such measurements (e.g. no knowledge about the most probable electron trajectories). This spatial information can be retained by scanning-gate measurements, where a SGM tip perturbs the circular electron trajectories, causing the device conductance to become tip-dependent. The conductance maps produced in such measurements reveal how device conductance depends locally on electron passage through each point.

According to Refs. [114, 20], a charged STM tip placed above a graphene sheet modifies the local charge density in graphene

$$\Delta n(\mathbf{r}) = \frac{\tilde{q}h}{(d(\mathbf{r})^2 + h^2)^{3/2}}. \quad (7.1)$$

This modification depends on the tip relative charge $\tilde{q} = -q/2\pi e$ (here q is

the actual charge accumulated on the tip, and e is the electron charge), the distance from the tip to the graphene plane h , and the distance from the tip in-plane projection to the current point $\mathbf{d}(\mathbf{r}) = \mathbf{r} - \mathbf{r}_{\text{tip}}$. A local change in the charge density modifies the local Fermi energy

$$\Delta E_F(\mathbf{r}) = E_F(n) - E_F(n + \Delta n(\mathbf{r})), \quad (7.2)$$

which manifests as an additional (tip-induced) potential $U_t(\mathbf{r}) = \Delta E_F(\mathbf{r})$. Since Fermi energy in graphene depends on the charge density through $E_F(n) = \hbar v_F \sqrt{\pi n}$, the induced potential is

$$U_t(\mathbf{r}) = \hbar v_F \sqrt{\pi} \left(\sqrt{n} - \sqrt{n + \Delta n(\mathbf{r})} \right). \quad (7.3)$$

This potential is a function of the global charge density n and the local charge modification $\Delta n(\mathbf{r})$. The global density n is set by the back-gate voltage, while the local modification $\Delta n(\mathbf{r})$ is determined by the tip height and the tip charge.

An alternative way to look at the tip perturbation is through the tip-generated force field. Charge carriers traveling through the system experience a force $\mathbf{F}(\mathbf{r}) = -\nabla U_t(\mathbf{r})$ generated by the tip. This force modifies the carrier equation of motion²⁰

$$\frac{d^2 \mathbf{r}}{dt^2} = \frac{\mathbf{F}(\mathbf{r})}{m^*} = \frac{1}{2} v_F^2 \frac{\nabla \tilde{n}(\mathbf{r})}{\tilde{n}(\mathbf{r})}, \quad (7.4)$$

where m^* is the carrier mass in graphene ($m^* = \hbar \sqrt{\pi n} / v_F$), and $\tilde{n}(\mathbf{r}) = n + \Delta n(\mathbf{r})$ is the resulting charge density. The derivation of the force field used in our classical model is presented in Appendix A.

Fig. 7.2 shows tip-induced potentials for different combinations of the global charge density and the local charge modification. There are six different regimes in which the tip can operate, but only three of these six are unique. The other three regimes can be obtained by exchanging electrons with holes. The first regime is presented in Fig. 7.2(a). Here, a positively charged tip increases the local electron density beneath itself, which manifests in the negative potential profile shown in Fig. 7.2(g). The tip-induced force field in Fig. 7.2(j) reveals a focusing nature of the tip. The case of negatively charged tip in Fig. 7.2(b) was previously studied experimentally.²⁰ As shown in Ref. [20] and in Fig. 7.2(h), the tip creates a positive potential which then repels the incoming electrons. The force field in this regime, shown in Fig. 7.2(k), is pointing away from the tip. In both Figs. 7.2(a) and 7.2(b) we

7.2. Focusing system and SGM potential

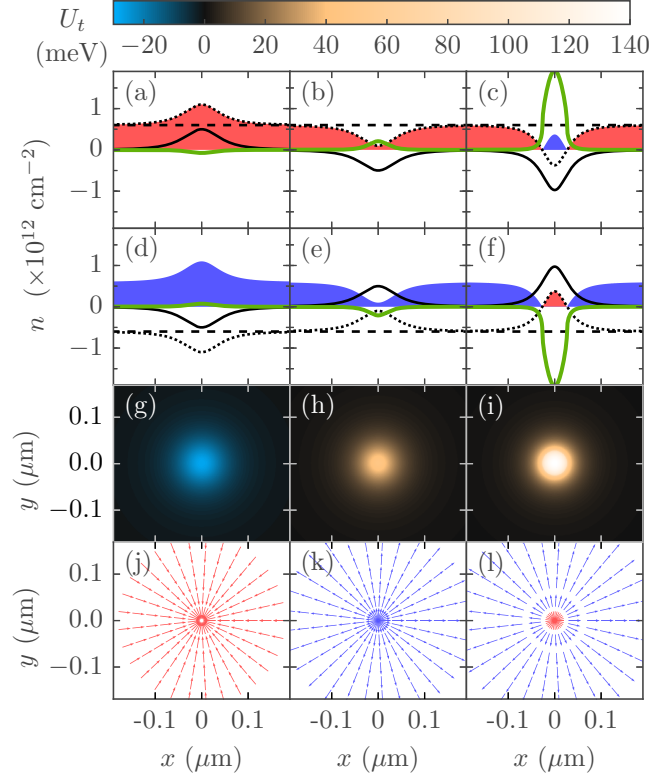


Figure 7.2: (a)–(f) Charge density beneath the tip ($x_{\text{tip}} = y_{\text{tip}} = 0$) for electrons (red), and holes (blue). Solid-black curves show the local charge modification $\Delta n(\mathbf{r})$, while dashed-black lines mark the global density n . Dotted-black curves show the resulting density $\tilde{n}(r) = n + \Delta n(r)$, and green curves show the tip-induced potential. (g)–(i) Tip-induced potential for three regimes in (a), (b), and (c), respectively. (j)–(l) Directions of the force field acting on the charge carriers.

set $|\Delta n(\mathbf{r})|$ to $5 \times 10^{11} \text{ cm}^{-2}$. This density was used in Ref. [20] to fit the experimental data, and it corresponds to a tip positioned $h = 60 \text{ nm}$ above the graphene sheet. Assuming the tip charge \tilde{q} does not depend on the tip height h , in the far-left column of Fig. 7.2 we present results for a tip positioned closer to the sample ($h = 43 \text{ nm}$). When changing the tip height, we first calculate the tip charge \tilde{q} from the modified charge density $\Delta n(r_{\text{tip}}) = \tilde{q}/h^2$, and then we recalculate Δn for the new height.

Contrary to a classical 2DEG, where the tip depletes the electron density beneath it,³⁸ in graphene (due to its gapless nature) the depleted electrons turn into holes. The induced potential in this third (or mixed) regime is much

stronger than in both, focusing and repelling regime (compare Fig. 7.2(i) with Figs. 7.2(g) and 7.2(h)). The force field is also specific (see Fig. 7.2(l)): in the n region (surrounding the tip) the tip repels incoming electrons, while in the p region (beneath the tip) the tip focuses tunneling holes. The actual tip height used in the experiment²⁰ could not go below 50 nm (because of the 50 nm thick BN layer separating the tip and the graphene sample). However, this does not mean that the third scanning regime is experimentally inaccessible. Enhanced tip potentials can be realized by lowering the global electron density n , or by increasing the tip charge \tilde{q} .

As stated above, we model this system from two perspectives, the quantum and the classical one. The classical billiard model is the same as that used in Ref. [118], while the quantum simulations are performed using KWANT,²⁷ a software package for quantum transport.[†] In the classical approach the edges are considered to be uniform and continuous, and the reflection of electrons at the edges is assumed to be specular. The magnetic field in the quantum model is implemented through Peierls phase, as explained in Chap. 5, and the resistances are obtained by applying the Landauer-Büttiker formalism for a four-terminal⁸⁶ and multi-terminal²⁸ device (as also explained in Chap. 2).

7.3 Scaling the tight-binding Hamiltonian

In order to simulate devices of similar sizes as those used in the experiment,²⁰ we scale the graphene tight-binding Hamiltonian. As explained in Ref. [120], a scaling coefficient s_f is introduced. This coefficient increases the spacing between the carbon atoms $a = s_f a_0$, and simultaneously decreases the nearest neighbor hopping energy $t = t_0/s_f$. The scaling procedure allows for simulations of systems with dimensions comparable to those used in actual experiments (in order of microns), but with lesser number of tight-binding orbitals. However, the scaling has its limits. Results for larger s_f are less accurate, particularly for higher energies (away from the linear part of the spectrum). Close to the Dirac point the scaled system is still a good approximation of the pristine graphene lattice. A very recent study on graphene magnetic focusing¹²¹ used an alternative way to scale the tight-binding Hamiltonian. They scaled the Fermi energy instead of the hopping term. Beside the scaling procedure, this reference compares results of tight-binding and classical

[†]Modeling and calculations using the classical billiard model are performed by my colleague Slaviša P. Milovanović.

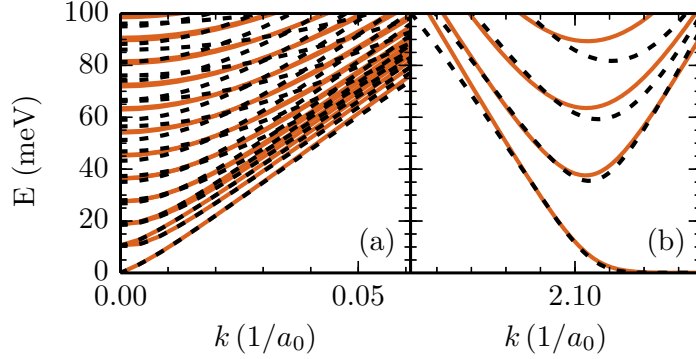


Figure 7.3: Dispersion relations of the 1st (a) and the 2nd (b) lead. The 1st and the 2nd lead connect the first and the second contact with the main scattering region (contacts are labeled in Fig. 7.1). Leads in KWANT are modeled as semi-infinite nanoribbons. The magnetic field is $B = 0.1$ T. Energy bands of pristine graphene are shown in orange, while those of the scaled graphene ($s_f = 15.15$) are shown by the black dashed curves. System dimensions are ten times smaller than those used in Fig. 7.1. Since the scaling procedure modifies the inverse (k) space, we translated the K-point of the scaled system in (b), to match it with the K-point of the pristine graphene lattice.

model, and also gives comparison with experimentally measured resistances.

To test the validity of the scaling procedure, we compare in Fig. 7.3 the dispersion relations obtained using scaled Hamiltonian with those obtained using the pristine graphene lattice. Since performing tight-binding calculations on a micrometer scale is computationally very demanding, we test the scaling procedure on a system ten times smaller than that presented in Fig. 7.1. The lattice scale of this smaller system ($s_f = 15.15$) is comparable to the lattice scale we use in the rest of the chapter to simulate the micrometer-sized system shown in Fig. 7.1 ($s_f = 15.34$). As expected, the scaled dispersions match the pristine graphene lattice dispersions for low energies (below 100 meV). Although the band minimal energies differ, the scaled lattice is a good approximation for states away from the subband minima. Note that the scale is chosen such that it preserves the metallic nature of the armchair leads, as is seen in Fig. 7.3(a).

Since SGM experiments probe the local properties, it is necessary to determine how scaling affects them. With that in mind, in Fig. 7.4 we compare two current densities: one for scaled, and one for an unscaled lattice. Be-

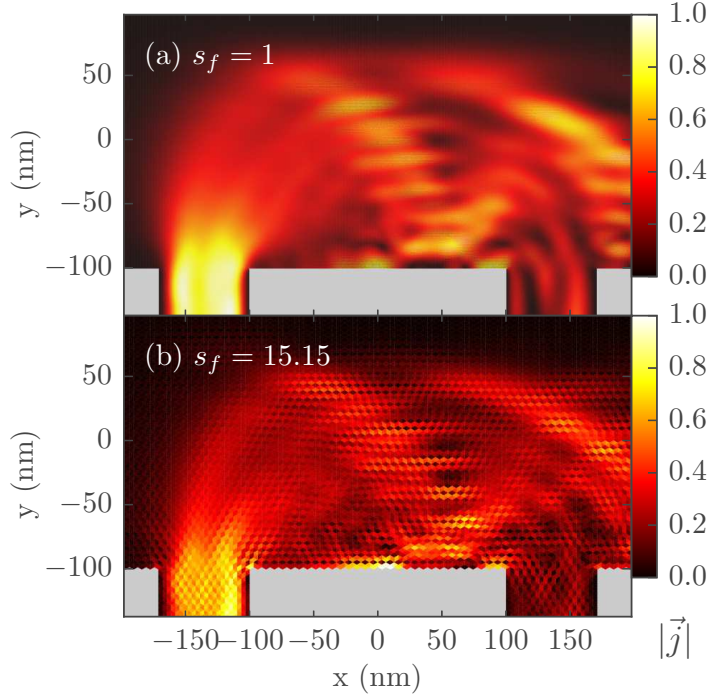


Figure 7.4: Normalized current density when current is injected from the second lead: (a) pristine graphene lattice ($s_f = 1$), and (b) scaled graphene lattice ($s_f = 15.15$). $B = 1$ T, and $E_F = 80$ meV. The presented system is ten times smaller than that in Fig. 7.1. SGM tip is not present.

side the loss in resolution (caused by a lesser number of carbon atoms), the general current flow patterns are preserved with scaling, which confirms that this method can be used to simulate SGM experiments.

7.4 Magnetic focusing

In this subsection we investigate the general transport properties of the focusing device when no SGM tip is present. We are interested in how the focusing resistance ($R_m = R_{12,43}$) changes as a function of the magnetic field B , and the electron density n (or Fermi energy). In general, as explained in previous chapters, $R_{ij,km}$ refers to the resistance when current is injected from contact i and collected at contact j , while voltage is measured between contacts k and m (contacts and their corresponding leads are labeled in Fig. 7.1). Ref. [20] reported several resistance peaks as a function of the applied field,

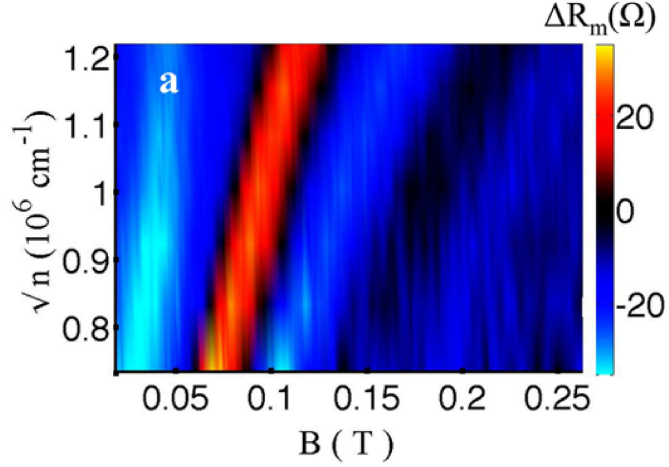


Figure 7.5: Experimentally measured changes in the focusing resistance (ΔR_m) as a function of magnetic field and charge density (Fermi energy). Figure taken from Ref. [20].

and these peaks were related with the current focusing. Figure 7.5 shows experimentally measured changes in the resistance R_m (the figure is taken from Ref. [20]). A clearly visible red region corresponds to the first focusing peak, while the black region located at two times higher fields corresponds to the second focusing peak. We simulate these measurements, and in Fig. 7.6 we present a comparison of the resistances obtained from both, quantum and classical simulation. To match our color-maps with those of Ref. [20], in both cases (quantum and classical) we subtract $R_0 = 28 \Omega$ from numerically calculated $R_{12,43}$. This value (R_0) is very close to $(R_m^{\max} + R_m^{\min})/2$. The resistances obtained with the two methods agree both qualitatively and quantitatively. The only difference is that resistances obtained with the quantum method show a set of parabolic fringe lines at higher fields, coming from Landau quantization. The classical method does not account for transversal quantization in the leads, and for the existence of transverse modes, hence the transmissions obtained classically need to be properly scaled before resistance calculations. We perform this scaling by multiplying the classically obtained transmissions with the approximate number of modes in the source lead⁴

$$M_i = 2 \frac{E_F W_i}{\hbar v_F \pi}. \quad (7.5)$$

Here index i refers to the leads, W_i is the width of the i -th lead, E_F is the Fermi energy in the i -th lead, v_F is the graphene Fermi velocity, while coeffi-

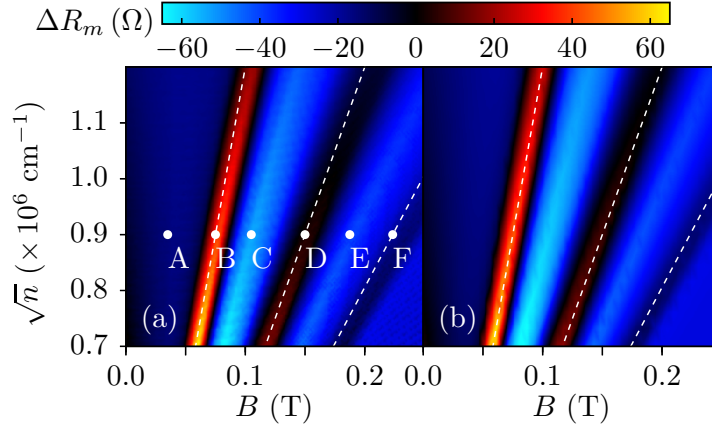


Figure 7.6: Change of the $R_m = R_{12,43}$ resistance versus the magnetic field and the electron density (Fermi energy) obtained from (a) quantum, and (b) classical simulation. In order to be able to compare both results with those published in Ref. [20], we calculate ΔR_m by subtracting $R_0 = 28 \Omega$ from numerically obtained $R_{12,43}$. The white dashed lines mark the first three focusing maxima, and they correspond to cyclotron radii of $1.4 \mu\text{m}$, $0.7 \mu\text{m}$, and $0.47 \mu\text{m}$. Labels A–F mark the (\sqrt{n}, B) points for which we present the current density in Fig. 7.7.

cient 2 is added to account for contributions coming from the two valleys. The graphene Fermi velocity v_F in the tight-binding model is determined (to first approximation) from the nearest-neighbour hopping energy as $v_F = 3|t|a/2\hbar$, where a is the distance between neighbouring carbon atoms. For $t = 2.7 \text{ eV}$, and $a = 1.42 \text{ \AA}$ we obtain $v_F = 873\,893 \text{ m/s}$, which is the value that we use in our classical model.

Since the cyclotron radius in graphene is proportional to the Fermi energy $R_c = E_F/(ev_FB)$, and Fermi energy is proportional to carrier density $E_F = \hbar v_F \sqrt{\pi n}$, then $\sqrt{n} = \gamma R_c B$ (where $\gamma = e/(\hbar\sqrt{\pi})$). In other words, for equiradial lines, \sqrt{n} is a linear function of the applied magnetic field. In Fig. 7.6 we mark three such lines (white dashed lines) for three cyclotron radii ($1.4 \mu\text{m}$, $0.7 \mu\text{m}$, and $0.47 \mu\text{m}$) in order to match the first three focusing maxima.

For narrow focusing leads (leads 2 and 3), resistance peaks appear each time a multiple of a cyclotron diameter $2R_c$ matches the lead distance L . However, if the lead widths (l_R and l_L) are comparable to the distance between them, it is reasonable to assume that focusing would occur only when electron injected from the middle of the input lead exits in the middle of the

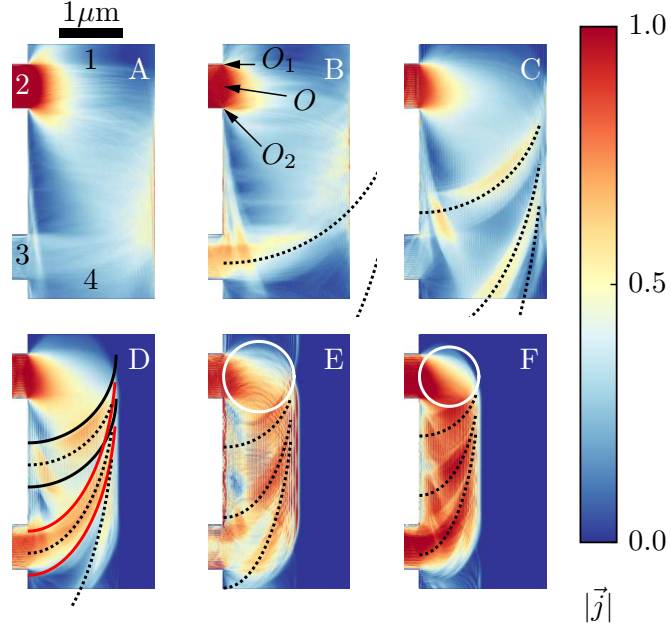


Figure 7.7: Normalized total current density at different focusing fields: (A) 35 mT, (B) 75 mT, (C) 105 mT, (D) 150 mT, (E) 188 mT, and (F) 223 mT (points A–F marked in Fig. 7.6). The current is calculated using the quantum method. The electron density is $n = 8.1 \times 10^{11} \text{ cm}^{-2}$. Lead numbers for this rotated system are shown in figure A. Black-dashed curves show elliptical trajectories given by Eq. (7.6), and centered on the middle of the 2nd lead (point O). Black and red full curves show the same trajectories, but now centered at the corners of the 2nd lead (points O_1 and O_2). White circles in E and F show cyclotron orbits for these two figures.

output lead. Two such trajectories are presented in Fig. 7.1. A simplified focusing formula, which includes the lead widths, would then be $2nR_c = (L+l)$. For $L = 2 \mu\text{m}$ and $l = 0.7 \mu\text{m}$, the first three focusing radii are $1.35 \mu\text{m}$, $0.675 \mu\text{m}$ and $0.45 \mu\text{m}$, which approximately match the three lines shown in Fig. 7.6. For cyclotron radii smaller than half of the lead width ($0.35 \mu\text{m}$) focusing is no longer possible.

To test whether the three resistance peaks in Fig. 7.6 appear due to the current focusing, we show in Fig. 7.7 the local current density for electrons coming from the 2nd lead, for points A–F marked in Fig. 7.6(a). The current is obtained using the quantum (tight-binding) model. Insets B, D, and F indeed show high current concentration in the exiting (3rd) lead, which confirms our

assumption. For stronger fields (insets D, E, and F) the current flows close to the system lower edge (the left edge in Fig. 7.7) in an area one cyclotron diameter wide. The reason why current spreads in an area one cyclotron diameter wide, and not one cyclotron radius wide, is the following: in the classical picture, electrons which enter the system perpendicularly to the lower edge (i.e. parallel to the focusing leads) would spread approximately one cyclotron radius away from the edge, since their trajectories consist of semicircles (see the two trajectories in Fig. 7.1). On the other hand, electrons entering the system almost parallel to the lower edge (i.e. normal to the focusing lead direction) would make almost a full circle before they scatter on the lower edge (see the two white circles in insets E and F in Fig. 7.7). The current then spreads in a diameter-wide area due to these electrons. For weak fields most of these electrons do not even make a full orbit, because they exit into the 1st lead (see insets A and B in Fig. 7.7, where one part of the current from the 2nd lead exits into the 1st lead).

Current in the system can be understood in terms of the cyclotron orbits. Based on the picture of classical trajectories presented in Ref. [122], we plot three envelope curves (black-dotted lines) to mark three paths where (according to the classical picture) the current is supposed to travel. Each of these three curves is a part of an ellipse

$$(x - x_0)^2 + \left(\frac{y - y_0}{2n}\right)^2 = R_c^2, \quad n = 1, 2, 3, \dots \quad (7.6)$$

centered on the middle of the input lead $(x_0, y_0) = O$ (see point O in Fig. 7.7B). It is clear that focusing occurs in insets B, D, and F, since for these insets the elliptic curves pass through the 3rd lead. The input lead has a finite width, hence these trajectories spread in space. The spread of current density is delimited by elliptical curves defined by Eq. (7.6) (black and red full curves in Fig. 7.7D), but now centered on two corners of the input lead (see points O_1 and O_2 in Fig. 7.7B).

7.5 Scanning gate microscopy

In this part we investigate resistance maps obtained when SGM tip is present. Experimental results presented in Fig. 7.8 show the evolution of the scanned resistance with magnetic field and electron charge density. As we explain below, the areas of suppressed resistance (red and orange areas) shown in these maps correspond to imaged electron trajectories. In this subsection

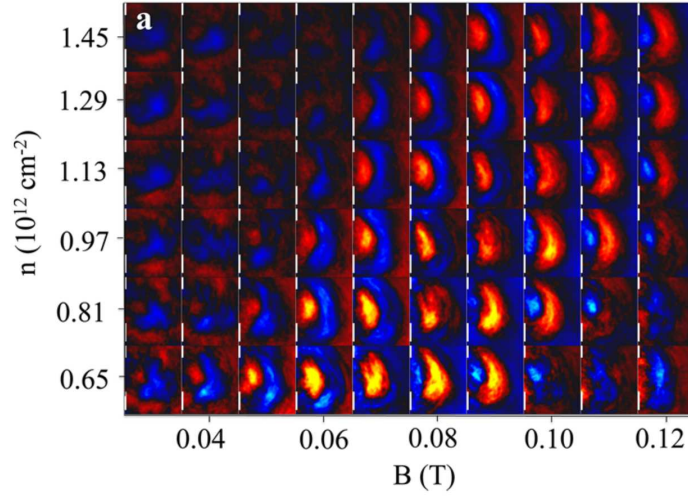


Figure 7.8: Experimentally measured SGM maps as a function of electron density and magnetic field. Figure taken from Ref. [20].

we simulate these experimentally obtained resistance maps. We mentioned above that there are three regimes in which the tip can operate, therefore we additionally compare how scanning maps change in these three regimes.

Simulated resistance maps are presented in Fig. 7.9. In general, local features of the SGM maps obtained with the two models (quantum and classical) match well, and the two models also manage to capture some of the experimental features (e.g. low resistance regions). This match between the quantum and the classical model is expected since the system size is larger than the electron wavelength, hence some of the interference effects are suppressed. Figure 7.9 also confirms that on these scales a computationally less demanding classical model manages to capture all the features obtained with a more detailed atomistic model.

The first two rows in Fig. 7.9 show SGM maps for a repulsive (negatively charged) tip, as it was used in the experiment.²⁰ The calculated resistances are very similar to the measured ones,²⁰ and the main difference is that our results possess some extra oscillations close to the upper edge (shown on the right side in the rotated system in Fig. 7.9). As we show below, these features originate from multiple electron scatterings between the tip and the upper edge. The defining characteristic of all SGM maps obtained with repelling tip is a region of suppressed resistance close to the lower edge. This region evolves as magnetic field is increased and as shown in recent experiments, it

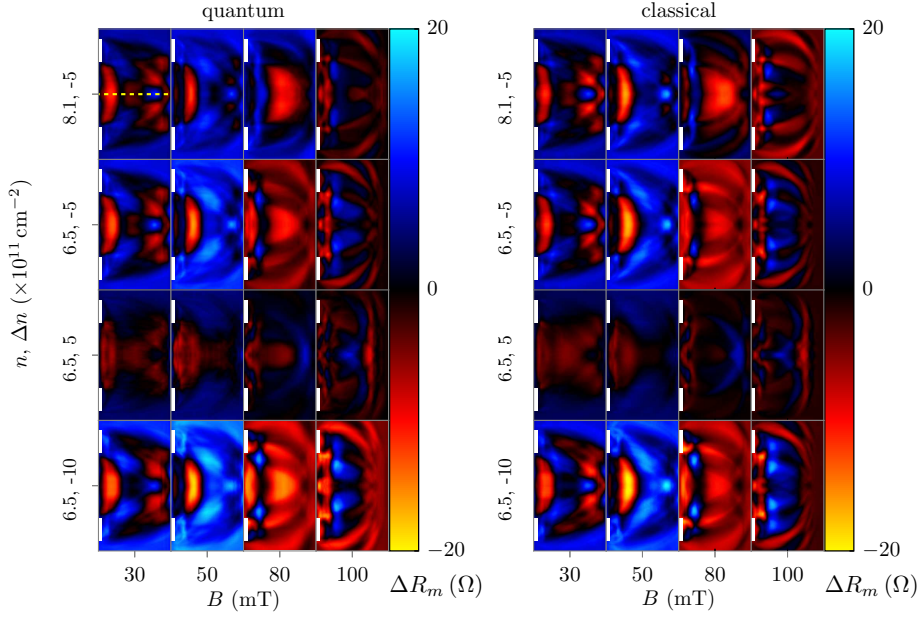


Figure 7.9: Comparison of the SGM resistance maps obtained from quantum (left) and classical (right) simulation. The two white stripes in the figures mark the positions of the 2nd and the 3rd lead. Labels on the left mark the electron density n , and the maximal change in the charge density introduced by the tip Δn . ΔR_m is calculated by subtracting $R_0 = (R_{12,43}^{\max} + R_{12,43}^{\min})/2$ from $R_{12,43}$ for each scan. Yellow-dashed line in the first row marks the mirror symmetry axis.

can be connected with the cyclotron radius.¹¹⁵

Resistance maps obtained with the focusing (positively charged) tip (third row in Fig. 7.9) convey less information than those obtained with a repelling tip. Although the tip causes some change in the resistance, some other effects, e.g temperature smearing, would even more degrade the obtained resistance maps. Therefore a tip in the focusing regime is probably not the best choice to probe electron transport. The third (mixed) regime seems to produce the largest change in the resistance: R -maps obtained in this regime show almost identical features as those obtained with a repelling tip, but the sample response is much better due to a stronger repelling force.

Previous (classical) simulations of magnetic focusing²⁰ considered only electron transmissions between the two focusing leads, and not the resistances. Here, we verify that this approach is valid. In Fig. 7.10 we compare

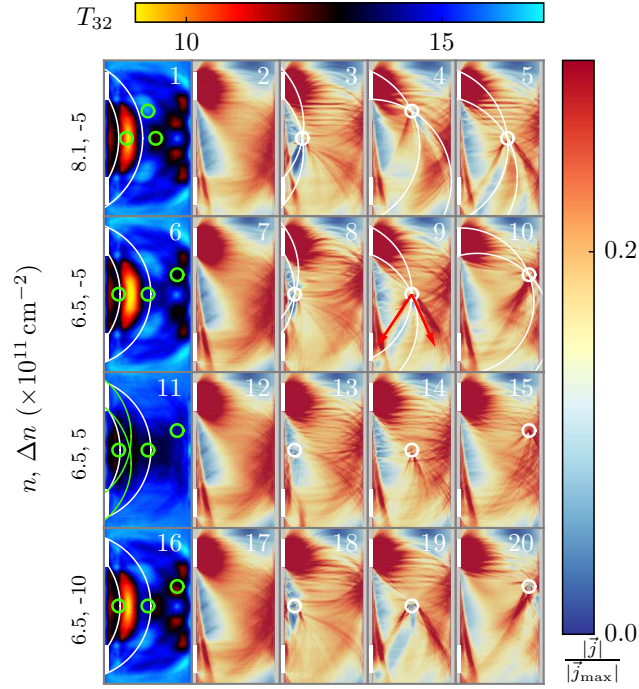


Figure 7.10: Transmission maps (1st column on the left) and normalized electron current densities (columns 2–5). In the second column we present current density with no SGM tip, and in the last three columns we show current densities for specific tip positions (white circles). The four rows correspond to the same four $n, \Delta n$ configurations as used in Fig. 7.9. Magnetic field is $B = 50$ mT. In insets 3–5, and 8–10 we mark the direct trajectories connecting the corners of the 2nd lead with the tip position. The white lines in the first column delimit the areas relevant for focusing.

the transmission maps between the two focusing leads (T_{32} , left column) with the current densities (columns 2–4) for some specific tip positions (white and green circles). Calculated transmissions in the 1st column of Fig. 7.10 resemble the corresponding R -maps in Fig. 7.9 (columns for $B = 50$ mT in Fig. 7.9). Most of the features of the resistance maps are determined by the tip position relative to the two corners of the injector lead. In each of the insets 3–5, and 8–10, we show two cyclotron orbits that directly connect the tip with the two corners (two white arcs in each of these insets). As shown in these insets, a trail of suppressed current is seen as a shadow that the tip leaves behind itself. The shadow is situated mostly in the area enclosed be-

tween the two cyclotron orbits. These two orbits (originating at two corners of the 2nd lead) mark the boundary of a set of direct cyclotron trajectories that connect the tip with the 2nd lead. The current is suppressed in these areas, because the tip blocks these trajectories. The diverted current forms an arc around the tip, and it flows away from the blocked area (see the two red arrows in inset 9, showing the flow direction of the diverted current). Similar explanation for the diverted current is given in Ref. [116]. Our interpretation (based on the two delimiting orbits) also explains the areas of strongly suppressed resistance. Insets 8 and 9 show two positions of the tip lying on the edge of the resistance suppressed region (see inset 6). For any point lying on a line between these two points, the trail of blocked current coincides with the 3rd lead. From these simple geometric relations, we see that the area of suppressed conductance is delimited by two cyclotron orbits that directly connect inner and outer corners of the focusing leads (white curves in the 1st column of Fig. 7.10). The maximal resistance suppression is expected at the crossing point of orbits connecting inner and outer corners (see the two green curves in inset 11, and also the two cyclotron orbits in inset 3). Based on the previous analysis, we conclude that the finite width of the suppressed resistance region is an indirect consequence of the finite width of the two focusing leads.

The results for a focusing tip reveal effects opposite to those of the repelling tip (compare the tip influence on the current densities in the second and the third row in Fig. 7.10). The focusing tip leaves a trail of enhanced current instead of a shadow, as seen in the case of a repelling tip (compare insets 10 and 15). In the last row, a tip in the mixed regime shows a much darker shadow behind itself as compared to the repelling tip. The mixed nature of the tip manifests itself in a current profile, where some of the current that manages to tunnel through the potential induced by the tip, exits focused on the other side.

7.6 Resistance maps of a six-terminal device

Although previous resistance maps capture the main features reported in the experiment²⁰ (e.g. they show semicircular areas where the resistance is reduced, and these areas coincide with the focusing trajectories), they possess some additional features which were not observed experimentally. The major difference is that the simulated resistance maps are symmetric with respect to mirror reflection along the middle line of the system (the yellow-dashed line

in the first row of Fig. 7.9). The cyclotron orbits imaged in the experiment²⁰ (Fig. 7.8) were not perfectly symmetric with respect to this transformation. This asymmetry could originate from several different sources. For example, it could come from local impurity charges trapped in the sample. Due to the electric forces coming from these charges, transmitted electrons could divert from their ideal circular trajectories. Although this is a possible explanation for the asymmetry, it is unlikely in samples sandwiched between h-BN, hence here we will discuss other possible sources.

Our initial assumption was that the asymmetry originates from a difference in widths of the two focusing leads (the 2nd and the 3rd lead). We tested this by changing the width of the 3rd lead, and recalculating some of the resistance maps of Fig. 7.9. Using a wider ($l = 1.2l_L$), or a narrower ($l = 0.8l_L$) 3rd lead did not significantly change the symmetry of the resistance maps, and can not account for what is observed in the experiment. Our second assumption was that the asymmetry originates from an asymmetry in the tip-induced potential. An uneven distribution of charges on top of the tip, or a tip not properly aligned to the vertical (z) axis would create an anisotropic image-charge density, and consequently an anisotropic tip potential. We tested this by modifying the eccentricity of an elliptic charge density, but the obtained resistance maps were not significantly modified. In general, we could not reproduce the measured resistance asymmetries in an impurity-free four-terminal device.

Since the original experiment was performed in a six-terminal device, in order to check how resistance maps change for different configurations of the voltage probes, we add two new leads to our system. We label these new leads as lead 5, and lead 6, and they are placed opposite to the two focusing leads. Our system is now a symmetric, six-terminal Hall bar often used in standard quantum Hall measurements.

Resistance maps of this system are shown in Fig. 7.11, for three different cases. The first row presents data for the same probe configuration as in Fig. 7.9, but now with two new leads included. When compared with Fig. 7.9, the new leads do not destroy the characteristic features in the resistance maps, yet they modify them. The region of suppressed resistance is still delimited with two cyclotron orbits connecting the outer and inner corners of the two focusing leads (violet and green curves in the first row of Fig. 7.11), and maximal resistance suppression is still determined by the orbits connecting the middle lines of the two focusing leads (the white curves). Also, the order of magnitude of calculated resistances does no change.

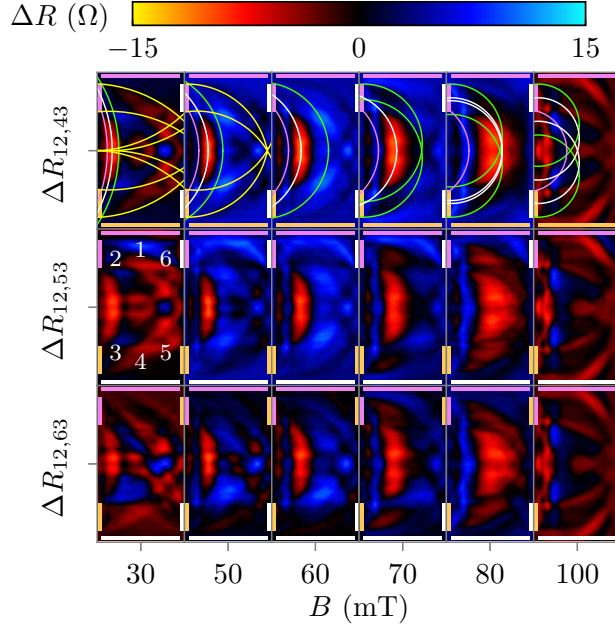


Figure 7.11: Resistance maps of a six-terminal device for different measurement configurations: $\Delta R_{12,43}$ (1st row), $\Delta R_{12,53}$ (2nd row), $\Delta R_{12,63}$ (3rd row), and for different magnetic fields (columns). Global electron density is $n = 8.1 \times 10^{11} \text{ cm}^{-2}$, and maximal tip-induced change in the charge density is $\Delta n = 5 \times 10^{11} \text{ cm}^{-2}$. All resistances are obtained using the quantum (tight-binding) approach. Resistance R_0 is calculated and subtracted from every inset, similarly as in Fig. 7.9. Lead numbers are presented in the left figure in the second row.

Yellow curves in the first row of Fig. 7.11 (for 30 mT, and 50 mT) show indirect trajectories that connect the two focusing leads. In the first case (for 30 mT), we present a set of trajectories where electron is scattered three times at the edges, while in the second case (50 mT), a set of trajectories with a single scattering. In order to draw these trajectories, we assume elastic scattering at the edges, with the normal component of electron velocity (component normal to an edge) changing its sign. In the same manner as with the direct trajectories, we show only those trajectories that connect the two inner and two outer lead corners, however there is another set of indirect trajectories that connect the inner with outer corners. Areas of suppressed resistance near the edges coincide with these indirect trajectories, while areas of enhanced resistance lay in-between these trajectories. It is important

to notice that these trajectories were not observed in the experiment.²⁰ One of the explanations is that they occur in very narrow regions, and this requires perfect elastic scattering and focusing of electrons. This focussing was strongly suppressed in the experiment, because the sample edges were not perfectly ordered, nor were the electrons perfectly elastically scattered. Another factor which is important is the modification of electron charge density near the edges. Ref. [123] reported (based on the self-consistent solutions of the Poisson's equation) significant deviations of density near the edges—as compared to the bulk density. This difference in charge density, but also edge roughness, is one of the explanations why finer details (related to indirect trajectories) were not observed in the experiment.²⁰

A recent work on magnetic focusing¹²⁴ reported anomalous oscillations of the Hall resistance with magnetic field. These oscillations appear between the classical (focusing) regime and the quantum Hall regime, and they were associated with the interferences of plane wave parts of the edge states. Another feature reported in Ref. [124] is different behaviour of the current near zigzag as compared with armchair edges. As our previous results show, we do not observe such effects, and this is mostly because we consider a system between the first and the second focusing peak. As for the edge current, we only studied the case of an armchair edge, and there is no particular current concentration near the edges similar to that reported in Ref. [124].

The second row in Fig. 7.11 corresponds to probe configuration actually used in the experiment.²⁰ A slight asymmetry is introduced by keeping the current probes (leads 1 and 2), and changing the voltage probes (from measuring V_{43} , to measuring V_{53}). Although the suppressed region is still fairly symmetric, an asymmetry is evident if we compare upper and lower parts of the R -maps. The third row shows R -maps obtained by measuring the voltage across the device (V_{63}). A clear asymmetry is evident for lower fields. In general, the measured voltage depends mostly on how much of the electron current is scattered into the voltage leads. For stronger fields, most of the current is located away from the new leads, on the lower edge, and therefore the scattering is negligible.

Since we demonstrated that most of the transport in this system is determined by considering direct electron orbits, the interface between the focusing leads and the main region might play a significant role. In this chapter we considered only leads with perfect (90° degrees) corners, but due to an imperfect etching these corners might be more smooth, thus allowing for some additional effects (e.g. new set of direct trajectories).

7.7 Summary

In this chapter we performed simulations of the scanning gate measurements in graphene magnetic focusing devices. Two methods (quantum and classical) were used to obtain the system transmissions. These transmissions were then applied in the (multi-terminal) Landauer-Büttiker formula to calculate the device resistances. In order to perform the quantum simulations, the graphene tight-binding Hamiltonian needed to be properly scaled.

In case without the SGM tip, the focusing resistance $R_m(E, B)$ reveals three focusing peaks, which are related with three cyclotron radii. These radii were calculated using the distance between the two focusing leads, but only after including the lead widths.

Depending on the voltage on the back-gate and the charge accumulated on the tip, we differentiate between six different regimes in which the tip can operate. Three out of these six regimes are unique. Due to the large system size, all the features of the resistance maps are captured with the classical model, and can be explained by tip influencing the direct cyclotron orbits coming from the 2nd lead. Our results show that the largest change in the resistance is obtained for a tip operating in the mixed regime (simultaneously repelling and focusing electrons). It is important to stress that, as compared to experiments in classical 2DEG,¹¹⁷ in graphene (due to the absence of an energy gap) the tip can induce a *pn* junction which leads to an enhanced response of the sample, due to the stronger backscattering. This third (or mixed regime) was not realized in recent experiments,^{20,115} and therefore presents an interesting regime to be investigated in future experiments. The spatial asymmetry in experimentally obtained R -maps can be partially explained by the specific configuration of the voltage probes, but we do not rule out other sources, such as charged impurities or edge imperfections produced during the etching process.

7.7. Summary

CHAPTER 8

Summary and outlook

In this thesis we theoretically investigated the scanning gate microscopy technique (SGM), and its application in imaging 2D electron transport in graphene and semiconducting heterostructures. Beside SGM, we studied electron transport in nanostructured graphene without SGM tip. In the course of these investigations two distinct numerical methods were used: the time dependent propagation of wave packets, and the tight-binding wave function approach as implemented in the KWANT software package.

Scanning gate microscopy is a relatively new measuring technique, and based on the two examples presented in this thesis (Chaps. 3 and 7) the potential for its application in characterization of electron transport becomes evident. In combination with other scanning techniques (e.g. AFM), SGM can provide additional information useful in determining the connection between the structure of a nanodevice and its conductance. As shown in Chaps. 3 and 7, the SGM method can be applied on different materials and in different transport regimes. The only prerequisite is that the electron gas is situated close to the surface. The results presented in Chap. 3, SGM can be used to study quantum phenomena where the SGM tip interacts with electron waves, and the resulting conductance map shows interference effects. The second case (investigated in Chap. 7) shows that the technique can be used to investigate ballistic transport on a micrometer scale to image classical electron trajectories. The technique can be used in other cases (not con-

sidered in this thesis) to study localization effects in quantum dots, where characteristic concentric halos appear around the centers of localization. All these results point towards the fact that when interpreting the SGM maps, it is important to take into account not only the characteristics of 2DEG, but also the regime in which the measurements are conducted. Depending on the case, the tip-induced potential can be interpreted as a movable obstacle that backscatters the incoming electrons, or as a tool to locally control the electronic density (as in the case of localization, where the tip acts as a movable top gate), or as a lens which casts a shadow behind itself (as in the case of magnetic focusing experiments).

The two cases of SGM application which we investigated in this thesis are mutually very different. In the first case (AB rings), we focused on a system whose size was comparable to the size of the tip-induced potential. Because of this the whole system could be considered as quasi-one-dimensional from the SGM tip point of view. On the other hand, in the second case (the graphene magnetic focusing device) the tip-induced potential was several times smaller than the studied device, and this allowed for imaging of ballistic electron trajectories. Both examples demonstrated that the most important property in SGM experiments is the tip-induced potential. From the experimental point of view, further characterization of the tip potential is necessary in order to provide better control of future SGM experiments. Experiments such as that performed in Ref. [23] showed that 2DEG nanostructures, beside being objects of experimental study, could also be used as nano-measuring devices. Future experiments could implement quantum dots as local potentiometers placed in the vicinity of other nanostructures with the special task of measuring the SGM tip potential. When it comes to theory of SGM, further investigation between the measured conductance change and the local properties such as local current density is necessary in order to provide better interpretation of the measured conductance maps. Unlike in STM measurements, the induced SGM tip potential is not localized around one atom, or small group of atoms, instead it spreads in wider areas. The measured conductance change then does not depend on the local current right beneath the tip, but on the average current in the area of the tip-induced potential. In other words, a connection between the local current density and the measured conductance change is not a simple point-to-point function, but a convolution which depends on the tip-induced potential. Ideally, an ultimate goal of a theoretical study would be to find an inverse transform, which together with the measured tip potential and the conductance map would produce

the local current density. This transform function is still missing. Similar work was previously done in Ref. [125] where a Hall bar was used to map inhomogeneous magnetic fields. A transform function was used to connect the Hall bar response (the Hall resistance) to inhomogeneous magnetic field. In case of classical ballistic transport (as in Chap. 7), when tip potential is narrow as compared to the whole device, the interpretation of conductance maps is straightforward, and as we showed in Chap. 7, the tip is imaging classical electron trajectories.

Beside scanning gate microscopy, in Chaps. 4, 5, and 6 we focused on graphene without the SGM tip. Our initial goal was to investigate SGM measurements in AB rings made out of graphene (as it was done in Ref. [126]), however the initial results were hard to interpret. Therefore, in order to gain familiarity with graphene, in these three chapters we investigated electron transport in static electric potentials, with or without magnetic field. Combined together, these three chapters show the rich physics of graphene, which in most cases is a consequence of its specific electronic structure. Additionally, these three chapters provided us with insights necessary to perform calculations on SGM in graphene (Chap. 7).

In the first of these three chapters (Chap. 4) we examined a side-gated graphene nanoribbon. This system showed the importance of graphene edges on electron transport, and it was a good starting point for understanding transport in other graphene structures, since in all systems leads are modeled as semi-infinite graphene nanoribbons. We showed that, depending on the ribbon orientation and width, a finite gap can be opened in graphene spectrum. Furthermore, a potential on the edges can create a constriction which transmits electrons only at specific (resonant) energies. Ribbons with zigzag edges are particularly interesting, because they offer the possibility to completely switch off or on electron current by simply missaligning the side-gates.

In Chap. 5 we introduced disorder in graphene lattice by randomly removing carbon atoms. Although the Hall resistance of this system was not significantly modified by disorder, new states appeared in-between the Landau levels, and these states manifested themselves in a nonzero bend resistance. In the last of these three chapters (Chap. 6), we studied the influence of four side gates on the quantum Hall effect in graphene. The importance of this chapter is in its demonstration of the relevance of snake states on electron transport in magnetic field. Snake states (or guided states, as we sometimes call them) should appear around equipotential lines where the electron en-

ergy matches the energy of a graphene Landau level. After combining all these insights on transport in graphene with no perturbing SGM potential, we focus in the Chap. 7 on SGM experiments.

Graphene is a very active area of research and previous topics showed only one small part of open questions regarding transport in graphene. At the present moment, we see several directions for future research. From the theory point of view, a determination of the SGM tip potential in graphene using a self-consistent Poisson solver would provide more reliable parameters for modeling SGM experiments. One of the open questions also concerns with the SGM imaging of guided states. To our knowledge this question has not been addressed neither experimentally nor theoretically. Magnetic focusing experiments in graphene studied in previous chapter showed that fine control of electron trajectories in graphene could be achieved with application of weak magnetic fields. Considering similarities between electrons in graphene and light particles, graphene has recently become a suitable material for applications in electron optics. Electron analogues of optical devices can be build in graphene, and SGM microscopy is one of the ways to test for characteristics of these devices. Building electron optical devices in graphene would require better control of electron motion, and construction of various optical elements (collimated electron sources, electron detectors, electron lenses, beam splitters etc). Further analysis of edge effects, disorder, and electrostatic gating, and how would they will affect different parts of an electron optical device is needed.

CHAPTER 9

Samenvatting

In deze thesis onderzochten we de scanning gate microscopie techniek (SGM) en de toepassingen hiervan voor het bestuderen van twee-dimensionaal (2D) elektronentransport in grafeen en halfgeleider heterostructuren. Naast SGM, bestudeerden we ook elektronentransport zonder SGM tip in grafeen nanostructuren. Tijdens deze studies werd gebruik gemaakt van twee verschillende numerieke methoden: de tijdsafhankelijke voortplanting van golfpakketten en de dichte-bindings golffunctie benadering zoals deze beschikbaar is in het KWANT software pakket.

Scanning gate microscopie is een relatief nieuwe meettechniek, gebaseerd op de twee voorbeelden die we in deze thesis presenteren (Chaps. 3 en 7) wordt het potentieel voor de toepassing hiervan voor de karakterisatie van elektronentransport duidelijk. In combinatie met andere scanningstechnieken (b.v. AFM), kan SGM bijkomende informatie verschaffen die nuttig is voor het bepalen van de relatie tussen de structuur van een nanocomponent en zijn geleidbaarheid. Zoals aangetoond in Chaps. 3 en 7, kan de SGM methode toegepast worden op verschillende materialen en in verschillende transport regimes. De enige vereiste is dat het elektronengas zich dicht tegen het oppervlak bevindt. De resultaten, voorgesteld in Chap. 3, tonen dat SGM gebruikt kan worden om kwantumfenomenen te bestuderen waar de SGM tip met de elektrongolffunctie interageert en de resulterende conductantiemap interferentie effecten vertoont. Het tweede geval (bestudeerd in

Chap. 7) toont dat de techniek kan gebruikt worden om ballistisch transport op micrometerschaal te bestuderen en zo klassieke elektronbanen te visualiseren. De techniek kan ook gebruikt worden in andere gevallen (niet in deze thesis beschouwd) om lokalisatie-effecten in kwantumpunten te bestuderen, waar karakteristieke, concentrische halo's ontstaan rond de lokalisatiecentra. Al deze resultaten geven aan dat bij het interpreteren van SGM maps, het belangrijk is om niet enkel rekening te houden met de eigenschappen van het 2D elektronengas, maar ook van het regime waarin de metingen uitgevoerd werden. Afhankelijk hiervan kan de potentiaal geïnduceerd door de tip, geïnterpreteerd worden als een obstakel dat inkomende elektronen reflecteert, of als een hulpmiddel om de lokale toestandsdichtheid te beïnvloeden (zoals bij lokalisatie, waar de tip fungeert als een beweegbare top gate) of als een lens die een schaduw achter zichzelf werpt (zoals bij magnetische focuseringsexperimenten).

De twee voorbeelden van toepassingen van SGM die in deze thesis bestudeerd werden zijn erg verschillend. In het eerste voorbeeld (Aharonov-Bohm (AB) ringen), bekeken we een systeem waarvan de grootte vergelijkbaar is met de grootte van de door de tip geïnduceerde potentiaal. Hierdoor kan het hele systeem, vanuit het standpunt van de SGM tip, beschouwd worden als quasi 1-dimensionaal. Bij het tweede voorbeeld was de potentiaal die door de tip geïnduceerd wordt veel kleiner dan het beschouwde systeem, dit leidde tot de mogelijkheid om de banen van ballistische elektronen te visualiseren. Beide voorbeelden tonen aan dat de belangrijkste eigenschap van de SGM experimenten, de door de tip geïnduceerde potentiaal is. Vanuit een experimenteel standpunt, is een verdere karakterisatie van deze potentiaal nodig om een betere beheersing van toekomstige SGM experimenten te bekomen. Experimenten zoals deze uitgevoerd in Ref. [23] tonen aan dat nanostructuren met een 2D elektronengas gebruikt kunnen worden als nano-meettoestellen. Toekomstige experimenten kunnen kwantumpunten gebruiken als lokale potentiometers om de SGM potentiaal te meten nabij andere nanostructuren. Wat de theorie achter SGM betreft, is er verder onderzoek nodig naar de relatie tussen de waargenomen conductantie en eigenschappen zoals de lokale stroomdichtheid om tot een betere interpretatie van de gemeten conductantiemaps te komen. In tegenstelling tot STM metingen, is bij SGM de tip-geïnduceerde potentiaal niet gelokaliseerd rond één of zelfs enkele atomen, maar spreidt deze zich verder uit. De waargenomen conductantie is daardoor niet enkel afhankelijk van de stroom net onder de tip, maar van de gemiddelde stroom in het gebied waarover de potentiaal zich uitstrekt. Met andere woor-

den, de relatie tussen lokale stroomdichtheid en de gemeten conductantie is geen simpele één-op-één afbeelding, maar een convolutie die afhankelijk is van de tip-geïnduceerde potentiaal. Het ultieme doel van een theoretische studie zou het vinden van een inverse transformatie zijn, die in combinatie met de geïnduceerde potentiaal en de conductantiemap, de lokale stroomdichtheid zou opleveren. Deze transformatie ontbreekt voorlopig nog. Gelijkaardig onderzoek werd uitgevoerd in Ref. [125] waar een Hall sensor werd gebruikt om inhomogene magnetische velden te mappen. Een transformatie functie werd gebruikt om de Hall weerstand te linken met een magnetisch veld. In het geval van klassiek, ballistisch transport (zoals in Chap. 7), wanneer de tip-potentiaal kleiner is dan het gehele systeem, is de interpretatie van conductantiemaps voor de hand liggend en zoals we toonden in Chap. 7, visualiseert de SGM tip klassieke elektronbanen.

Naast scanning gate microscopie, bekeken we in Chaps. 4, 5, en 6 grafeen zonder de SGM tip. Ons oorspronkelijk doel was om SGM metingen te bestuderen in AB ringen gemaakt van grafeen (zoals in Ref. [126]), echten de initiële resultaten waren echter moeilijk te interpreteren. Daarom hebben we, om vertrouwd te geraken met grafeen, in deze drie hoofdstukken elektrontransport in statische elektrische potentialen onderzocht met en zonder de aanwezigheid van magnetische velden. Tesaamen tonen deze drie hoofdstukken de rijke fysica van grafeen, die meestal voortvloeit uit de specifieke elektronische structuur van het materiaal. Bovendien brachten deze hoofdstukken ons de nodige inzichten om SGM berekeningen op grafeen uit te voeren (Chap. 7).

In het eerste van deze drie hoofdstukken (Chap. 4), onderzochten we een nanolint van grafeen met een zijdelingse gate. Dit systeem toonde het belang van de grafeenranden voor elektrontransport en het vormde een goed startpunt voor het begrijpen van transport in andere grafeenstructuren, aangezien elektrische contacten in alle systemen gemodeleerd worden als half-oneindige grafeen nanolinten. We toonden aan dat afhankelijk van de oriëntatie en breedte van het nanolint, er zich een energie kloof kan vormen in het elektronisch spectrum van grafeen. Bovendien kan een potentiaal aan de randen een constrictie vormen die enkel elektronen met specifieke (resonantie) energieën doorlaat. Nanolinten met zig-zag randen zijn bijzonder interessant omdat zij de mogelijkheid bieden om de elektronenstroom volledig aan en af te zetten door de zijdelingse gates al dan niet te aligneren.

In Chap. 5 introduceerden we wanorde in het rooster van grafeen door willekeurige atomen te verwijderen. Alhoewel de Hall weerstand van dit sys-

teem niet significant wijzigde ten gevolge van deze wanorde, verschenen er nieuwe toestanden tussen de Landau niveaus, en deze toestanden resulteerden in een eindige buigingsweerstand. In het laatste van deze drie hoofdstukken (Chap. 6), bestudeerden we de invloed van vier zijdelingse gates op het kwantum Hall effect in grafeen. Het belang van dit hoofdstuk zit in het aantonen van de relevantie van slangachtige banen op het elektronentransport in aanwezigheid van een magnetisch veld. Slangtoestanden (of geleide toestanden zoals soms genoemd) verschijnen rond equipotentiaallijnen waar de energie van de elektronen gelijk is aan de energie van een Landau niveau in het grafeen. Nadat we alle inzichten over transport in grafeen zonder SGM potentiaal combineerden, focusten we ons in Chap. 7 op SGM experimenten.

Grafeen is een erg actief onderzoeksdomein en vorige studies bekeken enkel een klein deel van de nog open vragen betreffende transport in grafeen. Momenteel zien we verschillende paden voor verder onderzoek. Vanuit een theoretisch standpunt zou het bepalen van de SGM tip-potentiaal in grafeen, gebruik makende van een zelf-consistente Poisson oplossing, meer betrouwbare parameters opleveren voor het modelleren van SGM experimenten. Nog een open vraag betreft de beeldvorming van geleide toestanden met behulp van SGM, voor zover wij weten is deze vraag noch theoretisch, noch experimenteel behandeld. Magnetische focuseringsexperimenten in grafeen toonden aan dat een zeer fijne beheersing van de banen van elektronen in grafeen reeds bekomen kan worden met erg zwakke magnetische velden. Gezien de overeenkomsten tussen elektronen in grafeen en lichtdeeltjes, is grafeen recent een geschikt materiaal geworden voor toepassingen in elektronenoptica. Elektron varianten van optische toestellen kunnen gemaakt worden met grafeen en SGM is één van de manieren om de eigenschappen hiervan te testen. Het construeren van deze optische toestellen in grafeen, vereist een betere controle van de beweging van elektronen en de constructie van verschillende optische elementen (gecollimeerde elektronbronnen, elektron detectors, elektron lenzen, bundelsplitters enz.). Verdere analyse van randeffecten, wanorde en elektostatische gating en hoe zij verschillende delen van een optisch toestel beïnvloeden is bovendien nodig.

Appendices

APPENDIX A

Force field in classical SGM simulation

The Lorentz force acting on an electron in an electromagnetic field is given by

$$\mathbf{F} = -e(\mathbf{E} + \mathbf{v} \times \mathbf{B}),$$

which in 2D case (when there is no electric field) can be written as

$$\mathbf{F} = m\mathbf{a} = -e \begin{vmatrix} \mathbf{e}_x & \mathbf{e}_y & \mathbf{e}_z \\ v_x & v_y & 0 \\ 0 & 0 & B \end{vmatrix} = -ev_y B \mathbf{e}_x + ev_x B \mathbf{e}_y$$

In graphene, if we replace the mass term m with a dynamical mass $m^* = \hbar\sqrt{\pi n}/v_F$, we get

$$\mathbf{a} = \mathbf{F}/m^* = \frac{eB}{\hbar\sqrt{\pi n}} v_F (-v_y \mathbf{e}_x + v_x \mathbf{e}_y) = \frac{eB}{E_F} v_F^2 (-v_y \mathbf{e}_x + v_x \mathbf{e}_y).$$

The SGM tip changes the local Fermi energy, and consequently it modifies the acceleration. However, the second (more important) contribution comes from the tip induced potential. This potential effectively creates an in-plane electric field in the graphene sample, and this field $\mathbf{E} = \nabla U(\mathbf{r})/e$ produces additional force acting on electrons

$$\mathbf{F} = -\nabla U(\mathbf{r}).$$

Since global charge density can be considered constant, previous force can be rewritten as

$$\mathbf{F} = \nabla E_F(\mathbf{r}).$$

Repeating the same procedure as in the case when there was no potential, i.e. expressing the force using the dynamical mass, and expressing the local Fermi energy using the local charge density $E_F(x, y) = \hbar v_F \sqrt{\pi(n_0 + \Delta n(x, y))}$, we obtain

$$\mathbf{a} = \frac{1}{2} v_F^2 \frac{\nabla n(\mathbf{r})}{n(\mathbf{r})}.$$

Here, a general relation

$$\nabla \sqrt{f(x, y)} = \frac{1}{2} \frac{1}{\sqrt{f(x, y)}} \nabla f(x, y)$$

is used to obtain the previous expression. Again, using the fact that the global charge density is constant, the acceleration can be written as

$$\mathbf{a} = \frac{1}{2} v_F^2 \frac{\nabla (\Delta n(\mathbf{r}))}{n_0 + \Delta n(\mathbf{r})}.$$

The only thing left is to obtain the gradient of the tip-induced charge density

$$\Delta n(x, y) = \frac{\tilde{q}h}{[(x - x_{\text{tip}})^2 + (y - y_{\text{tip}})^2 + h^2]^{3/2}}.$$

Along the x direction

$$\frac{\partial}{\partial x} \Delta n(x, y) \mathbf{e}_x = -3\Delta n(x, y) \frac{(x - x_{\text{tip}}) \mathbf{e}_x}{(x - x_{\text{tip}})^2 + (y - y_{\text{tip}})^2 + h^2},$$

and along the y direction

$$\frac{\partial}{\partial y} \Delta n(x, y) \mathbf{e}_y = -3\Delta n(x, y) \frac{(y - y_{\text{tip}}) \mathbf{e}_y}{(x - x_{\text{tip}})^2 + (y - y_{\text{tip}})^2 + h^2}.$$

From these two derivatives, we can write the components of the acceleration vector

$$a_x = -\frac{3}{2} v_F^2 \frac{\Delta n(x, y)}{n_0 + \Delta n(x, y)} \frac{(x - x_{\text{tip}})}{(x - x_{\text{tip}})^2 + (y - y_{\text{tip}})^2 + h^2},$$

and

$$a_y = -\frac{3}{2} v_F^2 \frac{\Delta n(x, y)}{n_0 + \Delta n(x, y)} \frac{(y - y_{\text{tip}})}{(x - x_{\text{tip}})^2 + (y - y_{\text{tip}})^2 + h^2}.$$

This acceleration is added to that when there is no tip-induced potential. An interesting feature of this acceleration is that it becomes infinite in areas where the local Fermi energy $n_0 + \Delta n$ is zero.

APPENDIX *B*

Analytical expression for the modified vector potential

Starting from scalar functions $F(x, y)$, we want to derive the analytical expression for the modified vector potential $\mathbf{A}' = \mathbf{A} + \nabla F$. The function $F(x, y)$ is defined as

$$\begin{aligned} F(x, y) &= F_2(x, y) + F_4(x, y) \\ &= \frac{1}{2}Bxy \left[1 + \tanh \left(2\frac{y - y_u}{d} \right) \right] + \\ &\quad \frac{1}{2}Bxy \left[1 + \tanh \left(2\frac{y_d - y}{d} \right) \right], \end{aligned} \quad (\text{B.1})$$

and since

$$\frac{\partial}{\partial x} \tanh \xi(x) = (1 - \tanh^2 x) \frac{\partial}{\partial x} \xi(x), \quad (\text{B.2})$$

we can derive two helpful expressions

$$\begin{aligned} \frac{\partial}{\partial y} \tanh \left(2\frac{y - y_u}{d} \right) &= \left[1 - \tanh^2 \left(2\frac{y - y_u}{d} \right) \right] \frac{\partial}{\partial y} \left(2\frac{y - y_u}{d} \right) \\ &= \frac{2}{d} \left[1 - \tanh^2 \left(2\frac{y - y_u}{d} \right) \right], \end{aligned} \quad (\text{B.3})$$

and

$$\frac{\partial}{\partial y} \tanh \left(2 \frac{y_d - y}{d} \right) = -\frac{2}{d} \left[1 - \tanh^2 \left(2 \frac{y_d - y}{d} \right) \right], \quad (\text{B.4})$$

which we will use to calculate the gradient

$$\nabla F(x, y) = \frac{\partial}{\partial x} F(x, y) \mathbf{e}_x + \frac{\partial}{\partial y} F(x, y) \mathbf{e}_y. \quad (\text{B.5})$$

Because $F(x, y)$ is a sum of two functions, we can calculate the gradient for each of these functions separately

$$\begin{aligned} \nabla F_2(x, y) &= \frac{1}{2} B y \left[1 + \tanh \left(2 \frac{y - y_u}{d} \right) \right] \mathbf{e}_x + \\ &\quad \frac{1}{2} B x \left[1 + \tanh \left(2 \frac{y - y_u}{d} \right) \right] \mathbf{e}_y + \\ &\quad B x y \frac{1}{d} \left[1 - \tanh^2 \left(2 \frac{y - y_u}{d} \right) \right] \mathbf{e}_y, \end{aligned} \quad (\text{B.6})$$

and

$$\begin{aligned} \nabla F_4(x, y) &= \frac{1}{2} B y \left[1 + \tanh \left(2 \frac{y_d - y}{d} \right) \right] \mathbf{e}_x + \\ &\quad \frac{1}{2} B x \left[1 + \tanh \left(2 \frac{y_d - y}{d} \right) \right] \mathbf{e}_y + \\ &\quad - B x y \frac{1}{d} \left[1 - \tanh^2 \left(2 \frac{y_d - y}{d} \right) \right] \mathbf{e}_y. \end{aligned} \quad (\text{B.7})$$

Summing these two expressions, we obtain

$$\begin{aligned} \nabla F(x, y) &= \frac{1}{2} B y \left[2 + \tanh \left(2 \frac{y - y_u}{d} \right) + \tanh \left(2 \frac{y_d - y}{d} \right) \right] \mathbf{e}_x + \\ &\quad \frac{1}{2} B x \left[2 + \tanh \left(2 \frac{y - y_u}{d} \right) + \tanh \left(2 \frac{y_d - y}{d} \right) \right] \mathbf{e}_y + \\ &\quad \frac{B x y}{d} \left[\tanh^2 \left(2 \frac{y_d - y}{d} \right) - \tanh^2 \left(2 \frac{y - y_u}{d} \right) \right] \mathbf{e}_y. \end{aligned} \quad (\text{B.8})$$

When we add this modification to the starting (unmodified) vector potential $\mathbf{A}_H = -B y \mathbf{e}_x$, we obtain

$$\begin{aligned}
\mathbf{A}_H + \nabla F &= \frac{1}{2}By \left[\tanh \left(2\frac{y-y_u}{d} \right) + \tanh \left(2\frac{y_d-y}{d} \right) \right] \mathbf{e}_x + \\
&\frac{1}{2}Bx \left[2 + \tanh \left(2\frac{y-y_u}{d} \right) + \tanh \left(2\frac{y_d-y}{d} \right) \right] \mathbf{e}_y + \\
&\frac{Bxy}{d} \left[\tanh^2 \left(2\frac{y_d-y}{d} \right) - \tanh^2 \left(2\frac{y-y_u}{d} \right) \right] \mathbf{e}_y, \quad (\text{B.9})
\end{aligned}$$

which is the expression used to plot the vector potential in Fig. 5.4 in Chapter 4.

References

1. Y. V. Nazarov & Y. M. Blanter. *Quantum Transport* (Cambridge University Press, 2009).
2. T. Ihn. *Semiconductor Nanostructures 232–233* (Oxford University Press, 2010).
3. Y. Imry. *Introduction to Mesoscopic Physics* (Oxford University Press, 1997).
4. S. Datta. *Electronic Transport in Mesoscopic Systems* (Cambridge University Press, 1995).
5. K. von Klitzing, G. Dorda & M. Pepper. New Method for High-Accuracy Determination of the Fine-Structure Constant Based on Quantized Hall Resistance. *Phys. Rev. Lett.* **45**, 494–497 (1980).
6. D. C. Tsui, H. L. Stormer & A. C. Gossard. Two-Dimensional Magnetotransport in the Extreme Quantum Limit. *Phys. Rev. Lett.* **48**, 1559–1562 (1982).
7. B. J. van Wees *et al.* Quantized conductance of point contacts in a two-dimensional electron gas. *Phys. Rev. Lett.* **60**, 848–850 (1988).
8. D. A. Wharam *et al.* Addition of the one-dimensional quantised ballistic resistance. *Journal of Physics C: Solid State Physics* **21**, L887 (1988).
9. M. A. Reed *et al.* Spatial quantization in GaAs-AlGaAs multiple quantum dots. *Journal of Vacuum Science & Technology B* **4**, 358–360 (1986).

References

10. G. Binnig, H. Rohrer, Ch. Gerber & E. Weibel. Surface Studies by Scanning Tunneling Microscopy. *Phys. Rev. Lett.* **49**, 57–61 (1982).
11. G. Binnig, H. Rohrer, Ch. Gerber & E. Weibel. 7 x 7 Reconstruction on Si(111) Resolved in Real Space. *Phys. Rev. Lett.* **50**, 120–123 (1983).
12. R. Landauer. Spatial Variations of Currents and Fields Due to Localized Scatterers in Metallic Conduction. *IBM J.Res.Develop* **32**, 306 (1988).
13. P. R. Wallace. The Band Theory of Graphite. *Phys. Rev.* **71**, 622–634 (1947).
14. M. O. Goerbig. Electronic properties of graphene in a strong magnetic field. *Rev. Mod. Phys.* **83**, 1193 (2011).
15. M. I. Katsnelson, K. S. Novoselov & A. K. Geim. Chiral tunnelling and the Klein paradox in graphene. *Nat Phys* **2**, 620–625 (2006).
16. Y. Aharonov & D. Bohm. Significance of Electromagnetic Potentials in the Quantum Theory. *Phys. Rev.* **115**, 3 (1959).
17. M. A. Topinka *et al.* Imaging Coherent Electron Flow from a Quantum Point Contact. *Science* **289**, 2323 (2000).
18. M. A. Eriksson *et al.* Cryogenic scanning probe characterization of semiconductor nanostructures. *Appl. Phys. Lett.* **69**, 671–673 (1996).
19. R. Jalilian *et al.* Scanning gate microscopy on graphene: charge inhomogeneity and extrinsic doping. *Nanotechnology* **22**, 295705 (2011).
20. S. Bhandari *et al.* Imaging Cyclotron Orbits of Electrons in Graphene. *Nano Lett.* **16**, 1690 (2016).
21. M. Pala *et al.* Scanning gate microscopy of quantum rings: effects of an external magnetic field and of charged defects. *Nanotechnology* **20**, 264021 (2009).
22. M. G. Pala *et al.* Local density of states in mesoscopic samples from scanning gate microscopy. *Phys. Rev. B* **77**, 125310 (2008).
23. A. E. Gildemeister *et al.* Measurement of the Tip-Induced Potential in Scanning Gate Experiments. *Phys. Rev. B* **75**, 195338 (2007).
24. S. Schnez *et al.* Imaging localized states in graphene nanostructures. *Phys. Rev. B* **82**, 165445 (2010).

-
25. R. A. Jalabert, W. Szewc, S. Tomsovic & D. Weinmann. What Is Measured in the Scanning Gate Microscopy of a Quantum Point Contact? *Phys. Rev. Lett.* **105**, 166802 (2010).
 26. M. A. Topinka *et al.* Coherent branched flow in a two-dimensional electron gas. *Nature* **410**, 183–186 (2001).
 27. C. W. Groth, M. Wimmer, A. R. Akhmerov & X. Waintal. Kwant: a software package for quantum transport. *New J. Phys.* **16**, 063065 (2014).
 28. D. K. Ferry, S. M. Goodnik & J. Bird. *Transport in Nanostructures* (Cambridge University Press, 2009).
 29. Daniel S. Fisher & Patrick A. Lee. Relation between conductivity and transmission matrix. *Phys. Rev. B* **23**, 6851 (1981).
 30. A. A. Kozikov *et al.* Interference of electrons in backscattering through a quantum point contact. *New. Jour. Phys.* **15**, 013056 (2013).
 31. B. Hackens *et al.* Imaging and controlling electron transport inside a quantum ring. *Nat. Phys.* **2**, 826–830 (2006).
 32. F. Martins *et al.* Imaging Electron Wave Functions Inside Open Quantum Rings. *Phys. Rev. Lett.* **99**, 136807 (2007).
 33. H. Sellier *et al.* On the imaging of electron transport in semiconductor quantum structures by scanning-gate microscopy: successes and limitations. *Semicond. Sci. Technol.* **26**, 064008 (2011).
 34. A. Baumgartner *et al.* Classical Hall effect in scanning gate experiments. *Phys. Rev. B* **74**, 165426 (2006).
 35. P. Fallahi *et al.* Imaging a Single-Electron Quantum Dot. *Nano Letters* **5**, 223–226 (2005).
 36. R. Crook *et al.* Imaging Fractal Conductance Fluctuations and Scarred Wave Functions in Quantum Billiard. *Phys. Rev. Lett.* **91**, 246803 (2003).
 37. C. Gorini *et al.* Theory of scanning gate microscopy. *Phys. Rev. B* **88**, 035406 (2013).
 38. B. Szafran. Scanning gate microscopy simulations for quantum rings: Effective potential of the tip and conductance maps. *Phys. Rev. B* **84**, 075336 (2011).

39. K. Kolasiński, B. Szafran, B. Brun & H. Sellier. Interference features in scanning gate conductance maps of quantum point contacts with disorder. *Phys. Rev. B* **94**, 075301 (Aug. 2016).
40. A. Chaves, G. A. Farias, F. M. Peeters & B. Szafran. Wave packet dynamics in semiconductor quantum rings of finite width. *Phys. Rev. B* **80**, 125331 (2009).
41. T. Chwiej & B. Szafran. Schrodinger-Poisson calculations for scanning gate microscopy of quantum rings based on etched two-dimensional electron gas. *Phys. Rev. B* **87**, 085302 (2013).
42. D. E. Manolopoulos. Derivation and reflection properties of a transmission-free absorbing potential. *Journal of Chemical Physics* **117**, 9552 (2002).
43. B. L. Al'tshuler, A. G. Aronov & B. Z. Spivak. The Aaronov-Bohm effect in disordered conductors. *JETP Lett.* **33**, 94 (1981).
44. B. Szafran & F. M. Peeters. Time-dependent simulations of electron transport through a quantum ring: Effect of the Lorentz force. *Phys. Rev. B* **72**, 165301 (2005).
45. G. Papp & F. M. Peeters. Resistance maps from local probing of a ballistic mesoscopic Hall bar. *J. Appl. Phys.* **101**, 063715 (2007).
46. G. Papp & F. M. Peeters. Resistance maps for a submicron Hall electrosensor in the diffusive regime. *J. Appl. Phys.* **101**, 113717 (2007).
47. K. S. Novoselov *et al.* Electric Field Effect in Atomically Thin Carbon Films. *Science* **306**, 666 (2004).
48. Z. Chen, Y. Lin, M. J. Rooks & P. Avouris. Graphene Nano-Ribbon Electronics. *Physica E* **40**, 228 (2007).
49. M. Y. Han, B. Özyilmaz, Y. Zhang & P. Kim. Energy Band-Gap Engineering of Graphene Nanoribbons. *Phys. Rev. Lett.* **98**, 206805 (2007).
50. F. Molitor *et al.* Transport gap in side-gated graphene constrictions. *Phys. Rev. B* **79**, 075426 (2009).
51. F. Molitor *et al.* Local gating of a graphene Hall bar by graphene side gates. *Phys. Rev. B* **76**, 245426 (24 Dec. 2007).
52. J. Cai *et al.* Atomically precise bottom-up fabrication of graphene nanoribbons. *Nature* **466**, 470 (2010).
53. K. Wakabayashi & M. Sigrist. Zero-Conductance Resonances due to Flux States in Nanographite Ribbon Junctions. *Phys. Rev. Lett.* **84**, 3390 (15 Apr. 2000).

-
54. K. Wakabayashi. Electronic transport properties of nanographite ribbon junctions. *Phys. Rev. B* **64**, 125428 (2001).
 55. K. Wakabayashi & M. Sigrist. Enhanced conductance fluctuation due to the zero-conductance Fano resonances in the quantum point contact on graphene. *J. Phys. Soc. Jpn.* **77**, 113708 (2008).
 56. R. Yang, L. Huang, Y.-C. Lai & C. Grebogi. Abnormal electron paths induced by Klein tunneling in graphene quantum point contacts. *Phys. Rev. B* **84**, 035426 (2011).
 57. K. Nakada, M. Fujita, G. Dresselhaus & M. S. Dresselhaus. Edge state in graphene ribbons: Nanometer size effect and edge shape dependence. *Phys. Rev. B* **54**, 17954 (1996).
 58. L. Brey & H. A. Fertig. Electronic states of graphene nanoribbons studied with the Dirac equation. *Phys. Rev. B* **73**, 235411 (2006).
 59. W. Apel, G. Pal & L. Schweitzer. Energy gap in graphene nanoribbons with structured external electric potentials. *Phys. Rev. B* **83**, 125431 (2011).
 60. A. R. Akhmerov, J. H. Bardarson, A. Rycerz & C. W. J. Beenakker. Theory of the valley-valve effect in graphene nanoribbons. *Phys. Rev. B* **77**, 205416 (2008).
 61. A. Rycerz, J. Tworzydło & C. W. J. Beenakker. Valley filter and valley valve in graphene. *Nat Phys* **3**, 172 (2007).
 62. A. Cresti, G. Grosso & G. P. Parravicini. Valley-valve effect and even-odd chain parity in pn graphene junctions. *Phys. Rev. B* **77**, 233402 (2008).
 63. U. Fano. Effects of Configuration Interaction on Intensities and Phase Shifts. *Phys. Rev.* **124**, 1866 (1961).
 64. M. Wimmer *et al.* Spin Currents in Rough Graphene Nanoribbons: Universal Fluctuations and Spin Injection. *Phys. Rev. Lett.* **100**, 177207 (2008).
 65. M. Wimmer, A. R. Akhmerov & F. Guinea. Robustness of edge states in graphene quantum dots. *Phys. Rev. B* **82**, 045409 (2010).
 66. J. Wilhelm, M. Walz & F. Evers. *Ab initio* quantum transport through armchair graphene nanoribbons: Streamlines in the current density. *Phys. Rev. B* **89**, 195406 (19 May 2014).

References

67. Z. Yuanbo, Y. W. Tan, H. L. Stormer & P. Kim. Experimental observation of the quantum Hall effect and Berry's phase in graphene. *Nature* **438**, 201 (2005).
68. K. S. Novoselov *et al.* Two-dimensional gas of massless Dirac fermions in graphene. *Nature (London)* **438**, 197 (2005).
69. Y. Zhang *et al.* Landau-Level Splitting in Graphene in High Magnetic Fields. *Phys. Rev. Lett.* **96**, 136806 (2006).
70. G. Li, A. Luican & E. Y. Andrei. Scanning Tunneling Spectroscopy of Graphene on Graphite. *Phys. Rev. Lett* **102**, 176804 (2009).
71. K. von Klitzing. The quantized Hall effect. *Rev. Mod. Phys.* **58**, 519–531 (1986).
72. Y Zhang, Y.-W Tan, H. L Stormer & P. Kim. Experimental observation of the quantum Hall effect and Berry's phase in graphene. *Nature* **438**, 201–204 (2005).
73. M. M. Ugeda, I. Brihuega, F. Guinea & J. M. Gómez-Rodríguez. Missing Atom as a Source of Carbon Magnetism. *Phys. Rev. Lett.* **104**, 096804 (2010).
74. J. Duffy, J. A. Lawlor, C. Lewenkopf & M. S. Ferreira. Impurity invisibility in graphene: Symmetry guidelines for the design of efficient sensors. *Phys. Rev. B* **94**, 045417 (2016).
75. D. A. Ruiz-Tijerina & da Silva, L. G. G. V. D. Symmetry-protected coherent transport for diluted vacancies and adatoms in graphene. *Phys. Rev. B* **94**, 085425 (2016).
76. M. Droth & G. Burkard. Tuning antiferromagnetism of vacancies with magnetic fields in graphene nanoflakes. *Phys. Rev. B* **91**, 115439 (2015).
77. J. Mao *et al.* Realization of a tunable artificial atom at a supercritically charged vacancy in graphene. *Nature Phys.* **12**, 545–549 (2016).
78. V. M. Pereira, dos Santos, J. M. B. L. & Neto, A. H. C. Modeling disorder in graphene. *Phys. Rev. B* **77**, 115109 (2008).
79. V. M. Pereira *et al.* Disorder Induced Localized States in Graphene. *Phys. Rev. Lett.* **96**, 036801 (2006).
80. A. Cresti *et al.* Broken Symmetries, Zero-Energy Modes, and Quantum Transport in Disordered Graphene: From Supermetallic to Insulating Regimes. *Phys. Rev. Lett.* **110**, 196601 (2013).

-
81. N. Leconte, F. Ortmann, A. Cresti & S. Roche. Unconventional features in the quantum Hall regime of disordered graphene: Percolating impurity states and Hall conductance quantization. *Phys. Rev. B* **93**, 115404 (2016).
 82. F. Ortmann & S. Roche. Splitting of the Zero-Energy Landau Level and Universal Dissipative Conductivity at Critical Points in Disordered Graphene. *Phys. Rev. Lett.* **110**, 086602 (2013).
 83. J. H. García, L. Covaci & T. G. Rappoport. Real-Space Calculation of the Conductivity Tensor for Disordered Topological Matter. *Phys. Rev. Lett.* **114**, 116602 (2015).
 84. H. U. Baranger & A. D. Stone. Electrical linear-response theory in an arbitrary magnetic field: A new Fermi-surface formation. *Phys. Rev. B* **40**, 8169 (1989).
 85. O. Shevtsov *et al.* Graphene-based heterojunction between two topological insulators. *Phys. Rev. X* **2**, 031004 (2012).
 86. M. Büttiker. Four-Terminal Phase-Coherent Conductance. *Phys. Rev. Lett.* **57**, 1761 (1986).
 87. M. Büttiker. Symmetry of electrical conduction. *IBM J. Res. Develop.* **32**, 317 (1988).
 88. A. L. C. Pereira & P. A. Schulz. Additional levels between Landau bands due to vacancies in graphene: Towards defect engineering. *Phys. Rev. B* **78**, 125402 (2008).
 89. J. E. Müller. Effect of a Nonuniform Magnetic Field on a Two-Dimensional Electron Gas in the Ballistic Regime. *Phys. Rev. Lett.* **68**, 385 (1992).
 90. J. Reijniers & F. M. Peeters. Snake orbits and related magnetic edge states. *J. Phys. Condens. Mat.* **12**, 9771 (2000).
 91. A. S. Rozhavsky & R. I. Shekhter. Kinetics of the conduction electrons in multidomain ferromagnets. *Solid State Commun.* **12**, 603 (1973).
 92. G. G. Cabrera & L. M. Falicov. Theory of the Residual Resistivity of Bloch Walls. *Phys. Stat. Sol. (b)* **61**, 539 (1974).
 93. G. G. Cabrera & L. M. Falicov. Theory of the Residual Resistivity of Bloch Walls. *Phys. Stat. Sol. (b)* **61**, 217 (1974).
 94. Y. V. Zakharov & Y. I. Mankov. Magnetoresistance of Ferromagnets with Domain Structure. *Phys. Stat. Sol. (b)* **125**, 197 (1984).

References

95. A. A. Bykov *et al.* Hall effect in a spatially fluctuating magnetic field with zero mean. *Phys. Rev. B* **61**, 5505 (2000).
96. A. Nogaret, J. S. Bending & M. Henini. Resistance Resonance Effects through Magnetic Edge States. *Phys. Rev. Lett* **84**, 2231 (2000).
97. L. Oroszlány *et al.* Theory of snake states in graphene. *Phys. Rev. B* **77**, 081403 (2008).
98. J. R. Williams & C. M. Marcus. Snake States in Graphene p-n Junctions. *Phys. Rev. Lett.* **107**, 046602 (2011).
99. S. P. Milovanović, M. R. Masir & F. M. Peeters. Spectroscopy of snake states using a graphene Hall bar. *Appl. Phys. Lett.* **103**, 233502 (2013).
100. M. T. Allen *et al.* Spatially resolved edge currents and guided-wave electronic states in graphene. *Nat. Phys.* **12**, 128–133 (2016).
101. M. T. Allen *et al.* Visualization of phase-coherent electron interference in a ballistic graphene Josephson junction. *arXiv*. eprint: 1506.06734 (condi-mat.mes-hall) (2015).
102. L. Brey & H. A. Fertig. Edge states and the quantized Hall effect in graphene. *Phys. Rev. B* **73**, 195408 (2006).
103. S. W. LaGasse & J. U. Lee. Theory of Landau level mixing in heavily graded graphene *pn* junctions. *Phys. Rev. B* **94**, 165312 (2016).
104. J. Berezovsky, M. F. Borunda, E. J. Heller & R. M. Westervelt. Imaging coherent transport in graphene (part I): mapping universal conductance fluctuations. *Nanotechnology* **21**, 274013 (2010).
105. J. Berezovsky & R. M. Westervelt. Imaging coherent transport in graphene (part II): probing weak localization. *Nanotechnology* **21**, 274014 (2010).
106. M. R. Connolly *et al.* Scanning gate microscopy of current-annealed single layer graphene. *Appl. Phys. Lett.* **96**, 113501 (2010).
107. M. R. Connolly *et al.* Reading and writing charge on graphene devices. *Appl. Phys. Lett.* **101**, 023505 (2012).
108. S. Neubeck *et al.* Scanning gate microscopy on a graphene quantum point contact. *Physica E Low-Dimensional Systems and Nanostructures* **44**, 1002–1004 (2012).
109. S. Schnez *et al.* The relevance of electrostatics for scanning-gate microscopy. *New J. Phys.* **13**, 053013 (2011).

-
110. M. R. Connolly *et al.* Tilted potential induced coupling of localized states in a graphene nanoconstriction. *Phys. Rev. B* **83**, 115441 (2011).
 111. A. G. F. Garcia, König, M., D. Goldhaber-Gordon & K. Todd. Scanning gate microscopy of localized states in wide graphene constrictions. *Phys. Rev. B* **87**, 085446 (2013).
 112. N. Pascher, D. Bischoff, T. Ihn & K. Ensslin. Scanning gate microscopy on a graphene nanoribbon. *Appl. Phys. Lett.* **101**, 063101 (2012).
 113. A. Mreńca, K. Kolasiński & B. Szafran. Conductance response of graphene nanoribbons and quantum point contacts in scanning gate measurements. *Semiconductor Science and Technology* **30**, 085003 (2015).
 114. S. Bhandari, G.-H. Lee, P. Kim & R. M. Westervelt. *Analysis of Scanned Probe Images for Magnetic Focusing in Graphene* 2016. arXiv: 1608.02248 [cond-mat.mes-hall].
 115. S. Bhandari, A. Lin & R. M. Westervelt. Investigating the Transition Region in Scanned Probe Images of the Cyclotron Orbit in Graphene. *ArXiv e-prints*. arXiv: 1611.04865 (2016).
 116. S. Morikawa *et al.* Imaging ballistic carrier trajectories in graphene using scanning gate microscopy. *Appl. Phys. Lett.* **107**, 243102 (2015).
 117. K. E. Aidala *et al.* Imaging magnetic focusing of coherent electron waves. *Nat. Phys.* **3**, 464–468 (2007).
 118. S. P. Milovanović, M. R. Masir & F. M. Peeters. Magnetic electron focusing and tuning of the electron current with a pn-junction. *J. Appl. Phys.* **115**, 043719 (2014).
 119. K. Kolasiński, A. Mreńca-Kolasińska & B. Szafran. Theory of ballistic quantum transport in the presence of localized defects. *Phys. Rev. B* **94**, 115406 (Sept. 2016).
 120. M.-H. Liu *et al.* Scalable Tight-Binding Model for Graphene. *Phys. Rev. Lett.* **114**, 036601 (2015).
 121. M. Beconcini *et al.* Scaling approach to tight-binding transport in realistic graphene devices: The case of transverse magnetic focusing. *Phys. Rev. B* **94**, 115441 (2016).
 122. S. Bhandari. *Imaging Electron Flow in Graphene* PhD dissertation (Harvard University, 2015).

References

123. T. Andrijauskas, A. A. Shylau & I. V. Zozoulenko. Thomas-Fermi and Poisson modeling of gate electrostatics in graphene nanoribbon. *Lith. J. Phys.* **52**, 63 (2012).
124. T. Stegmann & A. Lorke. Edge magnetotransport in graphene: A combined analytical and numerical study. *Ann. Phys.* **527**, 723–736 (2015).
125. Y. G. Cornelissens & F. M. Peeters. Response function of a Hall magnetosensor in the diffusive regime. *J. Appl. Phys.* **92**, 2006–2012 (2002).
126. D. Cabosart *et al.* Imaging coherent transport in a mesoscopic graphene ring. *Phys. Rev. B* **90**, 205433 (2014).

Marko Petrović

Address

Gligorija Diklića 117

37000 Kruševac, Serbia

Tel. 032/49-70-75-795

Email: marko.petrovic@uantwerpen.be

mpetrovic.ks@gmail.com



PERSONAL

- Date of Birth: 10th April 1986
- Place of Birth: Kruševac, Serbia

EDUCATION

- **University of Antwerp, CMT Group** **2012–2017**
PhD in Theoretical Physics
Thesis title: *Characterization of the scanning gate technique and transport in nanostructured graphene*
Thesis advisor: Prof. Dr. Francois Peeters
- **University of Belgrade, Faculty of Physics** **2005–2011**
Diploma in Theoretical Physics
GPA 9.56 (scale 6–10, 10 denoting the highest grade)
Thesis title: *Spin relaxation in CdTe quantum dots with single Mn atom*
Thesis advisor: Dr. Nenad Vukmirović
- **Kruševac High School** **2001–2005**
Section for mathematics and natural sciences
GPA 4.90 (scale 2–5, 5 denoting the highest grade)

PROFESSIONAL EXPERIENCE

- Attended the “27th Indian-Summer School of Physics on Graphene”, Prague, Czech Republic. **2015**
- Poster presentation on *Fano resonances in graphene nanoribbons* at the “19th Symposium on Condensed Matter Physics (SFKM)”, Belgrade, Serbia. **2015**

- Poster presentation on *Fano resonances in graphene nanoribbons* at the “Graphene Week 2015”, University of Manchester, UK. **2015**
- Attendance and oral presentation at the DRSTP postgraduate school on “Statistical Physics and Theory of Condensed Matter”, Doorn, Netherlands. **2013**
- Attended the “Workshop on Nanostructured Graphene”, Antwerp, Belgium. **2013**
- Internship at the John Adams Institute for Accelerator Science. Project: *Studying Beamstrahlung radiation at the future ILC collider*, University of Oxford, UK. **2009**

COMPUTER SKILLS

Python (numpy, matplotlib, KWANT), C, FORTRAN, bash, LaTeX, vim, git, gnuplot, Origin, MS Office. Experience in cluster computing and in working on MS Windows and Linux platforms.

LANGUAGES

- Serbian: Native speaker
- English: Fluent
- Dutch (Flemish): Basic proficiency (NT2 level 2.3)

SCHOLARSHIPS

- PhD scholarship from the University of Antwerp **2012–2017**
- Serbian Business Club “Privrednik” **2008–2010**
- Serbian Ministry of Education **2006–2007**
- Foundation for Development of Talented Youth **2005–2010**

PUBLICATIONS

- M. Petrović, N. Vukmirović, *Spin relaxation in CdTe quantum dots with a single Mn atom*, Physical Review B **85**, 195311 (2012).

- M. Petrović, F. M. Peeters, A. Chaves, G. A. Farias, *Conductance maps of quantum rings due to a local potential perturbation*, Journal of Physics: Condensed Matter **25**, 495301 (2013).
- M. Petrović, F. M. Peeters, *Fano resonances in the conductance of graphene nanoribbons with side gates*, Physical Review B **91**, 035444 (2015).
- M. Petrović, F. M. Peeters, *Quantum transport in graphene Hall bars: Effects of vacancy disorder*, Physical Review B **94**, 235413 (2016).
- M. Petrović, S. P. Milovanović, F. M. Peeters, *Scanning gate microscopy of magnetic focusing in graphene devices: quantum vs. classical simulation*, Nanotechnology **28**, 185202 (2017).
- M. Petrović, F. M. Peeters, *Quantum transport in graphene Hall bars: Effects of side gates*, Solid State Communications **257**, 20–26 (2017).

REFERENCES

- **Prof. Dr. Francois Peeters**

Head of the Condensed Matter Theory Group (CMT)

Address: University of Antwerp
 Campus Groenenborger
 Groenenborgerlaan 171
 G.U.213
 2020 Antwerpen, Belgium

Phone: 032/65–36–64

Email: francois.peeters@uantwerpen.be

- **Prof. Dr. Andrey Chaves**

Adjunct Professor at the Federal University of Ceará

Address: Universidade Federal do Ceará
 Departamento de Física
 Grupo de Teoria da Matéria Condensada (GTMC)
 Caixa Postal 6030, 60455–760 Fortaleza, Ceará, Brazil

Email: andrey@fisica.ufc.br